INDIAN ASSOCIATION OF NUCLEAR CHEMISTS
AND ALLIED SCIENTISTS

Modern Techniques in Material Characterization

IANCAS
Bulletin

www.iancas.org

January 2008 / Vol. VII / No.1

Vol. VII. No.1 Editor : B.S. Tomar January 2008

Editorial

The last few decades have witnessed a phenomenal advancement in the field of material characterization, particularly after the advent of nano- science and technology. Today, the materials are being viewed at atomic scale with the help of advanced tools like atomic force microscopy and X-ray absorption fine structure spectroscopy, which are providing the most detailed information about the structure of materials. The microstructure of materials at a few Å scale can be investigated using positron annihilation spectroscopy.

In the present bulletin an attempt has been made to bring out the salient features of the materials characterization tools employing electrons, positrons, X-rays, and lasers. I thank Dr. G.K.Dey, Head, Materials Science Division, BARC, to have agreed to be the guest editor of this bulletin. Thanks are also due to all the authors for their contributions to this bulletin. I sincerely hope this thematic bulletin will serve as a good reference for researchers working in the multidisciplinary areas involving physics, chemistry, biology and other subjects.

CONTENTS

Transmission Electron Microscope

Dr. Dinesh Srivastava did his B.E. in metallurgy from University of Roorkee and joined 28th Batch of training school and earned his Ph.D. degree in Metallurgy on the topic "Beta phase transformations in Zr-Nb alloy from Indian Institute of Science Bangalore in 1997. He has extensive experience in structural, morphological, defects and analytical characterization by Transmission electron microscopy. His research activities involves basic physical metallurgy studies of Zr- base alloys, alloy development, fabrication flow Sheet optimization of Zr-base alloy component for PHWR reactors. His other research interests are direct Laser fabrication process and synthesis, processing and characterization of nano crystalline soft magnetic material. He has published more than 65 research papers. He is recipient of Binani Gold Medal for best paper publication in Trans IIM and DAE Science and Technology Excellence award. Presently he is working in Materials science Division of Bhabha Atomic Research Center as scientific Officer.

Dr. Raghvendra Tewari obtained his B. E. in Metallurgical Engineering in 1988 from the University of Roorkee. He joined the 32nd batch of Training School in Bhabha Atomic Research Centre (BARC) and was awarded the Homi Bhabha prize for standing first in his discipline. On completion of training, he joined Physical Metallurgy Division of BARC. He obtained his Ph. D degree from Indian Institute of Technology-Bombay in 2000. He was a postdoctoral fellow at University of Cincinnati from 2002 to 2004. He has won several awards for his scientific contributions. He has been awarded Young Metallurgist Award given by Ministry of Steel and Mines (2000) for his contribution in the field of phase transformation. Areas of his research interest are Phase Transformation in zirconium, niobium and nickel Base Alloys, Amorphous and Rapidly Solidified alloys, Electron microscopy and defect characterization and High Resolution Electron Microscopy. He has more than 80 scientific publications to his credit.

Dr. Gautam Kumar Dey obtained his B. Tech in Metallurgical Engineering in 1979 from the Institute of Technology, Banaras Hindu University. He joined the 23rd batch of Training School in Bhabha Atomic Research Centre (BARC) and was awarded the Homi Bhabha prize for standing first in his discipline. On completion of training, he joined Metallurgy Division of BARC. He obtained his Ph. D. degree from Banaras Hindu University in 1988. He was a postdoctoral fellow at University of Cincinnati from 1994 to 1996. He has been Visiting Scientists at University of Osaka, Japan and Institut fur Festkorperforschung (IFF), Juelich, Germany. He has won several awards for his scientific contributions. Of these mention can be made of the Young Scientist award of Indian National Science Academy (1989), Young Metallurgist Award given by Ministry of Steel and Mines (1989), MRSI Medal given by Materials Research Society of India (2001) and Metallurgist of the year award given by Ministry of Steel (2003). He is a fellow of the Indian National Academy of Engineering (FNAE) and Indian Academy of Sciences (FAS). He is associate editor of Transactions of the Indian Institute of Metals and a key reader for Metallurgical and Materials Transactions. Areas of his research interest are Phase Transformation in Zirconium and Nickel Base Alloys, Amorphous Alloys, Rapidly Solidified Crystalline and Quasicrystalline Alloys, Electron Microscopy and defect Characterization and High Resolution Electron Microscopy. He has more than 190 scientific publications to his credit. He has been designated a Professor in the Homi Bhabha National Institute and is currently the Head of Materials Science Division, BARC.

Dr. D. Srivastava, Dr. R. Tewari and Dr. G. K. Dey, Materials Science Division, Bhabha Atomic Research Center, Mumbai 400 085;

Abstract

The basic principles and design of the transmission electron microscope (TEM) has been outlined in this presentation. In TEM the internal, surface structures, crystallinity and elemental composition of specimens can be examined with high spatial resolution in a single instrument. The principle features of the imaging, diffraction and microanalysis capabilities of TEM have been discussed in this article. The advancement in the Tem in all these has been also presented.

Keywords: Transmission electron microscope; Imaging; Microanalysis; Electron diffraction, scanning transmission electron microscope, Electron energy loss spectrometry

Introduction

The development of TEM was driven primarily to improve the limited resolution of the light microscope due to wavelength limit imposed by visible light. The first transmission electron microscope (TEM) microscope was invented by Knoll and Ruska in 1931 [1]. This microscope was not much of use since this was mainly used to view shadow images. The TEM became much more valuable to the metallurgist and materials science with the development of techniques to thin metals specimens to electron transparency. The potential of TEM got enhanced drastically with the development of dynamical theory of contrast of image formation in TEM [2]. This made it possible to explain and predict the finest detail of diffraction contrast from both perfect crystals and their inherent defects (dislocations and stacking faults etc.) [3]. TEM is possibly only imaging method that has an underlying contrast theory that matches experimental images with the degree of accuracy of TEM diffraction contrast. The practical and theoretical foundation developed in last six decades has made the TEM most important tool for the observation of crystal defects and second-phase precipitates. The TEM technique made it possible to illustrate crucial role of dislocations, grain boundaries, interphase interfaces and other planar defects in controlling principally the mechanical behaviour of materials and also explained chemical, physical, magnetic, electrical, etc. properties to a great extent [2]. Today TEM is the only technique that can unequivocally determine every known type of line and planar defect in crystals and it plays major role in materials research in the characterization of crystal defects. Over last many years electron diffraction has grown into more advanced and powerful tool. The standard, qualitative rather inaccurate interplanar spacing measurements by selected-area diffraction (SAD) patterns of TEM have been superceded by convergent-beam electron diffraction (CBED) [4]. CBED techniques are invariably used to determine point groups and space groups of any unknown phase. It also measures measurement of lattice parameter shifts (e.g. lattice strain) accurate to 0.0001 nm, the quantitative measurement of low-order structure factors and determination of charge-density distributions, etc..

The availability of X-ray spectrometry (energy dispersive spectrometer, EDS) [5-6] and electron spectrometry (electron energy loss spectrometry, EELS) [7] on TEM gives quantitative analysis capabilities covering the whole periodic table [2-4]. TEM has slowly developed over the last 25 years as an analytical instrument. The analytical TEM now offers through the use of scanning mode of transmission electron microscope (STEM) [8] and energy-filtered electron imaging (EFTEM) [9] and X-ray mapping, the analysis information can now be offered as a compositional map. As a result, in addition to the routine image and diffraction planes viewed by conventional electron microscopist, it can now create new image planes of all the signals that are detectable in a modern TEM. The digital imaging techniques allows images to be acquired and stored simultaneously through the technique of spectrum imaging in form elemental chemistry, the local atomic bonding, the dielectric constant, the specimen thickness, and the band gap. With such image forming capabilities TEM is the most powerful tool at the disposal of materials researcher.

By utilizing phase contrast mechanism the atomic structure of materials and defects are now routinely characterized at atomic resolution by high resolution transmission electron microscopy (HRTEM) which provides direct structural imaging at resolutions at or below 0.1 nm [2-10-11]. The resolution of TEM was limited by the lens defects and chromatic aberrations. In last 10 years extensive developments have taken place towards reducing these aberrations. Chromatic aberration limitations due to thick specimens can now be overcome by energy filtering of the imaging electrons. Now aberration free (both probe corrected and image corrected) microscopes are available where structures can be resolved with sub angstrom lattice resolution and chemical analysis at spatial resolutions from the micrometer to the nanometer scale and analytical sensitivities close to the single-atom level can be obtained [12-13].

Preparing high-quality TEM specimens is of paramount importance in TEM studies. A considerable improvement has taken place in this field and advent of the focused ion beam (FIB) microscope has greatly enhanced TEM specimen preparation capabilities [14].

In this article basic design and principle of TEM has been described. The different modes of TEM operation in brief has been highlighted.

Basics of Transmission Electron Microscope

A modern TEM consists of an illumination system provided by electron gun and set of electromagnetic lenses and image is recorded by a film or digital camera (Fig.1). The important components of TEM are described below.

The Illumination System

The Electron Gun

The electron gun usually consists of a tungsten wire of hairpin ("V") shape which is surrounded by a shield centered just below the filament tip [2]. Electrons emitted by the filament are accelerated between the cathode (at high negative potential) and anode (at ground potential). The function of the three electrodes (cathode, shield, and anode) is analogous to the function of the three electrodes of a triode. In a biased gun the shield is maintained at a negative potential with respect to the filament gives rise to a strong electrostatic field around the shield which acts as an electrostatic lens focusing the true source of the emitter below the anode. The gun-crossover is used as the virtual source of electrons for the electron microscope.

A tungsten filament provides adequate illumination for most purposes, but for operation at very high magnifications or using very small probes a brighter electron source is desirable. Replacing a tungsten filament by a conical crystal of LaB_6 gives a ten times increase in brightness, permitting either a more intense spot or a reduction in spot size by a factor of two to three, and hence potentially better scanning resolution. LaB_6 must be operated in a vacuum better than (10^{-6} mbar). Field emission guns (FEG) provide even greater brightness (100 times more than the LaB_6) and electron probes of 0.5 nm diameter can be obtained. However, the gun requires an operating vacuum of (10^{-10} mbar) and adds considerably to cost.

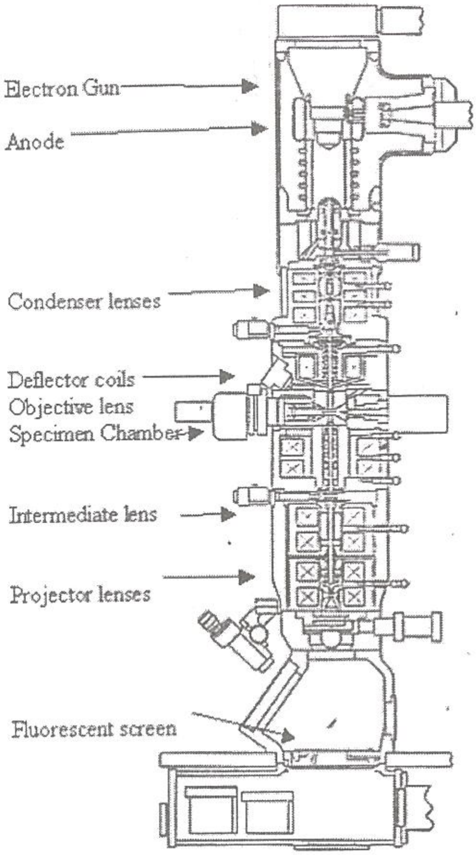

Fig. 1 Important components of transmission electron microscope

Imaging Lenses

a. Principle of an Electromagnetic Lens [2]

An electromagnetic lens consists of a coil of copper wires inside the iron pole pieces. A current through the coils creates a rotationally symmetric magnetic field in the bore of the pole pieces in such a way that it is weak in the center of the gap and stronger close to the bore. Electrons close to the center are less strongly deflected than those passing the lens far from the axis. The overall effect is that a beam of parallel electrons is focused into a spot known as cross-over. The strength of lens can be increased with the magnetic field (by increasing current flowing through the coils). The force acted upon is perpendicular to the magnetic field and its velocity which leads to a helical trajectory of the electrons and to the magnetic rotation. Magnetic lenses influence electrons in a similar way as convex glass lenses do with light and similar diagrams can be drawn to describe the respective ray paths (Fig.2). The imaginary line through the centers of the electromagnetic lenses in electron microscopes is referred as optical axis. The lens equation of light optics is also valid in electron optics, and the magnification is defined accordingly: In electron microscopes, magnetic lenses perform two different tasks (i) for beam formation (as condenser lenses in TEM) (ii) Image formation and magnification (objective, diffraction, intermediate, and projective lenses in TEM).

Similar to glass lenses, magnetic lenses have spherical (electrons are deflected stronger the more they are off-axis) and chromatic aberrations (electrons of different wavelengths are deflected differently). Additionally, the iron pole pieces are not perfectly circular, and this makes the magnetic field deviating from being rotational symmetric. The astigmatism of the objective lens can distort the image seriously which is corrected, by using stigmators [2].

b. Condenser Lenses

The function of the condenser lens system is to focus the electron beam emerging from the electron gun onto the specimen to permit optimal illuminating conditions (Fig. 3). A double condenser system has a strong first lens which is used to produce a demagnified image (spot size control) of the electron source and a weaker second lens projects this (brightness control). A condenser aperture is used to limit the amount of electrons striking the specimen and limit the number of X-rays generated from electrons hitting parts of the microscope column. The size of the C2 aperture determines the maximum semi-angular aperture of

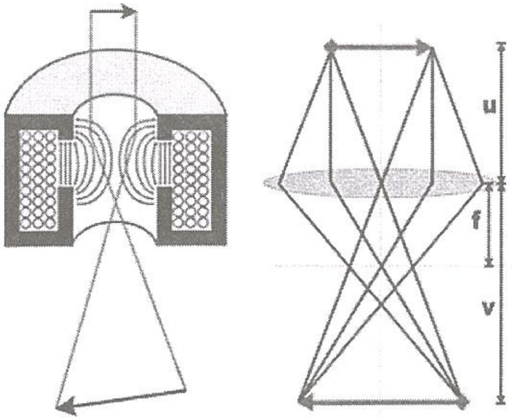

Fig. 2 Schematic showing the function of electromagnetic lens as convex lens in TEM

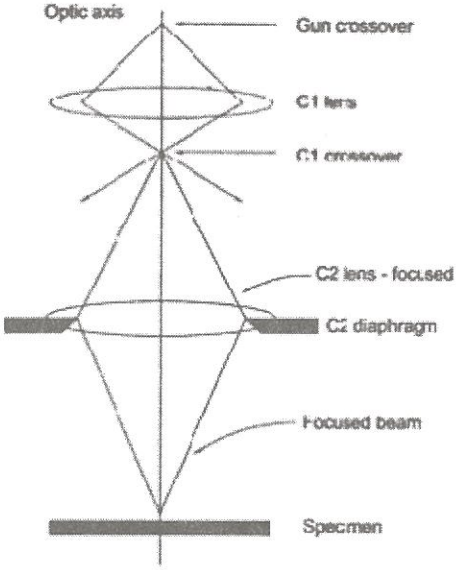

Fig. 3 Schematic showing ray diagram of two condenser lens system in TEM

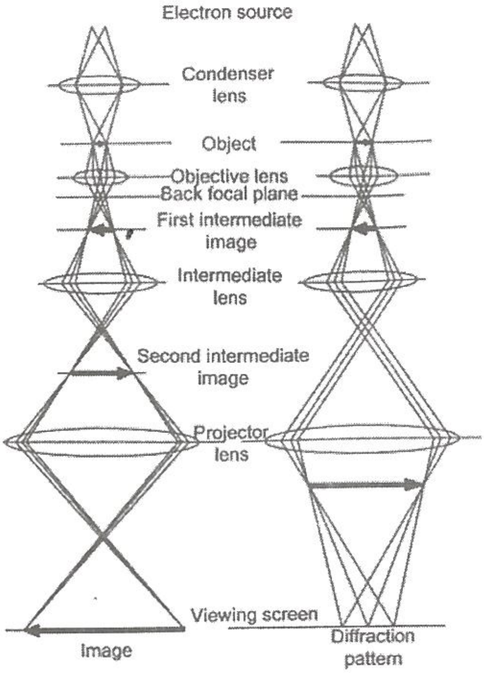

Fig. 4 Schematic showing ray diagram of (a) image mode and (b) diffraction mode of TEM

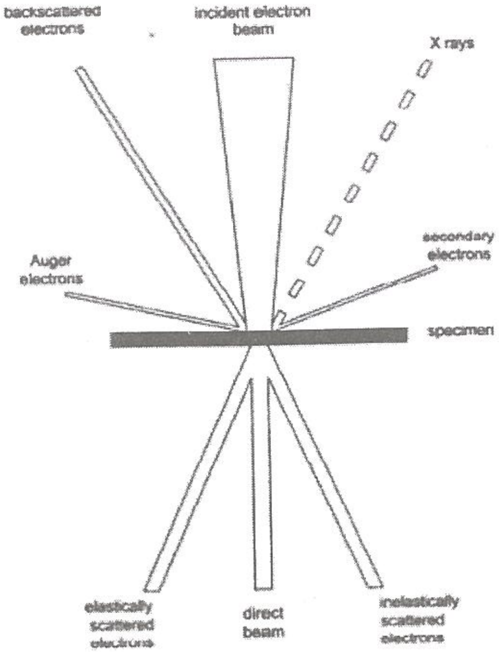

Fig. 5 Schematic showing interaction of electron with matter

the illumination as viewed from the specimen. The larger the aperture angle, the greater the maximum illumination intensity, but in general the poorer the image quality [2,14].

c. The objective lens and the intermediate lenses:

The objective lens is the strongest lens and is used to form the first intermediate image. Specimen chambers is located below condenser lens inside the objective lens. The chamber should allow several millimeter movement and tilting by large angles in both axes. Side entry sample holders are used through an airlock. The quality of this lens determines the ultimate resolution of the image. A diffraction pattern is formed in the back focal plane of the lens (Fig. 4).

The intermediate lens is used to switch between two modes. In image mode it is focused on the image plane of the objective (Fig. 4). The final magnification of image is obtained by combination of other intermediate lenses. Whereas in the diffraction mode the intermediate lens is focused on the image back focal plane of the objective lens and the diffracted beam is projected on to the projection screen. An objective aperture is used to define the angular range of the scattered electrons and its diameter controls the resolution of the microscope.

The image quality (resolution) is strongly depended on the alignment of the electron beam along the optical axis of each lens. Electromagnetic deflection coils are used to compensate some of the lens aberrations in the condenser.

Contrast and Image Formation

Contrast of images formed in TEM is determined by the nature and extent of interactions between the electron beam and the specimen (Fig. 5). There are three distinct contrast mechanism, either one, two or all three may contribute in the appearance of the TEM image.

Amplitude Contrast

Amplitude contrast is produced by the loss of amplitude (i.e. electrons) from the beam. The angular distribution of scattered electron intensities from the sample are excluded from the lens aperture to form image and corresponding area appear dark. This can happen in following two ways.

a. Mass thickness contrast

The interaction of electrons with heavy atoms is stronger than with light atoms. If the thickness is homogeneous, areas in which heavy atoms are concentrated appear with darker contrast than such with light atoms (mass contrast). Also more electrons are scattered in thick than in thin areas; thus, thick areas appear dark (thickness contrast). Thus in TEM the amount of scattering which occurs at any particular specimen point is dependent on its density and overall thickness and is relatively independent of the atomic number, chemical composition, or other specimen properties. The scattering power of a particular area of specimen is directly proportional to its mass density (mass per unit area = density x thickness) (Fig. 6). With increasing mass thickness the probability of scattering increases. However, a thick area with light elements might have the same contrast as a thinner area with heavier atoms. Normally this contrast mechanism is used for biological samples where heavy atom staining is done to obtain contrast. In thick areas, more electron scattering events occur of course; thus, these thick areas appear dark.

b. Diffraction contrast

If a crystalline specimen is transmitted by electrons, then Bragg diffractions happen as well. Each atom in such a regular arrangement acts as a scattering center. The scattered electron waves may interact with each other either in a constructive or in a destructive way, which gives rise to a diffraction. If a crystal is oriented along a zone axis so that many electrons are strongly scattered to contribute to the reflections in the diffraction pattern, then only a few electrons pass without interactions and therefore this crystal appears with dark contrast (diffraction contrast).

In the bright field (BF) mode of the TEM, an aperture is placed in the back focal plane of the objective lens which allows only the direct beam to pass and all scattered electron beams are deflected away from the optical axis and blocked by the objective aperture, then the corresponding areas appear dark in the b right field image (Fig. 7). Whereas in the dark field (DF) mode only one of the diffracted beam is allowed through this aperture and thus the corresponding area from which this diffracted beam comes appears bright (Fig. 7). Examples of dark field and bright field imaging are shown in Fig. 8. Diffraction contrast is extensively used to characterize the different lattice defects present in the material (Fig 9)

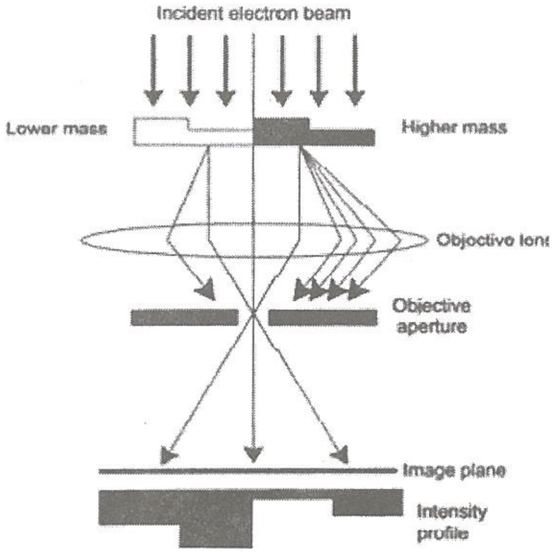

Fig. 6 Schematic diagram showing mechanism of mass thickness contrast in TEM

Phase Contrast

If the interference of diffracted beams are allowed to happen when multiple diffracted beams passes through objective aperture it produces differences in intensity at the image resulting in phase contrast. Thus, contrast arises from interference of the electron wave with itself. For phase contrast imaging the sample should be thin enough and the amplitude variations should not contribute to the images (weak phase object approximation).

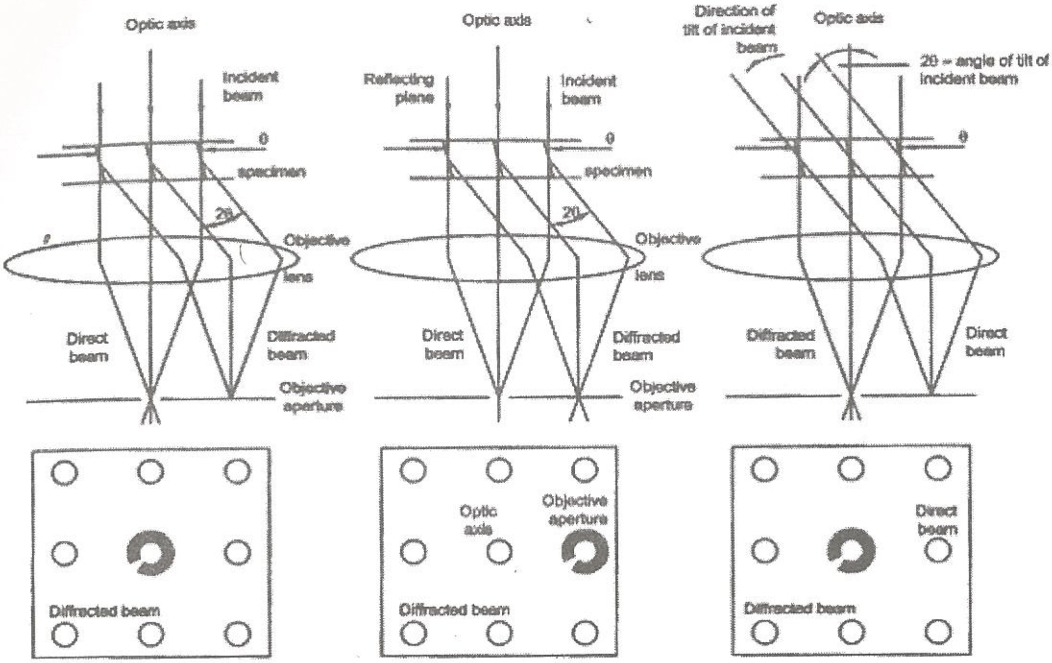

Fig. 7 Bright field and dark field image formation in TEM

Electron Diffraction

Spatial distribution of the elastically scattered electrons constitutes the diffraction patterns. These diffraction patterns can be used to deduce large information about the nature of atomic arrangement and other information's about the crystalline and amorphous materials. Similar to the X-ray diffraction, electron diffraction also results when Bragg condition is met. However, in the case of the electron diffraction since the wave length of electron is very small strong diffraction from these planes of atoms are obtained which are almost parallel to the electron beam. In addition to this the radius of Ewald sphere would be very large in this case. Unlike X-ray diffraction pattern it can be normally assumed electron diffraction pattern to be a section in a reciprocal lattice space. Diffraction pattern consists of a regular array of spots in case of a large single crystal. Whereas, it an be complex if more than one crystal or multiphases are present.. Nano-grains or small grains give rise to ring like pattern. The diffraction pattern of the amorphous material are normally associated with characteristic hallow rings. Examples of diffraction patterns obtained in TEM is shown in Fig 10.

In TEM it is possible to obtain diffraction pattern from a very small region. This technique is known is selected area diffraction (SAD) pattern. Here a SADP can be obtained from individual phases, precipitates or crystals. Thus it makes much easier to identify the nature of the phases. One to one correspondence between the crystal structure and image can be made.

However, in the case of electron diffraction, the deviation in Bragg condition is observed and increases with decreasing crystal thickness. Therefore, electron diffraction is not an accurate method to determine the lattice parameter. There are other diffraction effects as well such as Kikuchi line patterns. Kikuchi lines are used to determine orientation of a grain accurately or misorientation within the structure (low angle grain boundary).

The limitations of SAD pattern were overcome in the late 1970s when CBED techniques developed in step with microanalysis using the new probe-forming, analytical TEMs (see below). But

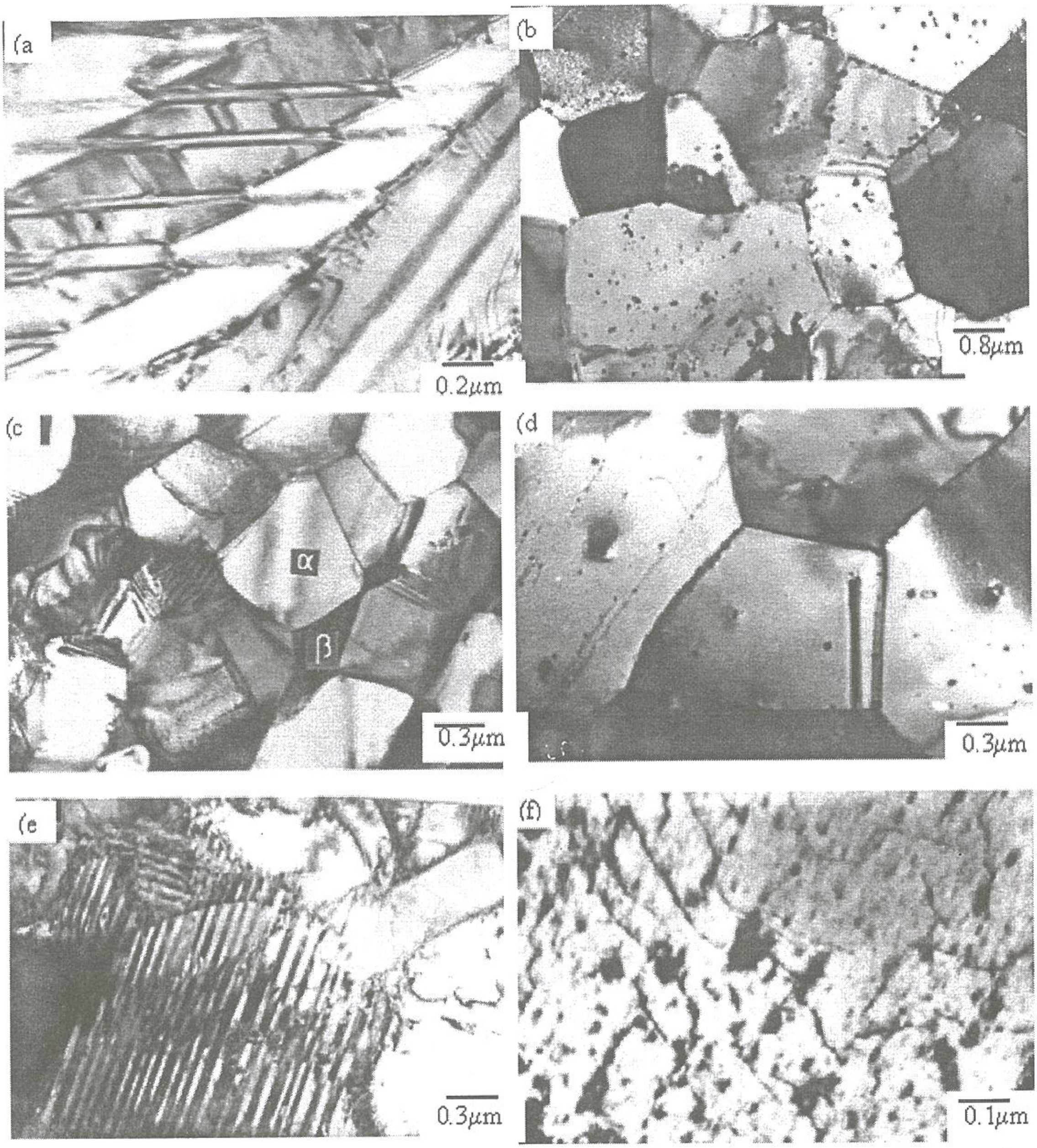

Fig. 8 Examples of bright field images obtained in TEM (a)Internally twinned martensite in Zr-2.5Nb alloy [15]. (b) Fine β precipitates in equiaxed α grains in Zr-1%Nb alloy [16]. (c)Extruded microstructure of Zr-2.5 % Nb pressure tube material [17] (d) secondary precipitate in α matrix in Zircaloy-2 cladding tube material. (e)Internally twinned γ hydride in Zr-20Nb alloy [18] (f) secondary precipitate in the irradiated Zircaloy-2 pressure tube material [19]

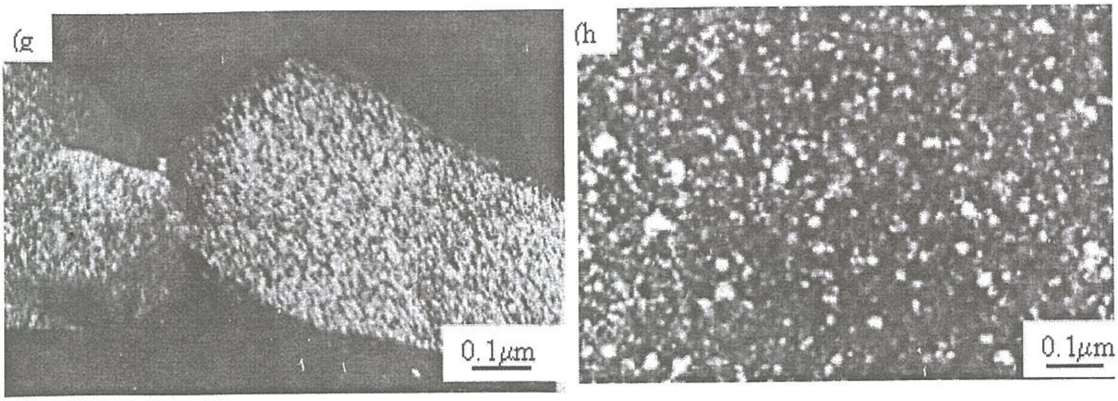

Fig. 8(contd.)Examples of dark field images obtained in TEM (g) w phase precipitation in the b phase in Zr-2.5 Nb alloy extruded pressure tube [17] (h) Nanocrystalline magnetic phase precipitates in a amorphous matrix [20]

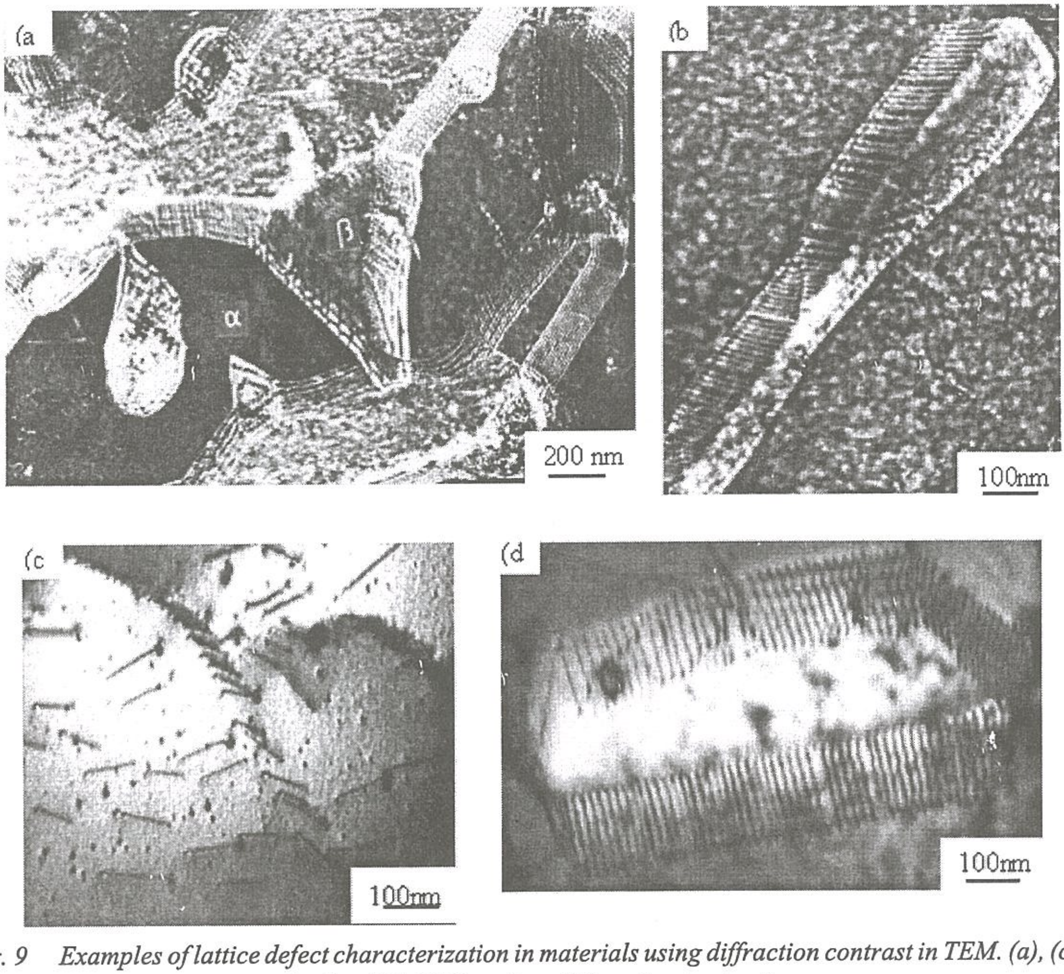

Fig. 9 Examples of lattice defect characterization in materials using diffraction contrast in TEM. (a), (c) (d) α/β interface in Zr-Nb alloy [21,22] Interface dislocation in zircaloy

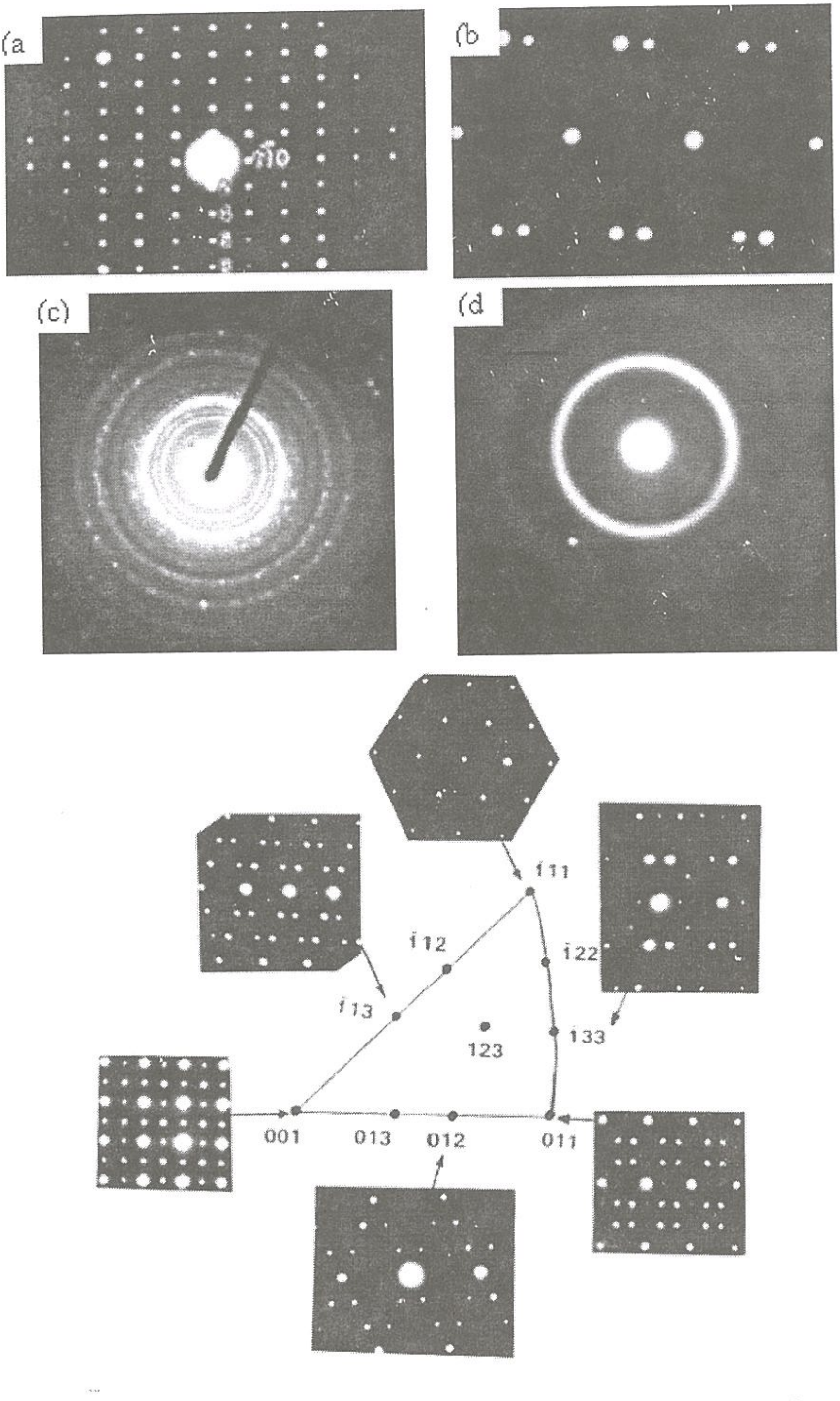

Fig. 10 Examples of SAD pattern obtained from (a) a single crystal (b)interface of internally twinned martensite [15] (c) nanocrystals [20] (d) amorphous phase (e) different zones obtained from multi-variant ω phase in TEM [22]

the main advance of CBED was to take electron diffraction from two to three dimensions through the development of "electron crystallography" where it has since competed with, and surpassed in many ways, the tremendous achievements of X-ray crystallography. For example, CBED can determine the point groups and space groups of extremely small crystals while, at the same time, the TEM is able to image them and carry out elemental analysis.

The spot diffraction patterns are obtained with parallel beam of electrons. In CBED convergent electron beam is focused on to the specimen then instead of a spot a disc is obtained which contains many fine details. The analysis of these fine structures it is possible to determine the specimen thickness, crystal structure and point and space group of crystals. In CBED high order Lauve zone(HOLZ) are also present they provide information from the crystal in the direction .parallel to the electron beam in addition to the two dimensional information obtained from the zero order Lauve zone (ZOLZ) [2-4].

High Resolution Transmission Electron Microscopy (HRTEM)

In this mode of microscopy phase contrast is used to form image. In order to obtain lattice images, a larger objective aperture has to be selected that allows many beams including the direct beam to pass (Fig. 11). The image is formed by the interference of the diffracted beams with the direct beam. If the point resolution of the microscope is sufficiently high and a suitable sample oriented along a zone axis, then HRTEM images are obtained. In many cases, the atomic structure of a specimen can directly be investigated by HRTEM. HRTEM can resolve object details smaller than 1 A , It can be used to image the interior structure of the specimen unlike atomic resolution scanning tunneling microscopy where only at the surface it can be resolved. HREM can provide information on the local structure and direct imaging of atom arrangements, in particular the structural defects, interface, and dislocations is obtained [10-13]. The examples are shown in Fig. 12 [15-17].

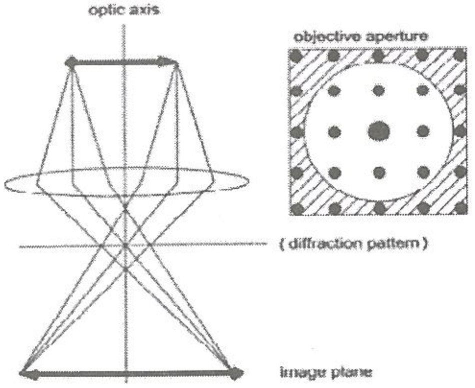

Fig. 11 Schematic showing ray diagram for image formation using phase contrast

The incident parallel electron beam interacts elastically while passing through the specimen, and the resulting modulations of its phase and amplitude are present in the electron wave leaving the specimen. The exit wave now passes through the imaging system of the microscope where it undergoes further phase change and interferes as the image wave in the imaging plane. However, the recorded image is not a direct representation of the samples crystallographic structure. For instance, high intensity might or might not indicate the presence of an atom column in that precise location. The relationship between the exit wave and the image wave is a highly nonlinear one and is a function of the aberrations of the microscope. The intensity distribution of the exit wave function is described by the contrast transfer function (CTF). A typical contrast function plot is shown in Fig. 13. CTF strongly depends on C_s, λ (accelerating voltage), defocus and spatial frequency, k. While this function is zero at the origin, it becomes positive for intermediate values of k. In this region of k, all information is transferred with positive phase contrast, i.e. the scattering centers (atom positions) appear with dark contrast Therefore, information in HRTEM images is consequently directly interpretable till the point resolution.

The direct interpretation of the image contrast is difficult because of strong electron-matter interaction (dynamical behaviour), the dependence on thickness of the crystal and CTF of the TEM (defocus) and the imperfect imaging system (aberrations like C_s, C_c). High resolution image contrast depends strongly on defocus, astigmatism, beam tilt, crystal tilt, etc. All of these cause the lattice

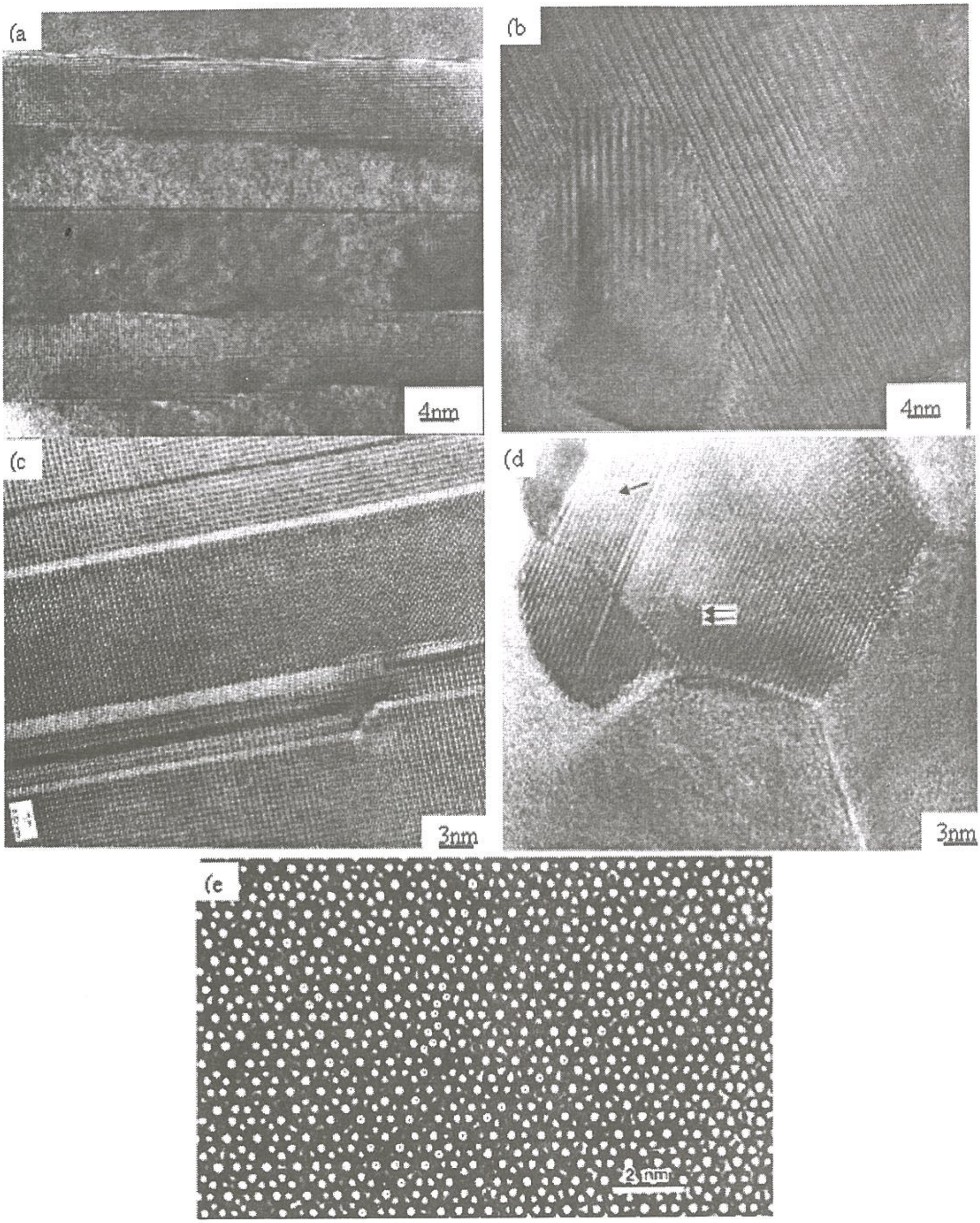

Fig. 12 Examples of high resolution transmission electron microscopy [23-25] (a) γ/γ *and* γ/α *interfaces in a TiAl alloy (b) stacking fault inside a nanograin (c) faulting in unidirectional* $Ni_{70}Mo_{25}Al_5$ *alloy (d) many nanograin boundaries, stacking fault and antiphase domain boundary (e) structure of quasicrystalline phase in a bulk metallic glass [25].*

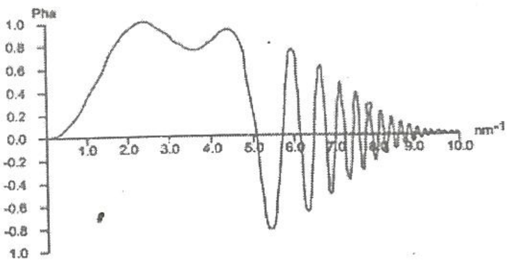

Fig. 13 Contrast transfer function

fringes to become stronger or weaker or move. An ideal structure image is when the lattice image is a good representation of the crystal structure, with heavy atoms as dark spots. To get a structure image specimen must be thin, crystal and beam must be on axis, astigmatism should be minimised, microscope must be at the correct focus (Scherzer focus) and lattice spacing must be within the resolution limit of the microscope. Image simulation is important for interpreting HRTEM images. The simulation of HRTEM images involves: modeling the crystal or defect structure, calculation of the propagation of the incident electron wave through the crystal, calculation of the transfer of the scattered wave by the optical system of the TEM and then comparison with the experimental micrographs. The most versatile approach is the multislice method.

Analytical TEM

Energy Dispersive Spectrometry

Combinations of probe-forming TEMs and electron and X-ray spectrometers gave rise to elemental analysis which, starting in the 1970s, was used to study many of the precipitation phenomena analyzed in the TEM in the 1960s. The advent of X-ray microanalysis in the TEM was shown to be an extraordinarily powerful addition to the arsenal of characterization weapons. Microanalysis in the TEM was only made commercially viable by the development of the energy-dispersive spectrometer (EDS). The EDS was small enough to be positioned inside the stage of a TEM and so could gather sufficient counts for quantification at high spatial resolution.

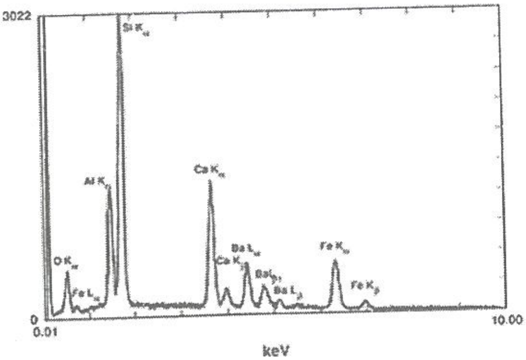

Fig. 14 Schematic showing a typical EDS spectra obtained in TEM

The characteristic X-rays are obtained when electron interact with the specimen. The measurement of the wavelength (or energy) of each characteristic-ray that is emitted enables us to find out which elements are present in the specimen (qualitative analysis). And measurement of number of intensity tells us about how much of the element is present (quantitative analysis). The TEM's are generally equipped with EDS detection system. A silicon/ lithium semiconductor energy dispersive X-ray detector is used. A window is provided to protect it from contamination from the specimen chambers. However, because of this window absorption of low energy X-ray makes detection of light element difficult (For Be window below Na). Modern windowless detectors can extend the analytical range down to boron. However, such detectors need more careful operation. Modern EDS detectors coupled with large collection angle a reasonable spectrum is be obtained in short time. Qualitative analysis of all the elements of the sample in TEM-EDS is extremely rapid. A typical spectra obtained is shown in Fig. 14. EDS are generally associated with rather poor resolution and accuracy but since it can be placed closed to specimen analysis is rapid and spectrum of all elements can be obtained simultaneously.

Since in TEM electron beam is normally not focused to large area of a specimen so good spatial resolution is not obtained. To overcome this STEM mode is used where electron probes can be focused down to the size of 1nm. This allows analysis of a spot, line or area of a specimen in same way as in

SEM. The spatial resolution in TEM/STEM is controlled by the nature of specimen, concentration of the element being analyzed, probe size and thickness of specimen. In conventional TEM it is possible to obtain a resolution better than 5nm. In TEM since surface area is large, great care must be exercised to minimize the surface effect.

The quantitative analysis requires accurate assessment of the volume from which X-rays are generated. This volumes depends on the electron beam energy, the average atomic weight of the sampling volume, the wavelength of characteristic X-rays, the absorption coefficients of the specimen. Another factor is that X-ray generated deeper in the surface may escape. However for thin samples in the case of TEM fortunately fluorescence and absorption effect is much less and can be ignored. Cliff and Lommer method is used for thin film analysis which estimates the compositions reasonably well [5-6]. A scaling factor K for each element with respect Si has been measured experimentally. In TEM the detection limit is typically of the order of 0.1 to 0.5 wt%. If sample is thicker than 50 nm than absorption corrections should be made.

TEM-EDS is very useful microanalysis technique where distribution of phases are at very fine scale. Now in a nano-science and nano technology it is making many valuable contributions in the study of nano-particles, phase transformations and phase equilibria.

Electron Energy Loss Spectroscopy (EELS)

During inelastic scattering of electron it suffers from energy loss and if this loss is nearly 1eV then it is possible to determine the composition and other information. Much of the chemical interest in EELS stemmed initially from the possibility of carrying out accurate chemical analyses on microscopic samples. The current consensus is that EDX provides a better analytical technique for all but the first row elements and even for the first row elements, excluding lithium and beryllium. The real power of EELS, in the study of core-edges, comes from the high resolution imaging and this technique yields information about a very wide range of properties including electron densities, chemical analyses, band structure information, information about the oxidation state and the hybridization state of particular atoms, information about the local coordination including bond lengths, and information about the momentum density [2,7]. A typical electron energy loss spectrum is shown in Fig. 15.

EELS spectra consists of three parts

Zero-loss peak at 0 eV:

It mainly contains electrons that still have the original beam energy E_0, i.e., they have only interacted elastically or not at all with the specimen.. The smallest energy losses arising from the excitation of phonons, or vibrations of the atoms (10-100 meV) are also included in the zero loss peak. Since there is no useful information in it, the zero-loss beam is often omitted during spectrum collection.

Low-loss region (< 100eV)

The Plasmon peak arises from the excitation of collective oscillations of the valence or conduction electrons,(energy 5 to 30eV). Since this is a collective excitation it depends on the many-body properties of the electron-gas and in particular on the density of the conduction or valence electrons. In this region, transitions between valence bands and low lying unoccupied states are also observed. Since the plasmon generation is the most frequent inelastic interaction of electron with the sample, the intensity in this region is relatively high. Intensity and number of plasmon peaks increase with specimen thickness.

High-Loss region (> 100eV)

core-edges are observed when the energy transfer exceeds the binding energy of the electrons in a particular shell. The edges are characteristic of the element whose electrons are excited and their energy and height can be used for elemental analysis.

A critical energy of incident electron is required to expel inner-shell electron, which leads to ionization edges in the spectrum at energy losses that are characteristic for an element. Thus, EELS is complementary to X-ray spectroscopy, and it can be utilized for qualitative and quantitative element analysis as well. In particular, the detection of light elements is a main task of EELS. Compared to the

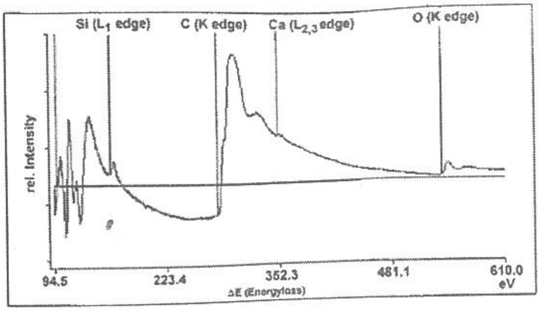

Fig. 15 Schematic showing a typical EELS spectra obtained in TEM

plasmon generation, the inner-shell ionization is a much less probable process, thus gives low intensity peaks. In the high-loss region, the amount of inelastically scattered electrons drastically decreases with increasing energy loss, thus small peaks are superimposed on a strongly decreasing background. Because of the low intensity, the representation of the high-loss region is magnified.

In solids, however, the density of states in the region of the Fermi level may be quite complex with both empty and partly filled bands and this is reflected in the electron energy-loss near-edge structure or ELNES, (few volts to about 20 volts). Since this near edge structure depends on the density of unoccupied states in the region of the Fermi level it provides information about the electronic structure of the sample. In addition, it is also possible to observe chemical shifts in the edges making it possible to identify the oxidation state and the number of inequivalent sites occupied by particular element. EXEIS"S or extended electron energy-loss fine-structure this is observed when the ejected electron is scattered back by the surrounding atoms and interferes constructively or destructively with itself. The period of the resulting modulation in the signal may he used to determine nearest neighbor distances and the amplitude of the modulation gives a measure of the coordination number of the atom under consideration. The EELS spectroscopy with high local resolution is performed by following two different methods. In first method EELS is performed in STEM mode where a region of the sample is selected, and an EELS is measured on each spot of the defined grid (serial measurement). Where as in the second method in EFTEM mode using an energy filter an energy range is selected, image is recorded with electrons of this energy (parallel measurement). Using dynamical scattering, EELS can be made sensitive to the location of atoms within the unit-cell [7].

Scanning Transmission Electron Microscopy (STEM)

In STEM, a small, convergent electron beam is scanned over a defined area of the sample in which elastically scattered electrons for direct and diffracted beams (BF/DF) and incoherent scattering (Z contrast) signal are used. At each spot, the generated signal is simultaneously recorded by selected detectors, building up an image. The advantage is that such a convergent beam is used to gain a highly localized signal from the specimen in analytical TEM (e.g., EDX, EELS), and thus the combination of STEM with analytical methods is a main application in practical work. Three types of detectors are used to obtain STEM images:

Bright field (BF) detector is placed at the same site as the aperture in bright field in TEM and detects the intensity in the direct beam from a point on the specimen. In the BF-STEM image, the contrast is similar to that in bright field images. The crystalline particles appear with dark contrast since they are crystalline and the heaviest scatterers in this system.

The annular dark field (ADF) detector is a disk with a hole in its center where the BF detector is installed. The ADF detector uses scattered electrons for image formation, similar to the dark field mode in TEM. The measured contrast mainly results from electrons diffracted in crystalline areas but is superimposed by incoherent Rutherford scattering. In the ADF-STEM image, the crystalline particles appear with bright contrast because of diffraction and incoherent scattering. Both BF and ADF detectors are used for phase analysis, particle size, and characterization of defects and grain boundaries.

The high-angle annular dark field (HAADF) detector is also a disk with a hole, but the disk diameter and the hole are much larger than in the ADF detector. Thus, it detects electrons that are scattered to higher angles and almost only incoherent Rutherford scattering contributes to the image. Thereby, Z contrast is achieved. In the HAADF-STEM image, only the incoherently scattered electrons contribute to the image, which nonetheless appears to be very similar to the ADF-image. In the high-angle annular dark field (Z contrast) image, the phases, which have high atomic numbers Z compared to the matrix, are imaged as bright dots. Thus detection of small clusters or even single atoms of a heavy metal in a matrix of light elements (Z-contrast) and direct visualization of structures and defects is possible with this.

In STEM mode the beam can be localized on a certain point in the image and used to measure an EDX and/or EEL spectrum at there. Moreover, line scans and mappings can be obtained by this powerful technique.

TEM Sample Preparation

Due to the strong interaction between electrons and matter, the specimens have to be rather thin (<100 nm) for TEM investigation [2]. Thus, bulk materials have to be thinned to make them electron transparent. The sample preparation method should not make any changes in the specimen during preparation. The sample should be strong enough to handle.

The method of thinning sample depends on initial form of material and what information is needed.

(a) Powders: If particle size is small enough to be electron transparent on its own (<100nm) then small amount of samples are added in a solvent and for better dispersion of particle they are ultrasonically mixed. A small drop of suspension is dropped on carbon-coated amorphous grids and if the particles are large then they are dispersed in a resin and sliced by microtome technique

(b) Bulks: In case of metals, bulk specimens can be prepared by cutting the sample into thin slices using a diamond saw. A disc punch is used to punch out 3-mm-diameter disks from the slice. For brittle and hard samples such as ceramics and semiconductors mechanical pre-thinning is carried out using SiC sandpaper of increasing grit sizes (60 - - 600 grit sizes). Starting materials is ground to slabs of about 500 um in thickness. Then the disc can be cut using ultrasonic disc cutter. The disc is further grounded using disc grinder upto a thickness of 100mm. Thinned disk is subsequently milled on a dimpling device.

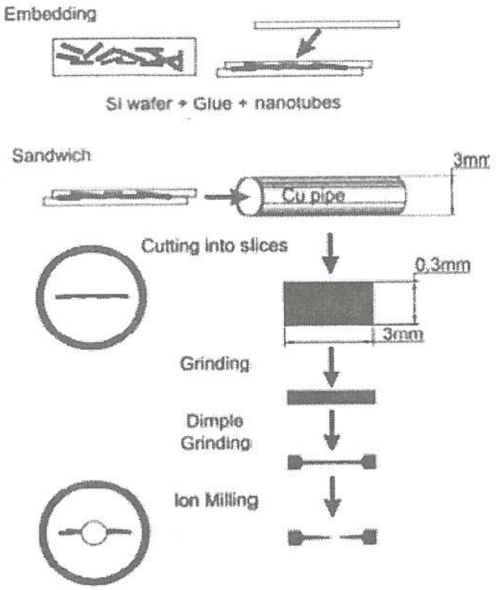

Fig. 16 TEM sample preparation technique

Thinned and dimpled samples are further thinned either by electrochemical jet thinning method or by ion milling technique. In jet thinning method sample is made anode and dissolved by applying current (Fig. 16)

Dimpled samples are thinned by ion Milling. In this technique thin samples are bombard with energetic Argon ions which, sputter away material from both side of samples until it becomes transparent. The ion milling parameters e.g. ion current, angle of incidence, sample temperature, sample rotation is set as per the nature of the sample. The sputtering rate depends on: flux and velocity of the incident particles, angle of incidence, relative masses of the specimen atoms, cohesive energy of the specimen atoms and chemical interactions between incident particles and the specimen. High ion current leads to more damage of the sample. But, smaller angle of incidence results in less ion implantation and less damage.

Cleaving technique is used to examine brittle single crystals. This technique is mainly used to examine the epitexial semiconductor layers. Ultramicotomy is an slicing instrument used for slicing biological samples which is subsequently mounted on a grit for TEM examination

Specimen Preparation by Focused Ion Beam (FIB) Milling

Like in field emission gun, gallium ions can be used extracted from the tip of few nanometer width and accelerated using a potential of tens of kilovolts. Such field emission guns has a very small source size and energy spread and can be used to produce fine beam using a aperture and demagnifying lens. This is used to form an image in a focused ion beam microscope. The beam is used for precise sectioning of samples (eg. Semiconductors). This is only technique where image can be formed and simultaneously features can be sectioned for TEM examinations.

There are two different approaches to TEM sample preparation with FIB: lift out and traditional. Preference between the two depends on specific analytical conditions such as sample compositions. The life-out technique uses the milling action of the ion beam to excavate materials from both sides of the final thin section, and then cut the section free from the bulk specimen. An automated process lifting-out the delicate specimen and transferring it to a TEM specimen grid, is available in some FIB system. The traditional approach requires the use of manual cleaving and polishing techniques to create a pre-FIB sample that is small enough to fit into the TEM specimen chamber and thin enough (less than 50 mm) to minimize the amount of material that must be removed by the FIB. This pre-FIB specimen is then glued to TEM specimen grid and milled in the FIB to its final electron-transparent thickness [14].

Aberration Corrected Microscopes

The advent of aberration corrected analytical transmission electron microscopes removes the major barrier to resolution that has existed since its invention and has resulted in sub angstrom lattice resolution. In probe corrected microscopes beams are used for imaging and spectroscopy, with enormous improvement in sensitivity for single atom detection and the investigation of interfacial electronic structure.

Now commercial TEM's fitted with both probe and imaging aberration correctors and an in column energy filter are available. The correctors are based on a design [15] in which the primary elements consist of a pair of strong hexapoles and two round-lens doublets. In practice adjustment of the imaging corrector is achieved using a Zemlin tableau of diffractograms calculated from images of a thin amorphous foil and recorded at several tilt azimuths with constant tilt magnitude. In these microscopes the spherical aberration and other aberration coefficients may be set to zero for pure amplitude contrast, or the spherical aberration coefficient may be set to a small negative value for optimum phase contrast.

Summary and Conclusions

The electron microscope has played a major role in materials characterization in its principal transmission and scanning forms. Conventional and advanced TEM has been effectively employed for imaging, characterizing defects and spectroscopy. TEM is becoming more and more indispensable tool in the field of science and nanotechnology. Tremendous improvement has been made in TEM but still TEM remains an operator-intensive instrument and requires great expertise to derive the best performance from the equipment. TEM is also most often limited in its capabilities by the quality of the thin specimens, and this is the reason often great emphasis is placed on the detailed experimental procedures necessary to create thin specimens and extract TEM images and diffraction patterns. X

References

1. M. Knoll and E. Ruska. Z. Phys. 78 (1932), p. 318.
2. D.B. Williams and C.B. Carter. Transmission Electron Microscopy—a Text for Materials Science Plenum Press, New York (1996).
3. P.B. Hirsch, A. Howie, R.B. Nicholson, D.W. Pashley and M.J. Whelan. Electron Microscopy of Thin Crystals (2nd edn ed.), Krieger, Huntington, NY (1977).
4. B.F. Buxton, J.A. Eades, J.W. Steeds and G.M. Rackham. Phil. Trans. R. Soc. 281 (1976), p. 181.

5. J.W. Steeds. In: J.J. Hren, J.I. Goldstein and D.C. Joy Editors, Introduction to Analytical Electron Microscopy Plenum Press, New York (1979), p. 387.

6. D.B. Williams, J.I. Goldstein and D.E. Newbury Editors, X-ray Spectrometry in Electron Beam Instruments Plenum Press, New York (1995).

7. R.F. Egerton. Electron Energy-Loss Spectrometry in the Electron Microscope (2nd edn ed.), Plenum Press, New York (1996).

8. Lupini, A. R. and Krivanek, O. L., in Electron Microscopy 1998, Proc. ICEM14, Cancun, ed. H. A. Calderon Benavides and M. J. Yacaman. Institute of Physics, Bristol, 1998, p. 59.

9. L. Reimer Editor, Energy-Filtering Transmission Electron Microscopy Springer-Verlag, Berlin (1995).

10. Kabius, B., Urban, K., Haider, M., Uhlemann, S., Schwann, E. and Rose, H., in Electron Microscopy 1998, Proc. ICEM14, Cancun, ed. H. A. Calderon Benavides and M. J. Yacaman. Institute of Physics, Bristol, 1998, p. 609.

11. P.E. Batson. Nature 366 (1993), p. 727.

12. Watanabe, M. and Williams, D. B., Ultramicrosc., 1999, 78, 89.

13. C. Jeanguillaume and C. Colliex. Ultramicrosc. 28 (1988), p. 252.

14. P. Goohew, J. Humpherys and R. Beanland, Atext book on Electron Microscopy and Analysis, 3rd Ed., Taylor and Francis, London,2001

15. D. Srivastava, Madangopal K., S. Banerjee and S. Ranganathan, Acta Metallurgica et Materialia, 41 (1993) 3445-3454.

16. S. Neogy, D. Srivastava, J.K. Chakravartty and G.K. Dey and S. Banerjee Metall. Meter Trans. Vol. 38, 2007, pp485-498.

17. D. Srivastava, G. K. Dey, and S. Banerjee, Metallurgical and Materials Transitions, 26A, (1995) 2707.

18. D. Srivastava, S. Neogy, G.K. Dey, S. Banerjee and S. Ranganathan, Mater. Sc. and Engg. A, Vol.397, pp 138-144

19. D. Srivastava, R. Tewari, G. K. Dey, B. P. Sharma and D. N. Sah, BARC Report, No. BARC/2005/E/023, 2005.

20. A.P. Srivastava, D. Srivastava and G.K. Dey J. Mag. and Magnetic Materials,, Vol. 306, 2006, pp 147-155.

21. S. Banerjee, G. K. Dey, D. Srivastava and S. Ranganthan Metall. and Maters. Trans., 28, (1997) 2201

22. D. Srivastava, Ph.D. Thesis, IISC, Bangalore, 1997

23. G. K. Dey, R. T. Savalia, S. Neogy, R. Tewari, D. Srivastava, S. Banerjee, Int. J. of Nano science . 5-6 (2005) 901.

24. G. K. Dey, S. Neogy, R. T. Savalia, D. Srivastava, and S. Banerjee, Tans. IIM, No.6, 2005, pp1113-1123.

25. D. Srivastava, G. K. Dey, and S. Banerjee, Metall. and Maters. Trans., 26A, (1995) 2707.

Scanning Electron Microscopy

Dr. Madangopal Krishnan did his B.Tech. in Metallurgical Engineering from BHU-IT, Varanasi in 1983. He joined the 28th batch of BARC Training school in 1984 and later Material Science Division in 1985. He did his Ph.D. in metallurgical engineering from BHU-IT and post doctoral work at University of Cincinati, USA. His fields of interest include, electron microscopy, phase transformations in metals and alloys, martensitic transformations, Shape memory effects, engineering applications of shape memory alloys, etc. He has received several awards, namely, Bhabha award for standing first among the metallurgical engineering trainees of BARC training School, INSA-JSPS short term research fellowship, outstanding research investigator award of DAE-SRC and outstanding referee award & citation received from Acta Materialia Inc.

Introduction

In the scanning electron microscope (SEM), Fig.1.1, sample surfaces are imaged by scanning an energetic electron beam (over the surface) in a raster scan pattern. The electrons interact with the material producing a variety of signals that contain information about the surface topography, composition, etc. Electronic devices, Fig.1.2, are used to detect and amplify the signals and display them as an image on a cathode ray tube with its raster scanning synchronised with that of the electron beam. The brightness on the CRT is proportional to the variation of signals reaching the detector. The displayed image is therefore a distribution map of the intensity of signal emitted from the area of specimen being scanned. In earlier SEMs, the image (displayed on a dedicated high resolution CRT) was captured by photography. However, in modern instruments the digitized image is both displayed and grabbed on a computer monitor.

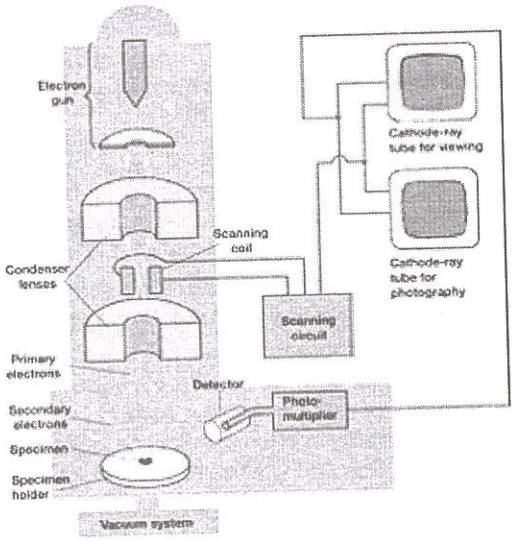

Fig. 1.1 Schematic showing the major components of a SEM.

The electrons of the probe are emmited from a cathode and accelerated towards the anode. The most common cathode used in the SEM is the tungsten filament thermionic emitter. Other electron sources include lanthanum hexaboride (LaB6) thermionic gun, cold-cathode field emission gun and thermally-assisted Schottky field emission gun. Typically in the SEM, the electron beam has an energy ranging from a few hundred eV to as much as 40 keV. The beam is focused by condenser lenses and an objective lens to a very fine focal spot of 0.5 nm to 5 nm. The beam is scanned over a rectangular area of the sample surface by horizontal and vertical deflection scan coils. Magnification results from the ratio of dimensions of raster on specimen to raster on display device. Since the display screen has a fixed size, higher magnifications are obtained by reducing the size of raster on specimen. In this way, magnification can be varied over 5 orders of magnitude, from x25 or less to x 250,000 or more.

Dr. Madangopal Krishnan, Materials Science Division, Bhabha Atomic Research Centre, Mumbai 400 085;
E-mail: madangk@barc.gov.in

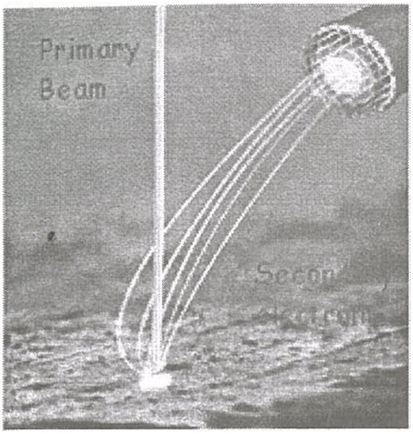

Fig. 1.2 Low energy secondary electrons are drawn towards the ET detector by the positive grid bias.

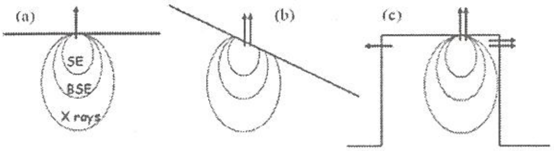

Fig. 1.3 (a) the primary beam loses its energy within a tear drop shaped volume ('interaction volume'). While the low energy SE can escape only from the uppermost part of the interaction volume, X-rays can from the deepest end and BSE from an intermediate depth; (b) and (c) inclined surfaces and edges appear brighter as higher amounts of SE can escape in these situations.

When the electron beam interacts with the sample, electrons loose energy by repeated scattering and absorption within a teardrop-shaped interaction volume, Fig.1.3(a). The size of the interaction volume (100 nm to around 5 ìm) depends on the electron energy, atomic number of interacting atom and density of specimen. The interactions within this volume leads to backscattered electrons by reflection of high-energy electrons through elastic scattering, low energy secondary electrons (<50 eV) by inelastic scattering, characteristic X-rays and light (cathodoluminescence).

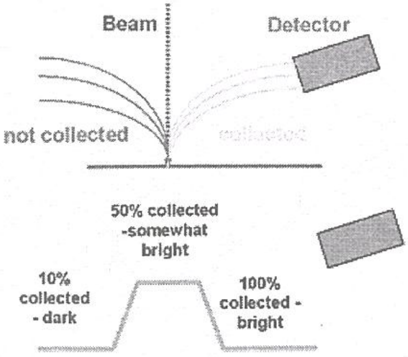

Fig. 1.4 Topographic contrast of SE images is enhanced by the position of the detector with respect to the feature ('detector efficiency contrast').

Typically, secondary electrons are used to image sample topography as their origin is limited to a few nanometers of depth (on account of their low energy). Universally, the Everhart-Thornley scintillator-photomultiplier type detector, Fig.1.2, is used to detect secondary electrons. Figure 1.3 (b) and (c) shows that steep surfaces and edges will tend to be brighter than flat surfaces as more secondary electrons can escape from such regions. The contrast due to this mechanism ("topographic contrast") and due to detector orientation ("detector efficiency contrast"), Fig.1.4, results in an image that is well-defined and three-dimensional in appearance, Fig.1.5. An helpful way of intrepreting SE topographic images is provided in Fig.1.6.

The yield of backscattered electrons (brightness) generally increases with the average atomic number. Therefore, the image generated using backscattered electrons (BSE) have a contast which reflects the variation of chemical composition, Fig.1.5. On the other hand, the topographic contrast is weak as BSE are generated from lower regions of the interaction volume. Topographic contrast can be enhanced by changing the detector inclination (detector efficiency contrast) or by adding SE information. The latter approach, Fig.1.5, is preferred as the image shows both topogaraphic and chemical contrast. Generally, BSE are detected using a solid state detector placed above the sample, concentric with the electron beam. This position of the detector produces better atomic number contrast as BSE collection increases with solid angle at sample. BSE can also be used to form

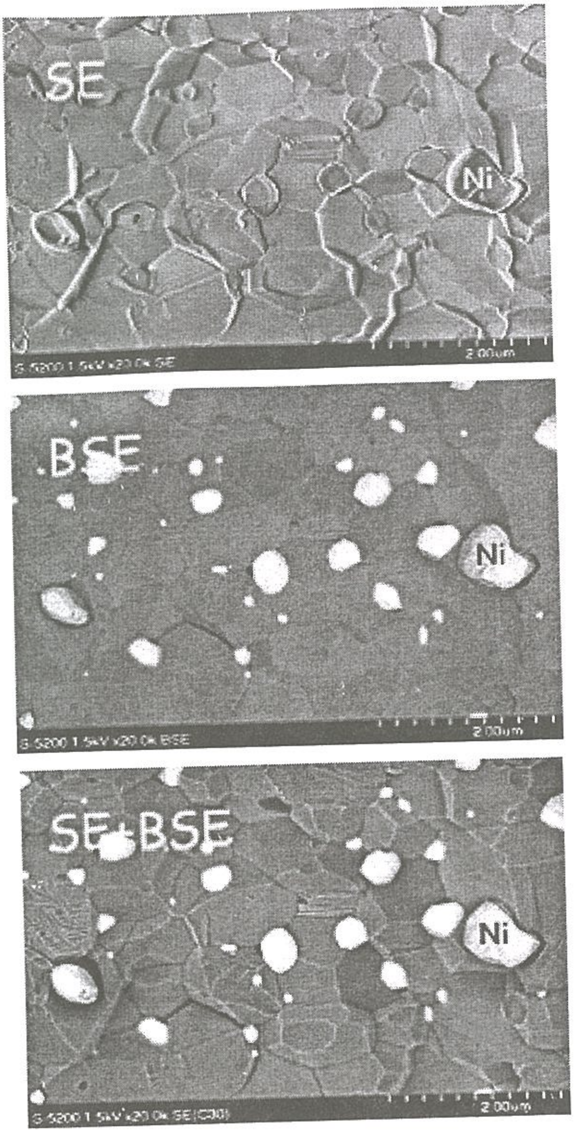

Fig. 1.5 SEM images of an sample with Ni particles in Alumina matrix: strong topographic contrast is obtained in SE image and chemical contrast in BSE image. These two information's are superimposed by mixing the signals from the two detectors.

an electron backscatter diffraction (EBSD) image (see #2).

X-ray mapping with characteristic x-rays are the third most common imaging mode.

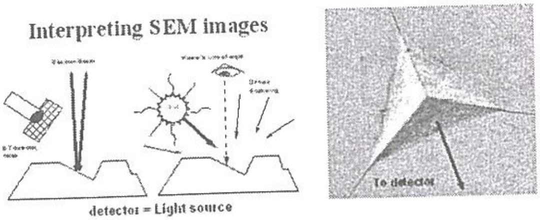

Fig. 1.6 The topographic contrast of SE images is interpretated as shown in the schematic on the left hand side. Thus the image on the right hand side is of a pit and not of a pyramid.

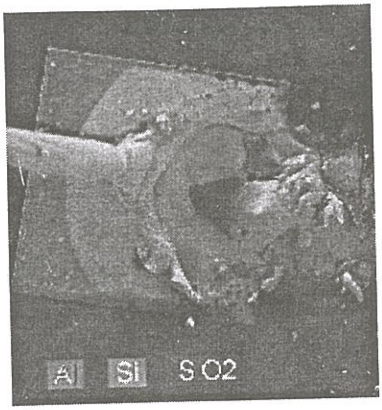

Fig. 1.7 X-ray map of a ruptured aluminium contact on a silicon semiconductor component

Characteristic X-rays are emitted when the electron beam removes an inner shell electron from the sample and a higher energy electron drops to fill it. These characteristic x-rays are commonly detected using Si(Li) detector based energy dispersive spectrometers. X-ray elemental maps, Fig.1.7, are generated by selecting the element (wavelength) to be detected during scanning and using the corresponding signal for imaging.

The spatial resolution of the SEM depends on the size of "spot" or the footprint of electron beam on the sample. The spot is smaller when the beam crossover size is small and spot size demagification (through electron optics) is high. Thus, field emission gun SEMs at low working distances show the highest resolution. Practically, however, the resolution is limited by the size of the interaction volume as secondary electrons are generated (known

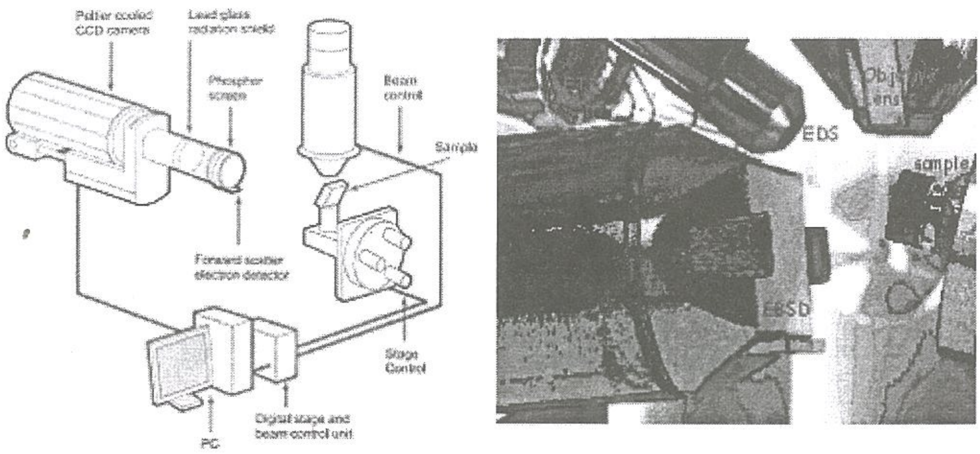

Fig. 2.1 Left hand shows a schematic of the set-up for EBSD. Right hand figure shows the in-chamber view of the set-up. Also seen are an ET (Everhart-Thornley) detector for topographic imaging using secondary electrons and an EDS detector correctly positioned for combined EBSD-EDS Phase ID and Phase Mapping.

as SE II) when BSE emerge from the surface. The dimensions of the SE II skirt around the SE I (those produced by primary beam) is roughly that of the interaction volume. Therefore, higher resolutions are obtained with smaller interaction volumes at lower acceleration voltages. However, depending on the instrument, the resolution of the SEM is between 1 nm and 30 nm.

The purpose of this article is primarily to introduce the reader to the versatility of the scanning electron microscope. The remaining article will review a few of the recent developments which have enhanced the capability and versatility of this remarkable instrument.

EBSD

In the last 10 years or so, electron backscatter diffraction technique, EBSD, has developed into a powerful tool for crystallographic analysis of materials using scanning electron microscope. For generating an EBSD patterns, a beam of electrons is focused at a point of interest on a tilted crystalline sample (Fig.2.1). A fraction of the electrons entering the crystal get quasi-elastically and incoherently scattered in all directions to form a divergent source of electrons close to the sample surface. Some of these electrons are directed towards atomic planes at angles which satisfy the Bragg relation: $n\lambda = 2d \sin\theta$ and get coherently diffracted. Figure 2.2 shows that the loci of all such diffracted electrons emerging from a point source, are pairs of cones centered on the lattice plane normal, having an apex angle of $180° - 2\theta$ and enclosing 2θ between. Since the Bragg angle θ is only ~1° (@ 15 kV accelerating voltage),

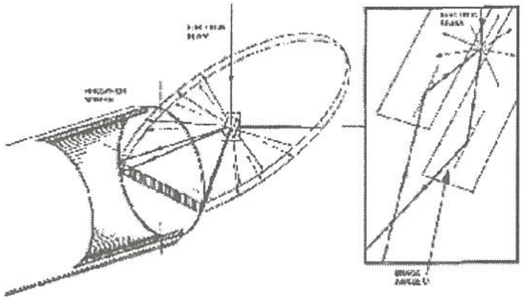

Fig. 2.2 At the point of interaction there forms a divergent 'point' source of inelastically scattered electrons. The scattered electrons traveling at Bragg angles to the crystal planes are coherently diffracted as pairs of cones that intersect the phospher screen of the EBSD camera (Fig. 2.1) in almost straight and parallel ' Kikuchi' lines.

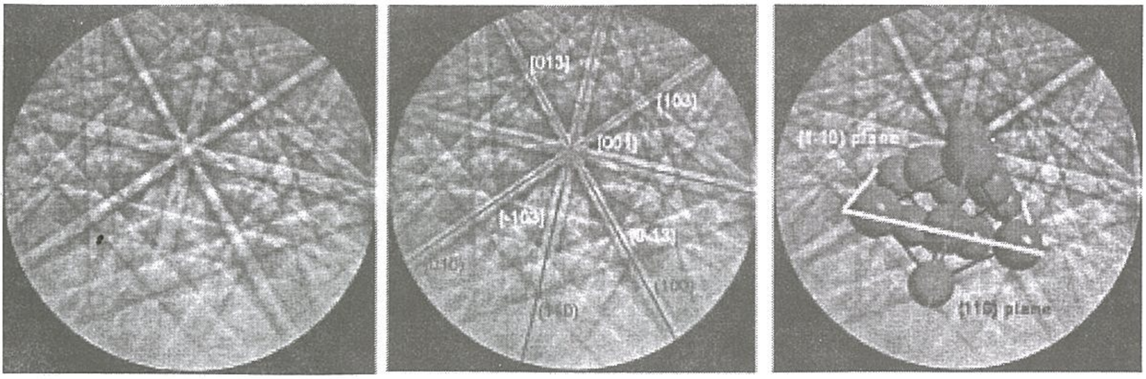

Fig. 2.3 (a) Shows a typical EBSD: the bright lines are Kikuchi bands; (b) and (c) shows the steps in automatic determination of crystal orientation band detection (b) and indexing (c)

the cones are large and intersect a screen (Fig.2.2), placed tangential to the propagation sphere of scattered electrons, in pairs of almost straight and parallel 'Kikuchi' lines. Figure 2.3a shows an example of EBSD patterns, wherein bright Kikuchi bands are seen crisscrossing on a relatively high background. It is easy to notice that the EBSD patterns obtained from bulk samples bear several similarities to the Kikuchi patterns obtained from thin foils in the transmission electron microscope. Since each band corresponds to a set of lattice planes, their Miller indices can be obtained from the widths and the angles between the bands (Fig.2.3b). The crystal orientation is obtained by the successful indexing and identification of the zones in the EBSD pattern (Fig.2.3c).

During an EBSD scan, Fig.2.1, the sample is steeply tilted, usually to about 60° or 70°. This is to allow the escape of the diffracted electrons from the crystal. The screen, which is a retractable transparent phosphor screen, is positioned close to the tilted sample, between 20 and 40 mm from the point of focus of the beam on the sample. The EBSD pattern on the phosphor screen is acquired by a highly sensitive camera and is transmitted to a computer for further processing. The same computer also controls the beam positioning for acquiring EBSD patterns from point locations and for stepwise beam scanning in a technique known as "orientation imaging microscopy, OIM".

The OIM technique is based on consecutive acquisition of electron diffraction patterns from points of a scan grid on a steeply inclined flat sample surface. Computer algorithms that automatically identify Kikuchi lines and index diffraction patterns, analyze individual EBSD patterns to provide the crystallographic orientation and quality of diffraction pattern at each scan point. From this data the crystal orientation maps or microstructure of the scanned area is reconstructed to provide a variety of information such as, size, form, nature and distribution of different phases, nature of grain boundaries, local crystal orientation and texture or misorientation distribution. The EBSD technique, on the other hand, is also used to investigate the structure of crystals, i.e. lattice symmetry and lattice parameters, and can replace the TEM for a large range of crystallographic work. To this end, the EBSD technique involves relatively simple sample preparation and allows the observation of much larger areas at high spatial resolutions.

Combined EDS and EBSD analysis has opened up two new characterization techniques: Phase ID and Phase Mapping. In Phase ID, Fig. 2.4, the EDS data and EBSP (electron back scattered diffraction pattern) are simultaneously gathered from a feature (matrix, precipitate) in the sample. The feature is identified by searching available structure databases using the information of its structure and composition obtained from EBSP and EDS, respectively. Phase maps (Figs.2.5 and 2.6) were put together from phase ID measurements carried out on a large number of grid points superimposed on the microstructure. In practice, however, successful phase mapping requires limiting the database search

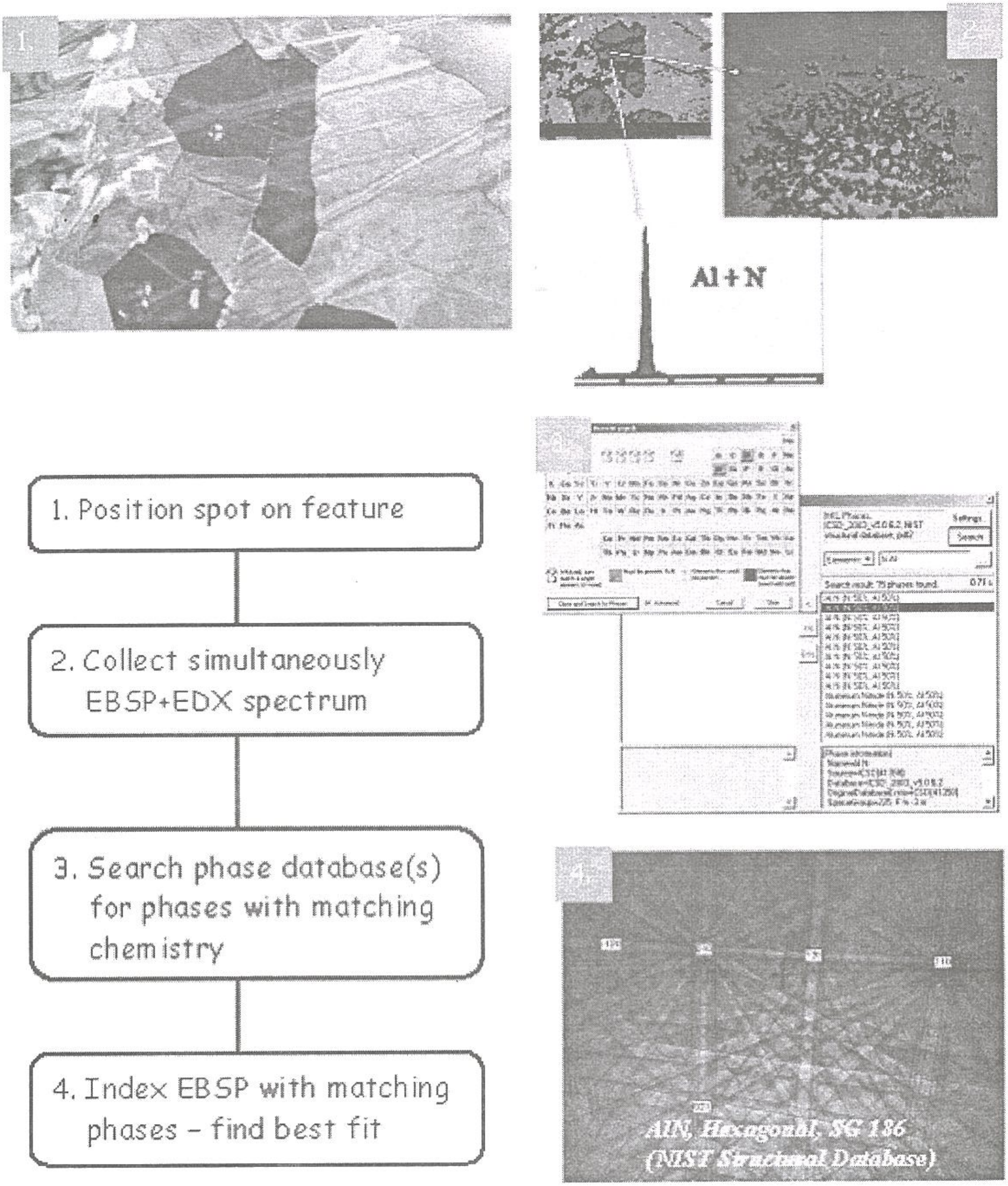

1. Position spot on feature
2. Collect simultaneously EBSP+EDX spectrum
3. Search phase database(s) for phases with matching chemistry
4. Index EBSP with matching phases - find best fit

Fig. 2.4 Phase ID by combined EBSD-EDS: combined EBSP and EDS spectrum are used to determine identity of the phase by search and match of available databases.

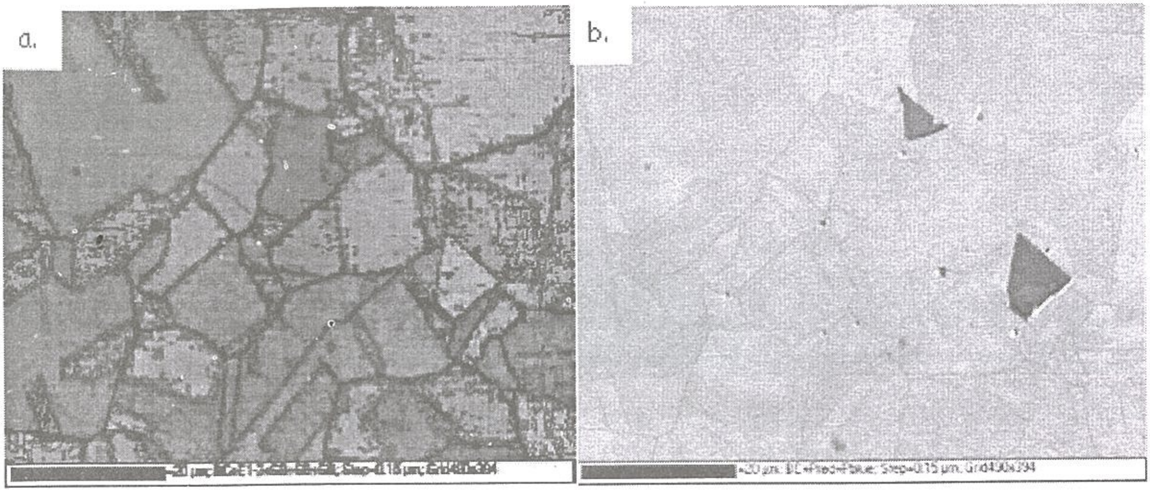

Fig. 2.5 Second phase in austenitic stainless steel: (a) EBSD Euler colour map; (b) EBSD phase map (yellow: austenite; blue: TiN)

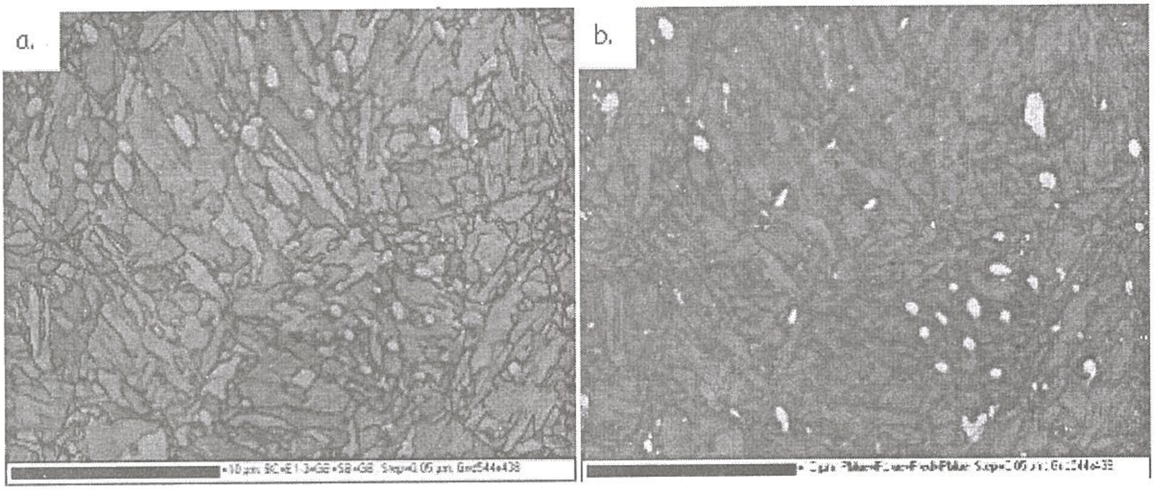

Fig. 2.6 Carbide and nitride precipitates in tempered martensite: (a) EBSD Euler colour map; (b) EBSD phase map (blue: Cr_2N, yellow: $(Cr,Fe)_{23}C_6$; red: bcc martensite)

by a foreknowledge of phases that may be encountered in the microstructure. Also, a high speed EBSD camera with a large area Si(Li) detector or Silicon Drift Detector are essential for minimizing the total scan time. Usually, such a system is integrated with the focus of EDS and EBSD set coplanar at the same working distance in a SEM equipped with a bright Schottky emitter. In addition to phase mapping, high speed EBSD cameras (with speed higher than 300 fps) are also essential for 3D-EBSD and in-situ deformation studies.

ESEM

The high vacuum required for SEM limits the imaging of insulators, biological samples, wet samples and liquid samples. In the case of insulators, negative charge accumulates on the surface and deflects the primary electron beam. Usually, these

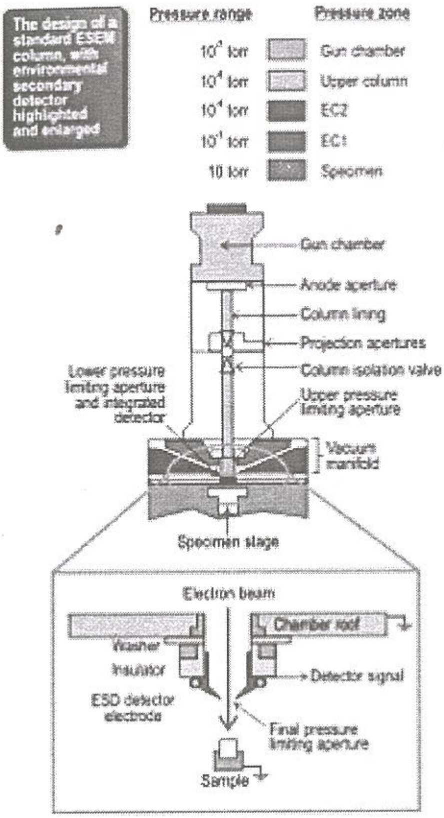

Fig. 3.1 Typical ESEM column showing the pressure limiting apertures

charging artifacts can be eliminated by depositing a conductive layer like carbon or gold on the specimen surface prior to examination. However, coatings obscure fine details of the sample. In case of wet and damp samples such as, paints, inks, emulsions and biological tissue, the lengthy specimen preparation techniques required to remove or fix the water before imaging, increase the risk of introducing artefacts.

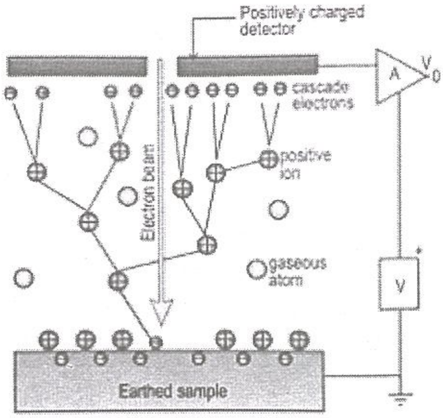

Fig. 3.2 Cascade amplification process in the GSED

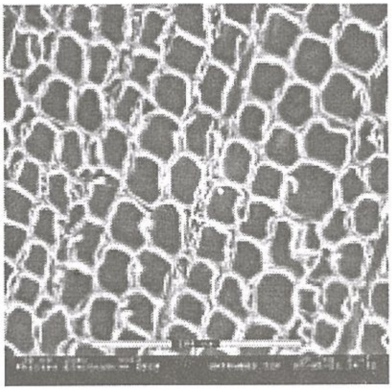

Fig. 3.3 Cellular structure of wood imaged in ESEM

Environmental SEM or ESEM overcomes the above difficulties through the introduction of two technologies: 1) differential pumping and 2) gaseous secondary electron detector (GSED). With differential pumping it is possible to maintain the electron gun at high vacuum while keeping the sample chamber at a constant pressure of 10-20 Torr. This is achieved, Fig.3.1, by a series of pressure limiting apertures placed in the column, across which pressure differentials are maintained. Thus, a relatively high pressure is maintained in the chamber while the vacuum in column is sufficiently low to operate LaB_6 filaments or field emission guns. Electron losses through scattering occur when the beam enters the specimen chamber. In general, electron losses increase at a rate that depends on chamber pressure, nature of chamber gas and accelerating voltage of beam. However, the scattered electrons, which are distributed over a broad skirt surrounding the focused spot, only contributes to background noise as its intensity is orders of magnitude lower.

The conventional Everhardt-Thornley secondary electron detector cannot be used in presence of gas or vapour because of electrical discharge (due to the high kilovolt bias used in this detector). The ESEM uses a GSED, Fig.3.2, which is biased only with a few hundred volts or less. Secondary electrons released from the specimen are driven by the field towards the anode. Amplification of the SE signal occurs by an avalanche of SE generation triggered by collisions with gas molecules in the path to the anode. Alternatively, the gaseous scintillation, which accompanies the electron avalanche, can be used as a signal. In this case, a photomultiplier is used to detect the light produced. On the other hand, the chamber gas ionized by SE and BSE are attracted to the sample surface and neutralize the negative charge accumulation. In this way, the principal advantage of ESEM, i.e. examination of insulating samples, is possible without the application of conductive coatings, Fig.3.3.

To summarize, the advantages of ESEM are: a) specimens (esp. electrically non- conducting) can be examined without complex and time consuming preparation methods and without modifying the natural surface or creating artifacts during sample preparation work; b) In-situ dynamical studies of gas/liquid/solid interactions can be carried out; c) Hydrated specimens can be examined (pressure > 609 Pa allows water to be in liquid phase at temperatures > 0 degrees Celsius); d) Biological specimens can be maintained fresh and live. Thus, ESEM constitutes a radical breakthrough from conventional scanning electron microscopy, where the requirement of high vacuum precludes the universal application of scanning electron beam imaging.

FIB

The focused ion beam (FIB) microscope has gained widespread use in fundamental materials studies and technological applications over the last several years because it offers both high-resolution imaging and flexible micromachining on a single platform. The micromachining is essentially done by sputtering or material removal in accordance to a pattern by an energetic ion beam controlled by an ion optic column. Most modern FIB instruments are "dual-beam" platforms with an additional SEM column and are capable of performing imaging, material removal, and deposition at length scales of a few nanometers to hundreds of microns.

The FIB instrument is similar to a SEM, Fig.4.1, except that an ion beam is scanned over the sample rather than an electron beam. The ion source used in all commercial systems and in majority of research systems reserved for micromachining applications is the Ga-based blunt needle liquid metal ion source (LMIS), which provides a bright and focused ion beam. During operation, Ga flows from a reservoir to the needle tip, from where it is extracted by field emission.

The ion beam column typically consists of (Fig.4.1): electrostatic condenser and objective lenses to define and focus the ion beam, beam-defining apertures, deflection plates for rastering the beam, stigmators and a beam blanker to deflect the beam onto a Faraday cup.

The sample is mounted on a grounded stage with three-axis translation-rotation-tilt capabilities and eucentric point located at the crossing of the ion and electron beams ('coincidence' point). The region of interest on the sample is moved to the eucentric point using translation and rotation and then tilted for the desired angle of beam incidence.

The various particles or radiation emitted due to interaction of the ion beam with the sample (X-ray, secondary and back scattered electrons) are sensed with detectors such as ET, BSED and EDS. The ions sputtered from the sample are detected by charge electron multipliers and secondary ion mass spectrometry.

The size and shape of the beam on the sample determines the image resolution and micromachining precision. Generally, the smaller the beam diameter, the better the FIB resolution and milling precision. Though the beam spot size is limited by chromatic aberration (due to beam energy spread) and spherical aberration (due to lenses), the ultimate spatial resolution is limited by sputtering and is thus sample-dependent. In current FIB-SEMs, the sputter-limited resolution is about 10 nm.

The FIB instruments have become a powerful tool for nanomachining by the augmentation with gas injection system (GIS) for enhancing the sputtering (etching) rate or site-specific chemical

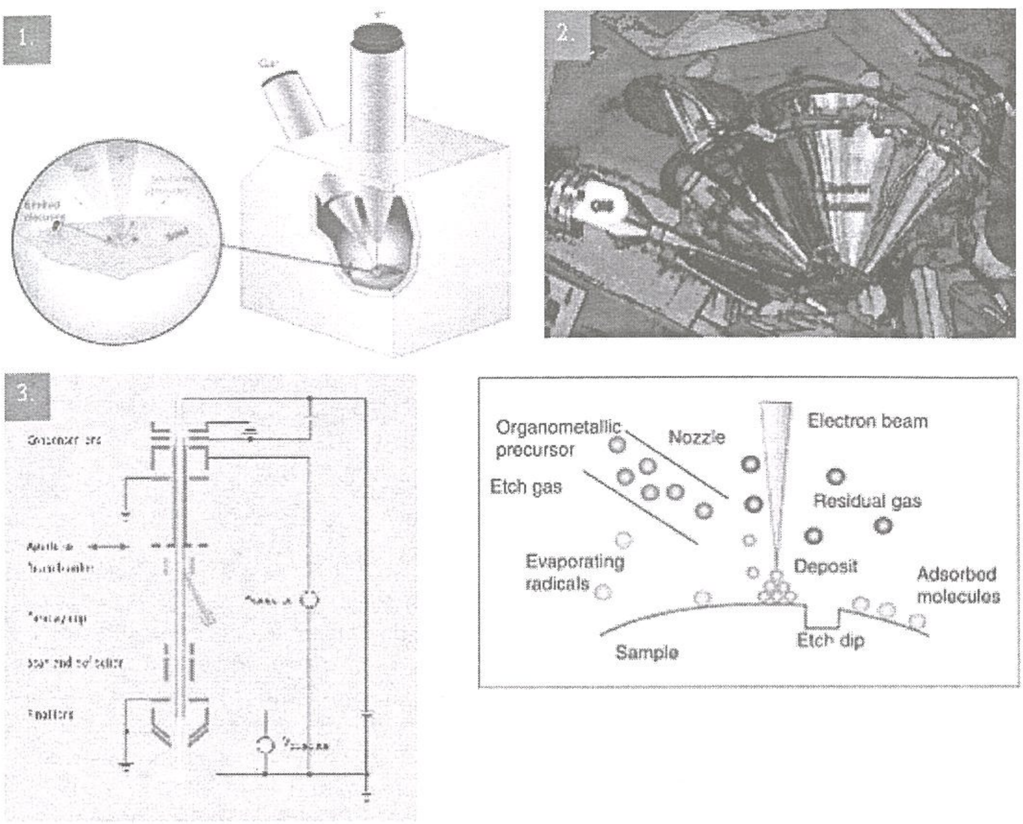

Fig. 4.1 (1) Dual beam FIB-SEM; (2) view of dual beam chamber; (3) ion column optics; (4) schematic showing GIS in deposition and etching.

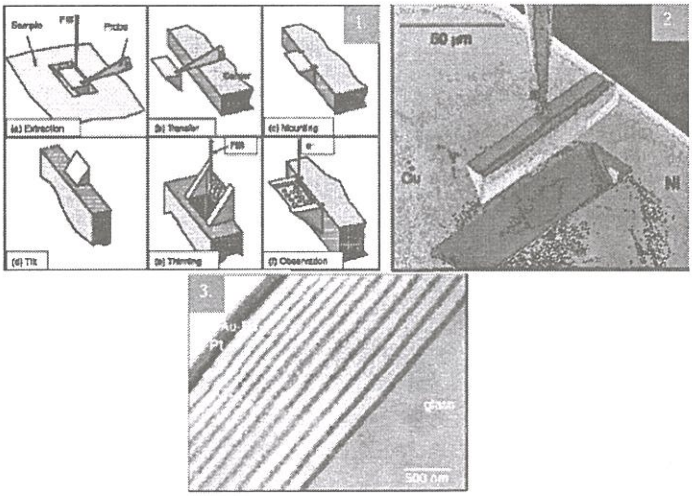

Fig. 4.2 (1) Process for preparation of TEM specimens by FIB; (2) lift-off of wedge specimen; (3) TEM specimen of coated fluorescent bulb prepared by FIB

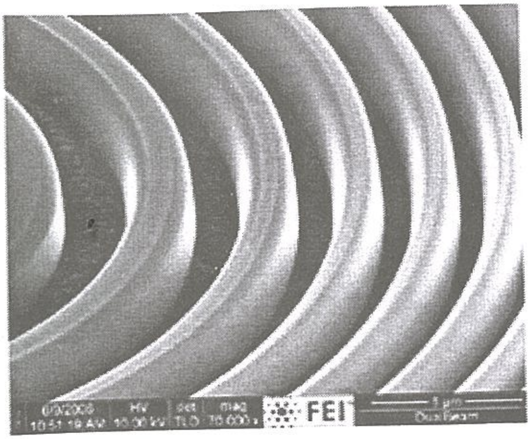

Fig. 4.3 Fresnel lens carved from Si substrate by reactive gas assisted FIB

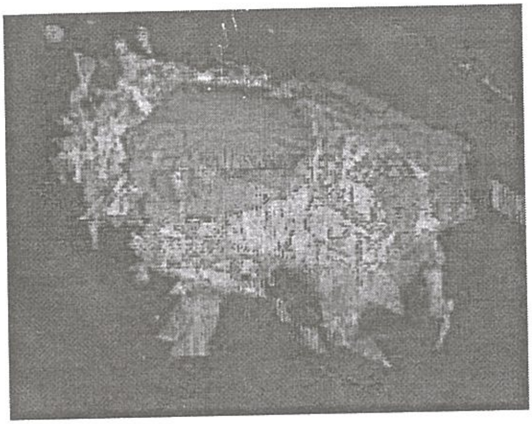

Fig. 4.4 3D reconstruction of the Laves-phase precipitation using the orientation maps derived from the 3D image stack.

vapor deposition (CVD). Secondary electrons generated by the incident ion beam (or the incident electron beam) crack the hydrocarbon precursor gases (introduced through gas injection needles) leading to local deposition of conducting material (W, Pt, or C) or insulating material (SiO_2). With additional micromanipulation accessories, it becomes possible to cut (sputter), paste (deposit), and watch (image) during a nanofabrication process within the FIB-SEM chamber. A few examples of nanofabrication for preparation of TEM specimens and prototype nanostructures are shown in Figs.4.2 and 4.3. Figure 4.4 shows an example of an interesting new technique known as 3D-EBSD, wherein 3D orientation information is build up slice by slice in a FIB-SEM equipped with an EBSD camera.

Acknowledgement

Much of the material presented in this paper, especially, figures and illustrations, have been taken from literature provided by FEI, Netherland (www.fei.com), Zeiss, Germany (www.Zeiss.com), JEOL, Japan (www.jeol.com), and the limitless amount of lecture notes and presentations available on the internet. The interested reader is directed towards these rich sources of information for a more detailed study of the multifunctional versatility of the SEM.

Monolayers and Thin Film Characterization using Atomic Force Microscopy

Dr. D.K. Aswal *joined Technical Physics and Prototype Engineering Division through 30th Batch of Training School. He has made several contributions in the field of thin/thick films and single crystals of various high temperature superconductors and colossal magnetoresistive materials. He has investigated various properties of magnesium-di-boride superconductor, metallic multilayer grown by molecular beam epitaxy and thermoelectric materials. Currently is is working on organic/molecular electronics. He is a recipient of several international fellowships including, JSPS, Japan (1997-99), IFCPAR, France (2004-05) and BMBF, Germany (2006). He is reviewer for 15 international journals. He has edited one book entitled "Science and Technology of Chemiresistive Gas Sensors" and authored more than 120 scientific publications.*

Dr. A.K. Chuahan *joined Technical Physics and Prototype Engineering Division through 36th Batch of Training School. He has developed software for "fully automated diameter controlled growth of crystals" in Czochralski system and grown crystals of various materials, such as,* $ZnWO_4$, BaF_2, *LiF etc. His current areas of research are self-assembled monolayers for molecular electronics applications and characterization of materials using Fourier transform infrared spectroscopy, ellipsometry, contact angle measurements and conducting atomic force microscopy.*

Dr. N.R. Joshi *obtained Ph.D. in 2007 from University of Mumbai, while working at Bhabha Atomic Research Center. He has worked on metallic multilayers using molecular beam epitaxy. Currently he is a post doctral fellow at Universitat Karlsruhe, Germany, and is working on the investigation of the interplay between magnetism and superconductivity in ferromagnet/superconductor heterostructures.*

Dr. J.V. Yakhmi*, Associate Director (S), Physics Group and Head, Technical Physics and Prototype Engineering Division of BARC, has worked for the past 40 years on diverse areas of research in materials science, such as, high Tc systems, magnetic alloys, molecular materials etc. He is reciepent of several nantional and international awards/fellowships, including Fellow, National Academy of Sciences, India; Maharashtra Academy of Sciences; Elected Member, Asia Pacific Academy of Materials; MRSI-ICSC Superconductivity and Materials Science Prize 1995 by Materials Res. Soc. of India; Distinguished Alumni Award from Kurukshetra University (India) 1996; IIS Gold Medal by Institute of Industrial Science, University of Tokyo, 1996; "UDCT Golden Jubilee Visiting Fellow", University of Bombay, 1997; Award of 'Excellence' by the CEFIPRA Scientific Council to the Indo-French Project 1308-4 "Chemistry and Physics of Molecular-based Materials" carried out during 1996-99. He has coedited a book entitled "Thallium-Based High Temperature Superconductors", and authored more than 300 scientific publications.*

Dr. D.K. Aswal, Dr. A.K. Chauhan, Dr. N.R. Joshi and Dr. J.V. Yakhmi, Technical Physics and Prototype Engineering Division, Bhabha Atomic Research Center, Mumbai 400 085; E-mail: dkaswal@yahoo.com

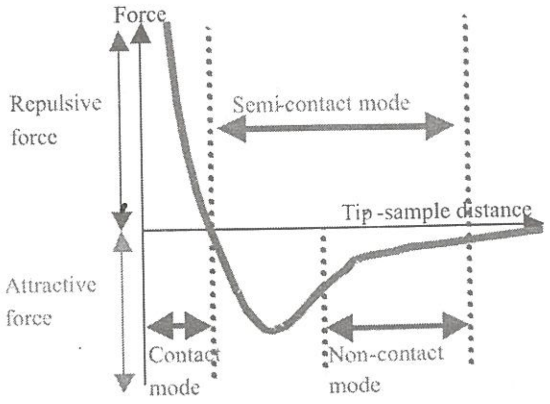

Fig. 1 *Van der Waals interaction between tip and substrate and different modes of AFM operation.*

Basics of Atomic Force Microscopy

The atomic force microscopy (AFM) belongs to a series of scanning probe microscopes (SPM). SPM technologies share the concept of an extremely sharp tip (3-10 nm radius of curvature) across the surface of an object. The tip is mounted on a flexible cantilever, allowing the tip to follow the surface profile. SPM series started with the invention of scanning tunnelling microscope (STM) in 1980's, which measures a weak electrical current flowing between tip and sample. With STM surfaces of conducting and semiconducting materials can be imaged upto subatomic resolutions. Scanning near-field optical microscopy (SNOM) scans a very small light source very close (less than the wavelength of light) to the sample. Detection of this light energy forms the image. NSOM can provide resolution of 30 nm, which is well below that of the conventional light microscope. In the AFM, the sample is scanned by a tip, which is mounted to a cantilever spring. While scanning, the force (as shown in Fig. 1) between the tip and the sample is measured by monitoring the deflection of the cantilever. A topographic image of the sample is obtained by plotting the deflection of the cantilever versus its position on the sample. Alternatively, it is possible to plot the height position of the translation stage. This height is controlled by a feedback loop, which maintains a constant force between tip and sample. Image contrast arises because the force between the tip and sample is a function of both tip–sample separation and the material properties of tip and sample. AFM may operate in several modes, which differ according to the force between the tip and surface. Some of these are listed in Table 1.

TABLE 1. Various modes of AFM operation

Mode of Operation	Force of Interaction
Contact mode:	Strong (repulsive) - constant force or constant distance
Non-contact mode:	Weak (attractive) - vibrating probe
Intermittent contact mode:	Strong (repulsive) - vibrating probe
Lateral force mode:	Frictional forces exert a torque on the scanning cantilever
Magnetic force:	The magnetic field of the surface is imaged
Thermal scanning:	The distribution of thermal conductivity is imaged
Electrical scanning:	The distribution of electrical conductivity is imaged

In contact mode, the tip is usually maintained at a constant force by moving the cantilever up and down as it scans. In non-contact or intermittent contact mode (tapping mode), the tip is driven up and down by an oscillator. In non-contact mode, the bottom-most point of each probe cycle is in the attractive region of the force-distance curve. In intermittent contact mode the bottom-most point is in the repulsive region. Variations in the measured oscillation amplitude and phase in relation to the driver frequency are indicators of the surface-probe interaction. To image frictional force, the probe is dragged along the surface, resulting in a torque on the cantilever. To image the magnetic field of the surface, a magnetically-susceptible probe is used. In other variations, the electric charge distribution on the surface or the surface capacitance is imaged. For thermal scanning microscopy (TSM) the thermal conductivity of the surface with is probed with a resistive tip that acts as a tiny resistance thermometer. In addition to these modes, many instruments are also designed to plot the phase difference between the measured modes, for example frictional force versus contact profile. This plot is called phase mode.

The analytic mode is chosen based on the surface characteristics of interest and on the hardness or stickiness of the sample. Contact mode is most useful for hard surfaces. However, a tip in contact with a surface is subject to contamination from removable material on the surface. Excessive force in contact mode can also damage the surface or erode the sharpness of the probe tip. Near-contact mode has less tendency to deform a soft surface, but is more sensitive to environmental vibrations and to variations in the film of moisture that coats samples in a normal atmosphere. Moisture or other thin liquid films expert an attractive capillary force on the probe as it is withdrawn from the surface. In non-contact mode this force becomes significant. Vibrating mode or intermittent contact modes are particularly suited for imaging soft biological specimen. However, biological samples are successfully imaged in the "harder" contact mode. Unfixed soft specimens are deformed in the z-dimension to a degree dependent on the imposed probe force, although spreading in the x-y plane may not be significant. Biological samples may be hardened to reduce probe-induced deformation by aldehyde fixation or frozen in a cryo-AFM.

The performance of a scanning probe instrument is limited by a number of factors. One of these is the resolution of the mechanical components used to move the tip and measure its position. The sharpness and stability of the probe tip determine the area of contact and the reproducibility of imaging. Obviously, environmental vibrations must be controlled to a high degree. In addition, most positioners depend on piezoelectric drive, which is subject to problems of non-linearity and to overshoot during rapid movements. The major manufacturers of SPM equipment have made substantial improvements in mechanical and electronic design. These improvements and advanced electronic calibration routines result in measurements that are more linear and accurate than the early models. Accurately nanofabricated gratings are the basis for two and three-dimensional calibrations. Such calibration gratings and calibration software are commercially available.

At very high magnifications and high-relief sample surfaces, the mode of imaging and the geometry of the probe tip can influence the scanned image. Knowledge of the probe geometry then becomes important for interpretation of the image. To image individual atoms and molecules it is necessary for the tip-surface interaction to depend only on the nearest atom(s) of the tip. This occurs in scanning tunneling microscopy because the tunneling current passes only through the nearest atom of the tip. Tunneling current falls off very steeply with distance from the surface. In atomic force microscopy the tip-surface interaction forces fall off less steeply with distance. Thus an AFM probe responds to the average force of interaction for a number of tip atoms, depending on the sharpness of the tip. An AFM image does not show individual atoms, but rather an averaged surface. For ordered surfaces this will reflect the average unit cell.

AFM has the ability to operate on a scale from microns down to nanometers and can image clusters of individual atoms and molecules. AFM has been used for measurements on a wide variety of samples including, inorganic (metallic films, ceramics, composites etc.), synthetic (data storage media, integrated circuits, self-assembled monolayers etc.) materials, nanostrcutures (Buckyballs and nanotubes), polymers and biological (Bacterial flagellae, DNA, chromosomes, cell and membrane) surfaces. Here we describe few examples of AFM characterization used in our own investigations. These include, growth kinetics of self-assembled organic mono and multilayers, annealing induced surface modification of MgO crystals, step formation on a $SrTiO_3$ single crystal and growth behavior of nano-crystalline nanocrystalline thin films of colossal magnetoresistance material $La_{0.6}Pb_{0.4}MnO_3$ and ultrathin Al films.

Growth Kinetics of Self-Assembled Organic Mono and Multilayers

Self Assembled Monolayer

The self-assembled mono- and multilayers deposited on Si are being proposed for hybrid nanoelectronics [1-4]. The surface coverage of a

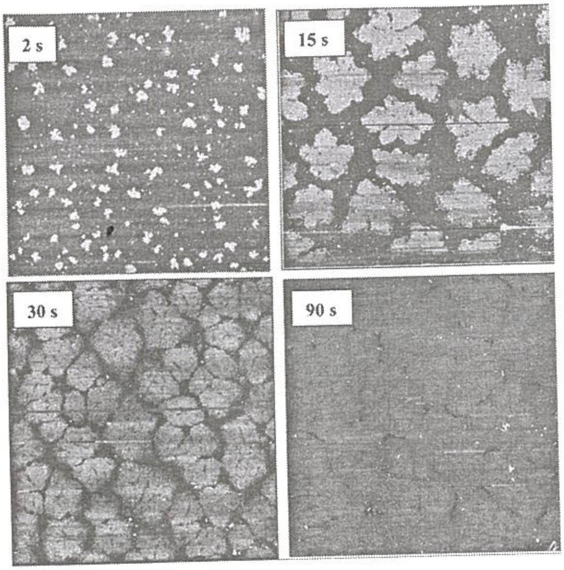

Fig. 2 *10 μm x 10 μm AFM images of partial C18 monolayer on Si immersed in octadecyltricholorosilane (OTS) solution for varying amounts of time.*

monolayer is usually examined by measuring the surface morphology using AFM. Here we present the growth kinetics studies carried on octadecyltrichlorosilane (C18 alkyl chain) monolayer deposited on Si. In Fig. 2, we show AFM images of partial C18 monolayers, which were deposited by immersing the Si substrate in the octadecyltricholorosilane solution for varying amounts of time. Initially isolated closed packed C18 islands are formed at the surface of the substrate, and these islands then serve as centers for aggregation for molecules diffusing on the surface as well as for adsorbing from solution (as schematically shown in the inset of Fig. 3). At low surface coverage the fractal dimension of the islands increases with surface coverage, while the height remains at ~25 Å indicating that C18 molecules are tilted at ~30°. At higher surface coverage, the islands height remaining at ~25 Å —grow by branching and eventually coalesce. With passage of time, the inter-island regions (pores or pinholes) shrink and eventually a continuous SAM get formed.

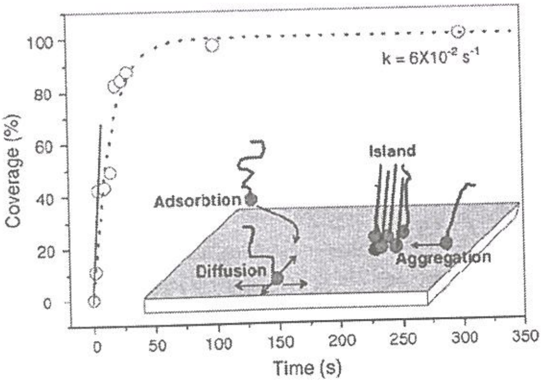

Fig. 3 *Monolayer coverage as a function of time determined using analysis of AFM images presented in Fig. 2. For time <5 s, a fast and linear growth (solid line fit) indicates that growth is due to diffusion limited aggregation. For higher time, the data is fitted (dotted line) to an equation governed by adsorption limited kinetics. Inset: Schematic showing the various processes during the monolayer growth. Once a molecule is adsorbed at the surface, it undergoes a random walk on the surface (with a certain value of 2D diffusion coefficient) until it collides with another adsorbed molecules and forms an island. Initially islands grow via diffusion-limited aggregation of adsorbed molecules followed by adsorption limited kinetics.*

In order to study the growth kinetics of the SAM formation, the monolayer coverage (Q) as a function of time, as shown in Fig. 3, is determined by analyzing the AFM images. The two regions showing different growth kinetics can be easily identified from this figure.

(i) A faster and linear growth for time <5 s (shown by solid straight line fit), indicating that the initial growth is primarily via diffusion limited aggregation

(ii) For higher times, the coverage kinetics becomes slow and can be fitted to an expression Q=1-exp (-kt), suggesting that growth is limited by adsorption from the solution.

Self Assembled Multilayers

We have been sucesseful in deposition of 3-aminopropyltrimethoxysilane [APTMS: $NH_2(CH_2)_3Si(OCH_3)_3$], multilayers of controlled thickness on SiOx/Si substrates using the layer-by-layer self-assembly process. We have demonstrated that these APTMS multilayers can be used as resistive molecular memory devices [5,6]. In general, the surface coverage and structure of the APTMS multilayers depends sensitively on various experimental parameters, such as, choice of solvent, water content of the solvent, silane concentration and reaction time. We have optimized these parameters to obtain the high-quality APTMS-multilayers. The self-assembly process of the deposited APTMS multilayers has been envisaged using the data obtained from the various characterization techniques, namely, static de-ionized water contact angle measurements, ellipsometry, X-ray photoelectron spectroscopy (XPS) and atomic force microscopy (AFM).

Typical AFM images of various APTMS samples are shown in Fig. 4. From the height profile of a partial-monolayer, formed after a grafting time of 20 min, it is apparent that the monolayer grows via the 2D nucleation and growth mode. The height of the island is ~7Å, which corresponds to the theoretical length of the APTMS molecule. This result is not in agreement with the reported literature, where the short alkyl-chains are found to grow by the layered growth mechanism. This difference could arise due to several factors, such as, different conditions of the substrate surface, different solution concentration, different head group of the silane molecule, and deposition under different ambient conditions. Clearly more research needs to be done to understand the grafting mechanism of the monolayer as a function of these parameters. The APTMS monolayer attains a surface roughness of <1Å, indicating that monolayer has a uniform coverage of the substrate. However, the surface roughness increases with increasing number of layers in the APTMS sample. In addition, the surface morphology also changes. For instance, the morphology of a 12-layered APTMS sample consists of islands having a lateral dimension of 100–200 nm with a height of ~7Å. A maximum surface roughness of ~7Å suggests that the APTMS multilayers grow by layer-by-layer self assembly.

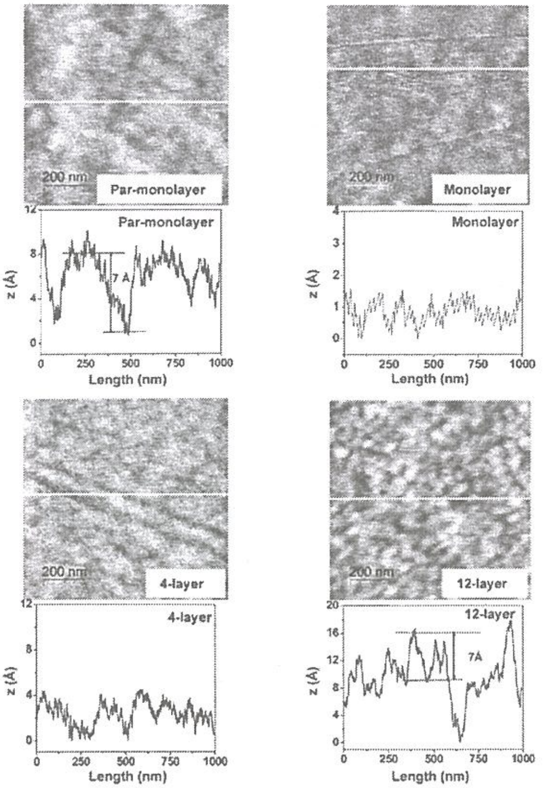

Fig. 4 1 μm x 1 μm AFM images recorded for different APTMS layers and the height profiles across the white line drawn in the respective AFM image.

Annealing Induced Surface Modification of MgO Crystals

MgO single crystals are being widely used as substrates for the growth of epitaxial thin films of various technologically important metal-oxide materials, such as, high temperature oxide superconductors (HTS), ferroelectric pervoskites, colossal magnetoresistive manganites etc. However, the surfaces of MgO crystals are very reactive to atmospheric moisture and carbon-di-oxide resulting in the formation of $Mg(OH)_2$ and $MgCO_3$, which destroy the properties of the growing films. We have demonstrated that by vacuum annealing one can not

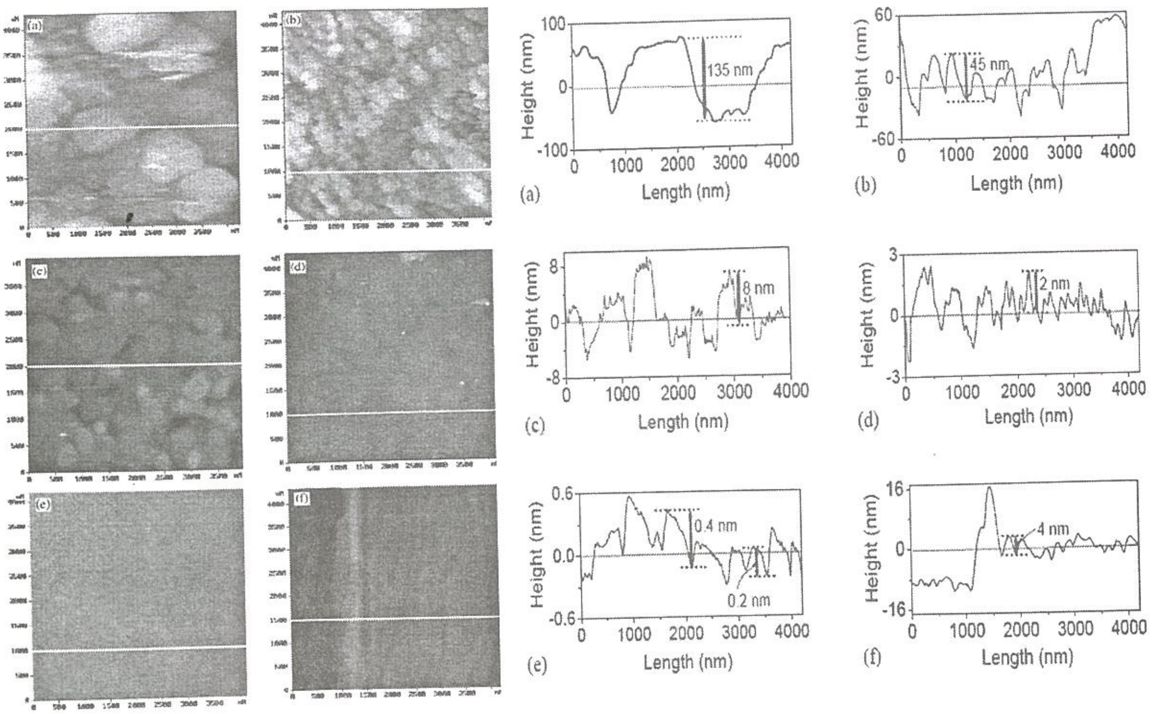

Fig. 5 Left: 4 μm x 4 μm AFM scan on [1 0 0]-oriented MgO surface annealed in air for 12 h at different temperatures; (a) as-received, (b) 700, (c) 900, (d) 1000, (e) 1100 and (f) 1250°C. Right: Height profiles across the white lines drawn in (a)–(f) of AFM images.

only remove $Mg(OH)_2$ and $MgCO_3$ but also obtains atomically flat MgO surface [7]. The AFM images depicting the morphological modifications as a function of annealing temperature are shown in Fig. 6. The surface roughness profiles, measured across the white lines, are also given in Fig. 5.

The as-received surface of the MgO crystals (obtained from the manufacturer) consists of large grains of diameter ~2000 nm. The surface roughness is found to be ~135 nm. X-ray photoelectron spectroscopy (XPS) measurements revealed that these grains consist of $Mg(OH)_2$ and $MgCO_3$, which were formed at the surface due to the reaction between MgO and atmospheric moisture and CO_2. The sample surface, after annealing at 700°C, shows a granular structure, with MgO grains having a size of ~300 nm. The surface roughness is found to be reduced to ~40 nm. The reduction in grain size is attributed to release of H_2O/CO_2 during the transformation of $Mg(OH)_2/MgCO_3$ into MgO, which was confirmed by XPS. Annealing at 900°C results in enlargement of MgO grains to ~800nm and reduction in surface roughness to 4 nm. These results suggest that at 900°C the grain growth take place. At high temperatures, the grain growth occurs because it reduces the surface energy of the grains. As the grains grow in size, their number decreases due to coalescence of surrounding grains of smaller size. In addition, the coalescence process reduces the surface roughness. This has indeed been confirmed when the annealing temperature is increased to 1000°C. At this annealing temperature, large grains with much reduced surface roughness (~2 nm) were observed. Annealing at 1100°C is found to yield very smooth surface with step-and-terrace structures. The terraces of ~700nm width and steps of 0.4 or 0.2nm height are found to develop. This is because at high temperatures, the enhanced surface diffusion would lead to faceting of the material. Since the base crystal has (1 0 0) plane, therefore, faceting of surface with [1 0 0] orientation is energetically favored. The

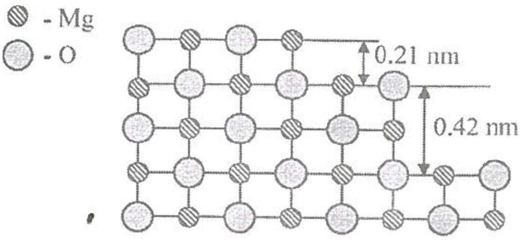

Fig. 6 Schematic showing the formation of a half-unit cell and one-unit cell steps at the [1 0 0]-oriented MgO surface.

surface steps, in between the (1 0 0) facetted regions i.e. terraces, are generated so as to lower the total surface energy. The step heights of 0.4 and 0.2 nm, formed in the present case, correspond to one-unit cell and half-unit cell dimension of the face-centered cubic structure of MgO, as shown schematically in Fig. 6. Increasing the annealing temperature to 1250°C resulted in rougher surfaces (surface roughness >4nm). The increased surface roughness at this temperature is attributed to the bunching of steps. At very high temperatures, the step movement becomes kinetically unstable. As a result steps aggregate together and form step bunches, sometimes of macroscopic size, separated by terraces of irregular widths.

Step Fabrication on $SrTiO_3$ Single Crystals

The steps of few hundred nanometers on the single crystals of $SrTiO_3$ are required for creating step junctions in the high-temperature superconducting films e.g. $YBa_2Cu_3O_{7-x}$ (YBCO). The YBCO film at the steps gets disordered and therefore show weak link behavior. This weak link characteristic can be used for making the superconducting quantum interference (SQUID) device. We have carried out some of the investigations on the step fabrication on the (100) single crystals of $SrTiO_3$ by ion milling. The ion milling was carried out by covering the half of the substrate using a SS mask. The AFM image of the ion milled substrate is shown in Fig. 7. It is seen that a clean step of 210 nm height spreading over 1675 nm is formed. The ion milling also does not create and significant damage.

Growth behavior of ultrathin Al films

Studies of ultrathin Al films (thickness <100 nm) are of technological importance for nanotechnology, such as, metallization in futuristic ultralarge-scale integration (ULSI) or gigascale integration (GSI) technology, as counterelectrodes in molecular electrodes etc.. At such a low film thickness, the mean free path of the electrons becomes larger than the film thickness, which results in a higher electrical resistivity of films compared to the bulk value owing to the scattering of electrons at the external surface. In addition, ultrathin Al films may not have a comprehensive coverage of the substrate and, therefore the growth morphology is expected to be discontinuous and would govern the film resistivity by scattering of electrons at the grain-boundaries. We have shown that at ultra-low

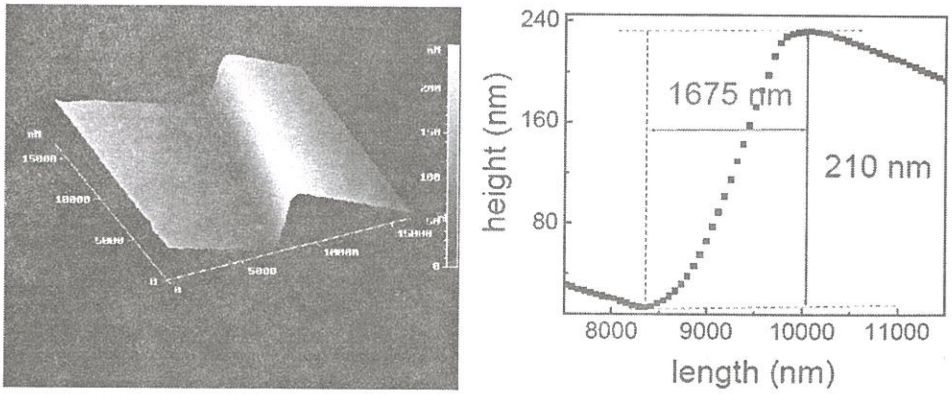

Fig. 7 The AFM image and height profile of a step created on the (100) single crystal of $SrTiO_3$ by ion milling.

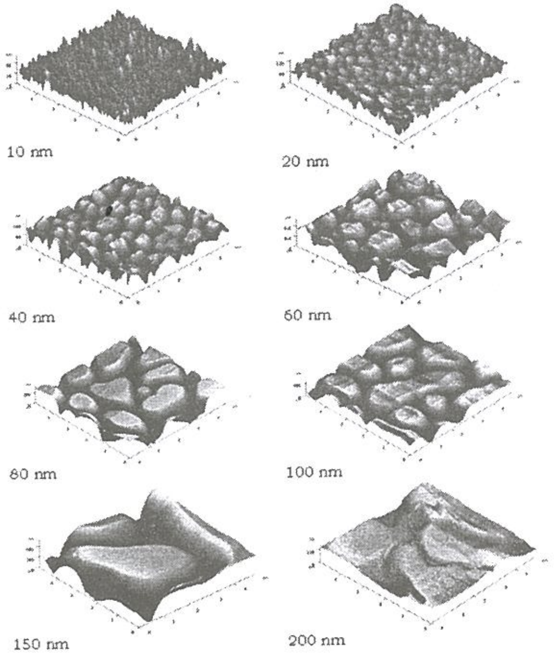

10 nm
20 nm
40 nm
60 nm
80 nm
100 nm
150 nm
200 nm

Fig. 8 AFM images of Al films with varying thickness deposited at 500°C.

thickness (<60 nm) the growth morphology of Al films on Si substrates consists of a two-dimensional random network of Al islands, which in turn lead to an anomalous thickness as well as temperature dependence of the electrical resistivity. The low temperature metal-to-insulator transition observed in these films has been explained using variable range hopping conduction mechanism [8,9].

Thin films of Al of varying thickness at different temperatures were grown on Si (111) using MBE (RIBER EVA 32 E) system. The preparation/cleaning process adopted for Si (111) substrates (Wacker-Chemitronic GmBH, Germany) is as follows. First, Si (111) wafer was degreased by trichloroethylene and cleaned ultrasonically using acetone. The cleaned substrates were etched in dilute HF acid (4%) and rinsed in de-ionized water and finally in acetone. The AFM images depicting the morphology of Al thin films of varying thickness deposited at a fixed substrate temperature of 500°C are shown in Fig. 8. Qualitatively, from these images it is evident that Al films grow via island or Volmer-Weber growth mechanism on Si substrates. At low thickness the grains have spike-like features with small average grain size. As the thickness increases, the morphology takes columnar shape. A coalescence of the grains takes place at a particular thickness, which depends on the deposition temperature viz 60 nm for a deposition temperature of 250°C and 150 nm for 500°C.

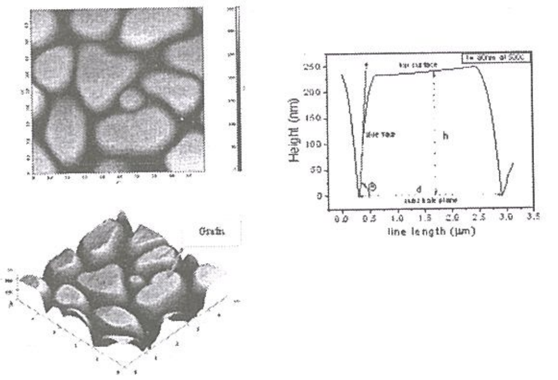

Fig. 9 A typical example demonstrating quantification of an AFM image. The line-height profile across a grain yields various parameters (as discussed in the text).

The advantage of AFM technique is that one can quantify various parameters of the grains. These include the average grain size (d), average grain height (h), the angle (Φ) between the side face of the grain and the substrate plane, and roughness or step patterns on the surface of the grains. The determination of these parameters is demonstrated in Fig. 9. First, one records a height profile across a line in a 2D AFM image, and then from this profile h, d and Φ can be determined. Φ is determined by measuring the slope of the line corresponding to the side face. Such measurements are done over a large number of grains to obtain the average values. From these parameters one can infer the mec hanism of grain growth in a film.

Fig. 10. Variation of average grain size of Al with thickness at deposition temperatures of 250°C and 500°C.

The dependence of average grain size (d) on thickness (t) for film grown at 250 and 500°C is plotted in Fig. 10. For a substrate temperature of 250°C, d increases monotonically up to a thickness of 100 nm and above that the films become continuous across the substrates. The values of d are usually 20-25 times larger than t. Almost similar trend is observed for of the substrate temperature of 500°C, except that the grains are slightly larger in size. This is expected as at a high substrate temperature, the grain boundary migration becomes faster. Interestingly however, a complete coalescence is observed at a much higher thickness i.e. ~150 nm. This phenomenon is quite unusual as at high temperatures the coalescence is anticipated to be at lower thickness, owing to a higher surface diffusion of the atoms.

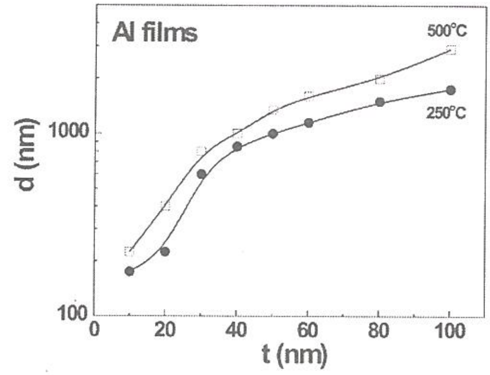

Fig. 10 Variation of average grain size of Al with thickness at deposition temperatures of 250°C and 500°C.

Nanocrystalline La$_{0.6}$Pb0.4MnO$_3$ Thin Films

The nanocrystalline thin films of colossal magnetoresistance material La$_{0.6}$Pb$_{0.4}$MnO$_3$ were grown using pulsed-laser ablation technique at 550°C [10]. A typical 1400 nm X 1400 nm AFM scan of LPMO films is shown in Fig. 9. The film consists of very fine grains, which is seen more clearly from a smaller AFM scan of 250nmX250 nm. The height profile, recorded across a white line drawn in revealed (i) that the average surface roughness of the film is <0.7nm indicating very smooth surface of the films and (ii) an uniform distribution of grains with an average size of ~17 nm. The magnetization data show that grain boundaries act as tunnel barriers, which leads to an enhanced magnetoresistance of >100% at 1 T [10].

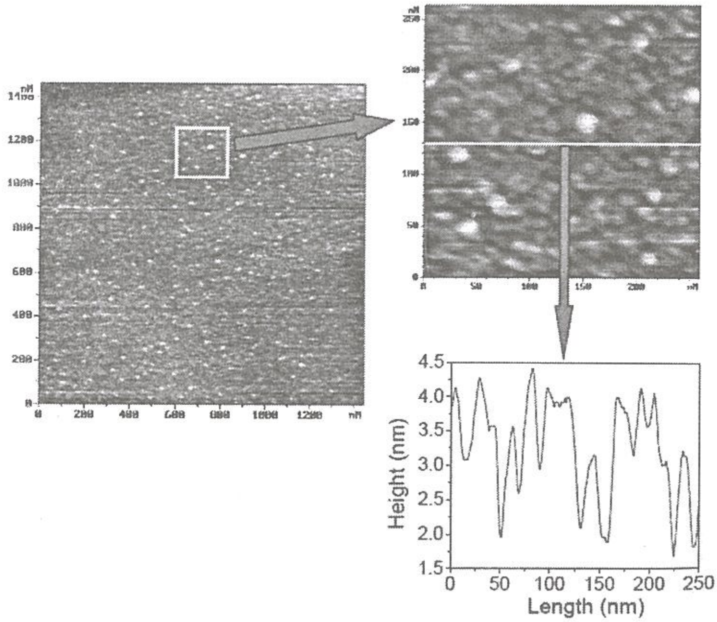

Fig. 11 1400 nm x 1400 nm AFM scan of a nanocrystalline LPMO film, 250 nm x 250 nm AFM scan corresponding to the white square drawn, and the height profile across the white line.

Fig. 11 1400 nm x 1400 nm AFM scan of a nanocrystalline LPMO film, 250 nm x 250 nm AFM scan corresponding to the white square drawn, and the height profile across the white line.

Summary

In summary, we have demonstrated the AFM technique is a powerful tool in the surface imaging of organic and inorganic thin films in the length scale ranging from nanometer to micrometer. AFM allows getting information not only in the X-Y plane, but also in the Z-direction. Thus, one can easily investigate growth kinetics of the films and surface modifications of the samples.

Acknowledgement

We would like to thank our colleagues S.K. Gupta, A.K. Debnath and Ajay Singh from BARC, and S. Lenfant and D. Vuillaume from IEMN, Lille, France for their support in various experiments.

References

1. Self assembled monolayers on silicon for molecular electronics, D.K. Aswal, S. Lenfant, D. Guerin, J.V. Yakhmi and D. Vuillaume, Analytica Chimica Acta, 568 (2006) 84–108
2. Molecule/Silicon hybrid nanoelectronics (Invited Review), D.K. Aswal and J.V. Yakhmi, IANCAS Bulletin 6 (2007) 161.
3. Electrical bistability in electrografted 5-(4-undecenyloxyphenyl)10,15,20-triphenylporphyrin monolayer on Si, S.P. Koiry, D.K. Aswal, A.K. Chauhan, V. Saxena, S.K. Nayak, S.K. Gupta and J.V. Yakhmi, Chem. Phys. Lett. 453 (2008) 68–72.
4. Electrochemical grafting of octyltrichlorosilane monolayer on Si, S.P. Koiry, D.K. Aswal, Vibha Saxena, N. Joshi, S.K. Gupta J.V. Yakhmi and D. Vuillaume, Appl. Phys. Lett. 90 (2007) 113118.
5. Resistive memory effect in self-assembled 3-aminopropyltrimethoxysilane molecular multilayers, A. K. Chauhan, D.K. Aswal, S.P. Koiry, S. K. Gupta and J.V. Yakhmi, Phys. Stat. Sol. (a) 205(2008) 373.
6. Self-assembly of the 3-aminopropyltrimethoxysilane multilayers on Si and hysteretic current-voltage characteristics, A.K. Chauhan, D.K. Aswal, S.P. Koiry, S.K. Gupta and J.V. Yakhmi, C. Suergers, D. Guerin, S. Lenfant and D. Vuillaume, Appl. Phys. A 90 (2008) 581
7. XPS and AFM investigations of annealing induced surface modifications of MgO single-crystals, D.K. Aswal, K.P. Muthe, Shilpa Tawde, Sipra Chodhury, N. Bagkar, Ajay Singh, S.K. Gupta and J.V. Yakhmi, J Crystal Growth 236 (2002) 661
8. Thickness dependent morphology and resistivity of ultra-thin Al films grown on Si(111) by molecular beam epitaxy, D. K. Aswal, N. Joshi, A. K. Debnath, S. K. Gupta, D. Vuillaume, and J. V. Yakhmi, Phys. Stat. Sol. 203 (2006) 1254
9. Morphology dependent electric transport in textured ultra-thin Al films grown on Si. D.K. Aswal, Niraj Joshi, A.K. Debnath, K.P. Muthe, S.K. Gupta, J.V. Yakhmi and D. Vuillaume, J. Appl. Phys. 98 (2005) 026103
10. Enhanced magnetoresistance in nanocrystalline$La_{06}Pb_{04}MnO_3$ thin films, Ajay Singh, D.K. Aswal, C.S. Viswanadham, G.L. Goswami, L.C. Gupta, S.K. Gupta and J.V. Yakhmi, J Crystal Growth 244 (2002) 313

Study of Materials Using Positron Annihilation Spectroscopy

*Dr. **P.K. Pujari** did M. Sc in Chemistry from IIT Delhi in 1984. He is Homi Bhabha Award winner from the 28th batch of training school. After one year of training, he joined Radiochemistry Division of BARC in 1985. He specialises in positron annihilation spectroscopy and its applications.*

*Mr. **Kathi Sudarshan** is gold medalist from University of Hyderabad in MSc chemistry in 1998. He joined radiochemistry division of BARC in 1999 from the 42nd batch of training school. His research areas include positron annihilation spectroscopy, radio analytical techniques and heavy ion induced reactions. He has published about 30 papers in peer-reviewed journals*

One of the significant predictions made by Dirac [1] in 1930, while dealing with the negative energy solutions that appeared in describing the relativistic behavior of electrons, is the existence of positron, the anti-particle of the electron. The positron was later discovered by Anderson [2] in cloud chamber photographs of cosmic-ray showers. Most of the physical properties of positron are same as electron except the sign of its charge and attendant properties.

Positron is an anti-particle of electron and they annihilate to produce photons, the event being governed by quantum electrodynamics. In principle, any number of photons can be produced in an annihilation event within the constraints of conservation laws. Zero-photon annihilation requires two 'third' bodies for conservation of momentum and is unlikely due to the requirement of unfavorable momentum transfer. One-photon annihilation requires a third body where as two-photon annihilation requires none. All the conservation laws are satisfied by the two photons themselves. As a consequence, the two photon annihilation is by far the most common mode. When the electron and positron meet with their spins parallel, that is triplet interaction, three annihilation quantas are emitted. The relative number of two and three photon annihilations depends on the triplet and singlet interactions and the rate of annihilation from each state. The statistical ratio of singlet (m=0) to triplet (m=0,±1) state is 1:3 and the ratio of their annihilation rates is 1115:1. Hence the ratio of probabilities of two photon to three photon annihilation resulting from free positron is 1115:3 or 372:1. The rate of annihilation of positron is a function of electron density although the effects of coulombic attraction of electron and positron, the Pauli's exclusion principle and other field and space effects must be taken into account to calculate the annihilation rate.

The experimentally observed ratio of three-photon to two-photon annihilation rate often differs from the theoretically expected ratio of 1/372 for a free positron [3]. Thus, free positron annihilation is not the only mechanism of disappearance of positrons. The formation of positronium changes this ratio. The possible existence of a bound state between positron and electron was realized soon after the discovery of the positron. The name 'positronium' was suggested for this unstable atom composed of positron and negative electron. Experimental evidence for the

Dr. P.K. Pujari and Shri K. Sudarshan, Radiochemistry Division, Bhabha Atomic Research Centre, Mumbai 400 085;
E-mail: pujari@barg.gov.in

existence of positronium atom was first found [4] while studying the slowing down of positrons in different gases. The positronium atom (Ps) can be described in the same theoretical framework as that of hydrogen atom, the only difference being the mass of the positive charged particle. Hence the reduced mass of positronium is half that of the hydrogen atom. It follows that there is one-to-one correspondence between the state of positronium and hydrogen, but the energy levels of the positronium are half as deep as the corresponding states of hydrogen.

Like hydrogen molecule, positronium can also exist in two states i.e. the triplet, called ortho-Positronium (o-Ps) with parallel orientation of the spins of positron and electron and singlet, called para-Positronium (p-Ps) with anti-parallel spins. The selection rules and cross section for self annihilation of positronium are similar to that of a free positron. The relationship between the orbital angular momentum l of the positronium state, the spin quantum number s and the number of photon emitted in self-annihilation, n, is given as

$$(-1)^{l+s} = (-1)^{n}$$

According to this selection rule, singlet states annihilate into an even number of photons and triplet states into odd-number of photons. Therefore, the ground state p-Ps and o-Ps annihilate into two and three photons respectively. The intrinsic lifetimes of the p-Ps and o-Ps are 125 ps and 142 ns respectively.

The fate of the positron and positronium is influenced by properties of the medium they are in. Hence, positron annihilation spectroscopy (PAS), the branch of science dealing with the study of materials using positron/Ps as probe and monitoring the annihilation gamma rays, allows one to extract nanoscale information specific to the site of annihilation. Due to the ability of positron to form a variety of electronic states in molecular media, it yields unique information about the properties of the material under study. The positron and positronium are preferentially trapped in low electron density areas like defects/free volumes owing to the repulsion between positron and positively charged nuclei of atoms. Positron trapping at mono vacancies, dislocations and vacancy clusters in metals has been extensively studied by PAS [5,6]. The PAS has found its way in the study of the type of vacancies and electronic environment around the vacancies in semiconductor materials [7,8], the free volume hole size distributions and micro structural changes in polymers [9,10], materials of technological importance like catalysts [11], low-k dielectric materials [12], and nano materials [13].

In this article, the principle of the different positron annihilation spectroscopic techniques used in material science studies and few applications with special reference to polymers, high Tc super conductors, porous materials and nano-particles will be discussed.

Experimental Techniques

The rate of annihilation or the survival time of positron in a matrix is a function of electron density. The energy and angular distribution of annihilation photons are important considerations in positron annihilation. In case of two photon annihilation, momentum and energy conservation law requires that the photons leave the annihilation site traveling in almost exactly opposite directions and that the energy of each photon is almost exactly one-half the total energy of the system. However, the deviations from the collinearity and energy are caused due to finite momentum associated with the annihilating pair. Since, the thermalisation time of the positron is very short, the contribution to the momentum of the annihilating pair is principally from the participating electron in the annihilation. Hence, the survival time of the positron in the medium and the energy and angular distribution of annihilation gamma-rays carry valuable information about the matrix in which the positron is injected. Positron Annihilation Lifetime Spectroscopy (PALS), Doppler Broadening of Annihilation Radiation (DBAR) and Angular Correlation of Annihilation Radiation (ACAR) are three traditional experimental techniques in Positron Annihilation Spectroscopy (PAS) developed to monitor these features. A schematic of these techniques is shown in Fig.1 taking the example of positron from ^{22}Na source. The correlated measurement technique, namely, positron Age and MOmentum Correlation (AMOC) is used to get the time resolved information on the positronium states. The less commonly used techniques in PAS include measurement of $3\gamma/2\gamma$

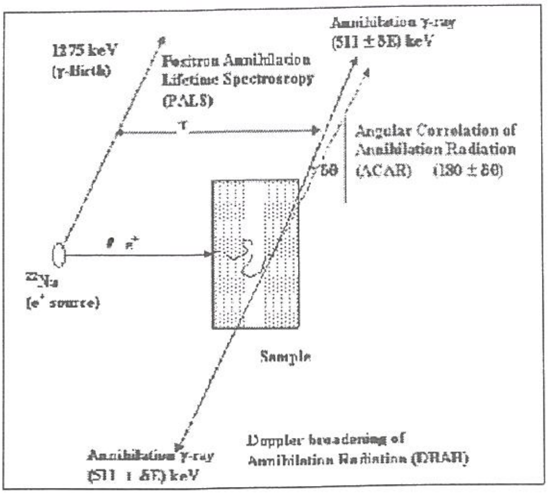

Fig. 1 Schematic of the principle of important techniques in PAS

fraction. The basic quantities that are measured in various experimental techniques in PAS and the principal information obtained from them are given in Table 1.

The neutron deficient radioisotopes are the most commonly used source of positrons in PAS. The choice of a particular isotope depends on the experimental techniques used. The lifetime technique requires the isotopes with good prompt gamma-ray yield accompanying the positron emission to mark its birth. ^{22}Na is the most suitable radioisotope for the positron lifetime studies, though it is also routinely used in all the positron annihilation techniques. The conventional isotopic sources, give the positrons with large distribution of energies (0 to β_{max}). Hence, depth dependent information on materials can not be obtained using these sources. The mono energetic positron beams

TABLE 1. Summary of the experimental techniques in positron annihilation spectroscopy

Technique	Quantities monitored	Principal information derived
Positron Annihilation Lifetime Spectroscopy (PALS)	Time difference between the birth of positron (signaled by prompt gamma ray) and annihilation gamma ray	Lifetimes of the positron corresponding to different positron or Ps states. Depends on the electron density and positron / positronium chemistry of the matrix
Doppler Broadening of Annihilation Radiation (DBAR)	Energy spectrum of annihilation gamma ray to monitor its deviation from 511 keV	Deviation of the annihilation gamma-ray energy from 511 keV gives the longitudinal component of the annihilating pair momentum $E_\gamma = E_0 \pm \delta E = m_0c^2 \pm c\frac{P_L}{2}$
Angular Correlation of Annihilation Radiation (ACAR)	Angular deviation of the two annihilation gamma rays from 180^0.	Angular deviation gives the transverse component of the momentum of the annihilating pair $\delta\theta \approx \frac{P_T}{m_0c}$
Age-MOmentum Correlation (AMOC)	Both PALS and DBAR in correlated mode	Longitudinal component of the momentum corresponding to the positron age or states
3γ/2γ-ratio	Energy spectrum of the annihilation gamma ray	Positronium yields and re-emission probabilities from the surfaces
2-detector Coincidence Doppler Broadening (CDB) measurement	Energy spectra of both the annihilation γ-rays in coincidence	Momentum distribution (as in DBAR) with high signal to background ratio in the higher momentum region there by enabling the identification of chemical identity of electronic environment around the site of annihilation by indexing core electron momentum

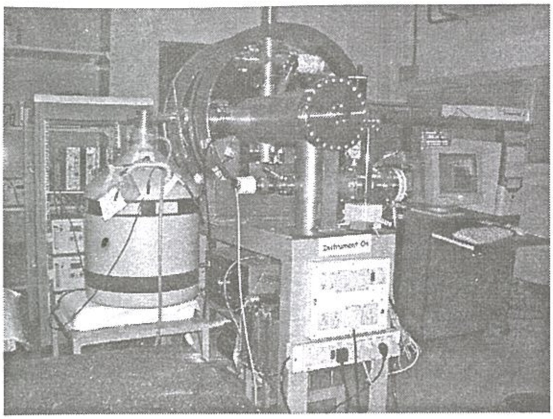

Fig. 2 The Slow Positron Beam Facility At Radio Chemistry Division (SPARC)

enable depth dependent studies in thin films. The mono energetic positron beams are obtained by moderating the positrons produced by radioisotopes or pair production of the gamma-rays, followed by extracting with einzel lens, transportation and accelerating by floating the target. A typical photograph of the slow positron beam facility at Radiochemistry Division is given in Fig.2. Alternately, the source/moderater can be floated at required voltage and the accelerated positrons can be transported to the target chamber.

Applications

The ACAR has been used to measure the momentum distribution of electrons in metals and alloys. The ACAR curves have been fitted to components comprising of a central inverted parabola corresponding to positron annihilations with valence electrons and one or more Gaussians corresponding the annihilations with core electrons. The energy corresponding to the point where the inverted parabola cuts the momentum axis gives the Fermi energy of the metal. The 2D-ACAR curves give the Fermi surface. The ACAR curves have been extensively used to measure the Fermi surfaces in various metals [5]. These measurements are supported by extensive theoretical calculations on electronic structure.

The positrons tend to localize in defects due to lesser nuclear repulsion compared to bulk. This makes PAS a valuable tool in defect spectroscopy of metals, alloys and semiconductors. The positrons trapped in the defects experience lower electron density than the positrons in bulk resulting in the lower annihilation rate or increased lifetime of the positron. The trapping of the positrons also results in the narrowing of the DBAR spectrum. The Doppler broadened spectrum is analyzed in terms of its shape parameters 'S' and wing parameter 'W'. The parameters S and W are defined as the fractional area in the central (low momentum region) and wing regions (higher momentum region) of the annihilation peak respectively. The changes in the positron lifetime and shape parameter in the annihilation spectra have been utilized to study the point defects, di vacancies, vacancy clusters, dislocations etc. in metal and alloys and semiconductors [6]. The changes in the slopes of S-W correlation curves have been utilized to understand the changes in the types of defects. A typical S-W correlation plot with elapsed time after deformation in Fe-Si alloys is shown in Fig. 3 [14]. The pure Fe alloy shows higher W parameter. Among the two Fe-Si alloys, the decay rate of S-parameter increases with Si content. With the advent of newer techniques like CDB, which offer high signal to background ratio in the higher momentum region of the annihilation spectra, it has been possible to establish the electronic environment around the site of positron annihilation or the defects [15] by monitoring their core electron momentum. A

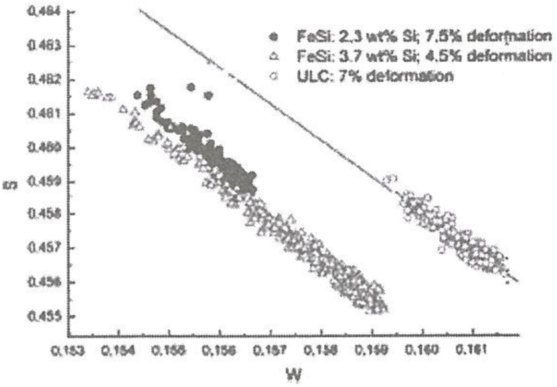

Fig. 3 S-W correlation evolution curve in Fe-Si alloys and ultra low carbon steel (ULC). Time after the deformation is increasing from left to right along the direction of the line

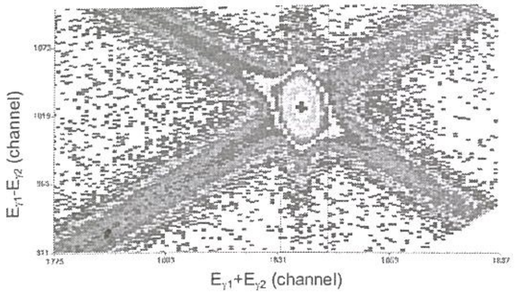

Fig. 4a The sum and difference spectra of the annihilation gamma-ray energy signals measured in CDB. The difference is plotted by shifting the origin to 1024 channels. The y-projection with sum being 1022 keV (shown as box) gives the CDB spectrum

typical CDB spectrum is shown in Fig. 4 (a). The ratio of the momentum curves from the annihilation spectra is taken with respect to a reference to identify the chemical surroundings of the positron annihilation site. The ratio curves of ethylene vinyl acetate copolymer and n-irradiated silica with respect to polyethylene are shown in Fig. 4(b). The ratio curves indicate the similarity in the core electron momentum of the elements around the site of annihilation, showing the positron trapping near the polar oxygen groups in polymers and near oxygen centers in silica [16].

PAS has also been used to study the phase transitions as they invariably involve changes in the electronic structure. A variety of phase transitions like glass transitions, magnetic transitions etc have been studied using PAS. The notable transition which received much attention is the transition to the superconducting phase. The temperature dependence of positron lifetime across the superconducting transition temperature in MgB_2 is shown in Fig. 5. In high temperature superconductors like YBCO, PAS has revealed electronic-structural changes at the onset of superconductivity and the possible presence of oxygen dimers and electron density change in copper-oxygen planes. In BSCO, evidence for local charge-transfer process from CuO_2 to Bi-O planes at the onset of the superconductivity [17], influence of sample preparation conditions and structural changes on the temperature dependencies of the positron annihilation parameters have been shown [18]. Recent studies on MgB_2 superconductors have revealed that the boron layer is electronically active at the onset of superconductivity and the nature of superconducting transition has a striking resemblance to HTSCs[19].

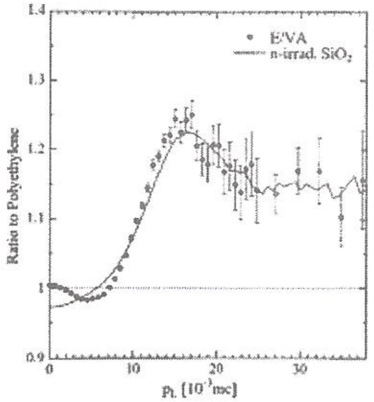

Fig. 4b The ratio curve of ethylene vinylacetate copolymer (E/VA) blend and neutron irradiated SiO_2 with reference to polyethylene, showing the trapping of positrons near the polar groups (oxygen) in polymer and SiO_2 [16].

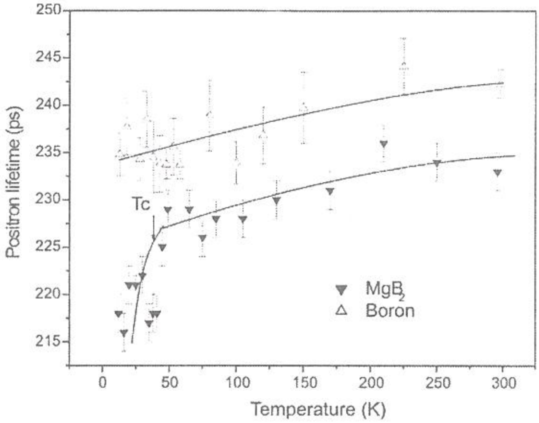

Fig. 5 Temperature dependence of the positron lifetime in MgB_2 and pure boron. The arrow indicates the T_c (39.4 K) in MgB_2. The solid lines are eye guides [19].

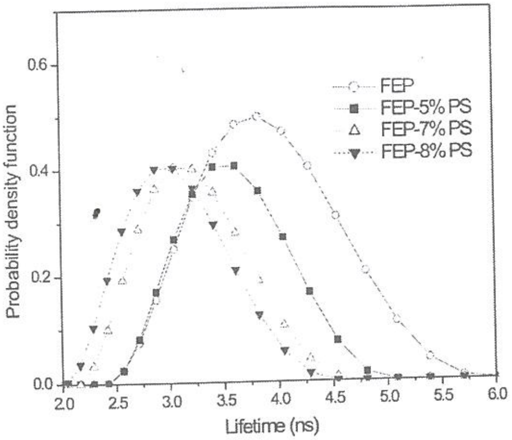

Fig. 6 Positronium lifetime distribution FEP-g-P-Styrene

The intrinsic lifetime of o-Ps is reduced from 142 ns in a medium by a process called pick-off annihilation. The pick-off annihilation rate depends on the free volume hole radius/pore size in polymers and porous materials. Hence, the positron annihilation lifetime technique has been the most successful technique for studying the free volume holes in polymers. The o-Ps being small in size (1.02 Å) can probe very small holes. Unlike the scanning electron microscopy and tunneling electron microscopy, which can probe static free volume holes, PAS can probe dynamic free volume holes caused by the molecular motion in polymer chain owing to shorter lifetime of positronium probe. The pick-off annihilation rate (λ) of the o-Ps is related to the free volume hole size (R) from which Ps is annihilating as

$$\lambda(ns^{-1}) = 2*\left[1-\frac{R}{R+\Delta R}+\frac{1}{2\pi}\sin\left(\frac{2\pi R}{R+\Delta R}\right)\right]$$

where ΔR is the electron layer thickness parameter and is taken as 1.66 Å. The product of the free volume hole size and the o-Ps intensity indicates the free volume hole fraction in the polymers. The PAS has found its maximum applications in the study of polymers as many properties of the polymers are directly influenced by the free volumes. Besides, average free volume size, the free volume hole size distributions can also be derived from lifetime spectroscopy. The free volume hole size distributions are essential to understand the microstructure of polymers which can be correlated with macroscopic properties. The changes in the o-Ps lifetime distributions (free volume hole size distributions) in fluorinated ethylene propylene copolymer with grafting of polystyrene are shown in Fig. 6. As can be seen from the figure, the grating of polystyrene on the copolymer reduces the free volume hole size distributions. The free volume hole size distributions have been found to be well correlated with gas separation factors in the membranes [20]. The changes in the free volumes distributions with temperature have also been studied to understand the molecular chain motions in the polymers.

The positron is an in situ probe in porous materials. The o-Ps lifetime is directly related to the pore size. The intensity of the o-Ps is directly proportional to the surface area. The Ps being small and in situ probe, can probes the pore in the dimension range of < 5 Å, where the techniques like BET fail due to the dimension of the adsorbates used. The Ps can also probe the hidden pores. The adsorbates on the porous surfaces have also been probed by utilizing the reactivity of the adsorbates with Ps species. The various ways in which the PAS is useful in studying the porous materials is schematically shown in Fig. 7. The PAS has found many applications in study of zeolites, catalysts etc [11]. One of the most notable of the application of PAS in porous materials is the study of low-k dielectrics. With the advent of intense and pulsed slow positron beams, the depth profiling of porous thin films has been possible. The positrons beams have utilized to understand the complete pore architecture in the films. The surface properties, the closed porosity, open porosity and pore inter connectivity have been examined in the porous films [12].

The inherent sensitivity of the positron to embedded precipitates as well as surface defects in nanoparticles has made this technique a powerful tool in the study of nanoparticles. The diffusion length of positron in most materials is the range of nm and this makes the implanted positrons annihilate on the surface of the nanospheres. Hence PAS has been found to be a sensitive technique to the changes in the electronic structure with the size in

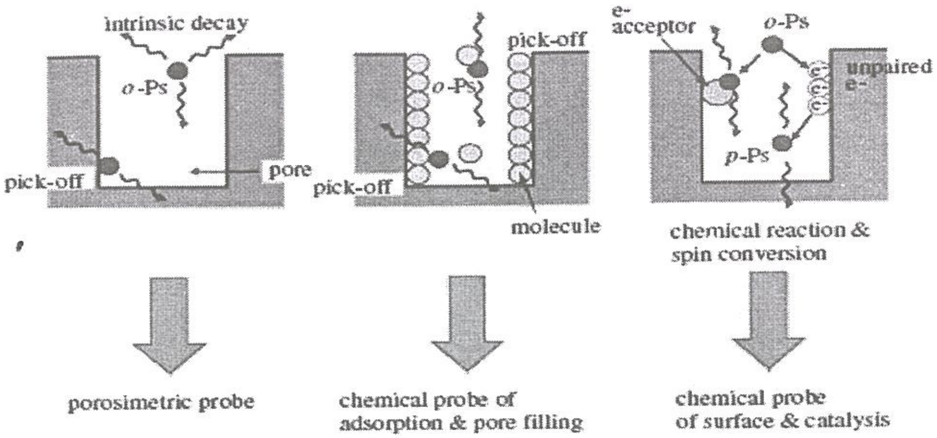

Fig. 7 Schematic representation of probing the porous materials using positrons [21]

nanostructured materials [22]. The PAS has shown considerable promise as site selective probe in studying the nanocrystalline embedded particles. In these embedded systems, the other probes employed interact with nanocrystallites and host matrix there by making it difficult to extract the weak interactions with nanoparticles from a large background from the host matrix. The nanoparticles dispersed in the matrix like MgO have been studied by PAS to understand the defect dynamics in these materials [23,24]. The inherent preference of positron to probe Au nanoparticles embedded in MgO matrix is illustrated in Fig. 8 in the form of momentum distribution ratio curves from CDB studies. Ultra low level sensitivity of the positron to the precipitates has been utilized to understand the nanoprecipitates in alloys [25].

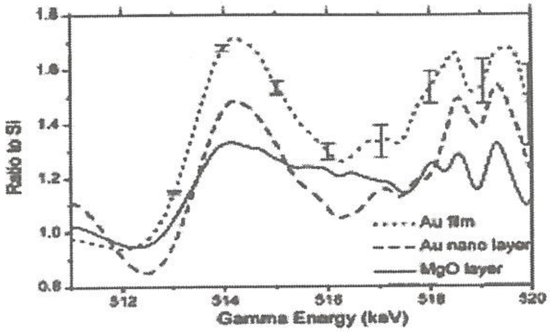

Fig. 8 The ratio of annihilation spectrum from Au nanoparticles embedded in MgO (dashed line), MgO (solid line) and Au film (dotted line) [23]

Fig. 9. A schematic of the PIPA set-up for studying large samples

While the application of PAS for studying nanostructures is extensive, new applications for nondestructive assay of large engineering materials are reported using the photon induced positron annihilation spectroscopy (PIPA). This technique has been utilized to study the stress induced defect studies on large engineering samples of practical importance. In this the Bremstrauhlung or nuclear reaction induced high energy photon are made to fall on the sample of interest. These high energy photons undergo pair production in the samples, and the annihilation characteristics of these positrons are monitored [26]. A schematic of PIPA set-up is shown in Fig. 9. The increase in the residual stress is manifested as increase in the S-parameter in these materials [27]. These studies have shown the promise in early stage detection of the fatigue and failure of samples like aircraft turbine blades, landing struts etc.

To conclude, positron annihilation technique, a spin off of nuclear sciences has emerged as a powerful nanoscopic technique which is interdisciplinary in nature encompassing theoretical physics/chemistry, condensed matter physics and material sciences. Availability of intense positron beams has widened the scope of this technique in

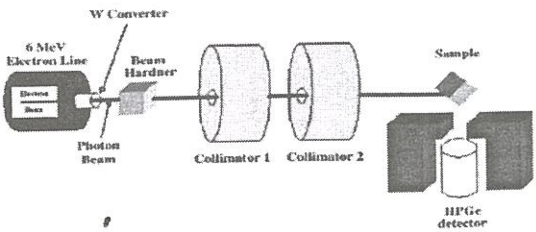

Fig. 9 A schematic of the PIPA set-up for studying large samples

fundamental as well as applied research considerably.

References

1. Dirac, P.A.M., 1930. Proc. Camb. Phil. Soc. 26, 361
2. Anderson, C.D., 1933. Phy. Rev. 43, 491.
3. Ore, A., and Powell, J.L., 1949. Phys. Rev. 75(11), 1696.
4. Shearer, J.W. and Duetsch, M., 1949. Phys. Rev. 76, 462
5. Dekhtyar, I. Ya, 1974. Physics Reports, 9(5), 243.
6. Dupasquier, A., and Mills, Jr., A.P., (Ed), 1995. Positron Spectroscopy of Solids, Proc. Internat. School of Physics «Enrico Fermi», Course CXXV, Varenna 1993, IOS Press, Amsterdam.
7. Hautakangas, S. et al., 2003. Phys. Rev. Lett. 90(13), 137402
8. Gebauer, J. et al, 2002. Phys. Rev. B. 66, 115206.
9. Ito, K. et al., 1998. J. Polymer Sci. B 36, 1141 and 1999. Polymer 40, 4315.
10. Bandzuch, P. et al., 2000. Phys. Rev. B. 61(13), 8784.
11. Miranda, R. et al., 1993. J. Mol. Catal., 78, 67.
12. Gidley, D.W. et al., 2006. Ann. Rev. Mater. Res. 36, 49.
13. Eijt, S.W.H. et al., 2006. Nature Materials, 5, 23.
14. Chou, K.W. et al., 2005. Acta. Phys. Polonica A. 107, 799.
15. Nagai, Y. et al., 2003. Phys. Rev. B. 67, 224202.
16. Nagai, Y. et al., 1999. Phys. Rev. B. 60, 11863.
17. Pujari, P.K. et al., 1994. Phys. Rev. B. 50, 3438.
18. Sundar, C.S., 2003. 'Positron annihilation studies in superconducting materials' in 'Principles and Applications of Positron and Positronium Chemistry', Editors: Jean, Y.C.; Mallon, P.E. and Schrader, D.M., World Scientific Publishing.
19. Pujari, P.K. et al 2002. Phy. Rev.B.66, 012518
20. Pethrick, R.A., 1997. Prog. Polym. Sci. 22, 1.
21. Kobayashi, Y. et al., 2007. Rad. Phys. Chem. 76(2), 224.
22. Webber, W.H. et al, 2002. Phys. Rev. B. 66, 041305(R).
23. Jun Xu et al., 2001. Phys. Rev. B. 64, 113404.
24. Falub, C.V. et al., 2002. Phys. Rev. B. 66, 075426.
25. Nagai, Y. et al., 2001. Phys. Rev. Lett. 87, 176402.
26. Selim, F.A. et al., 2003. Rad. Phys. Chem. 68, 427.
27. Roy, A.K. et al., 2005. J. Mater. Eng. And Performance. 14, 203.

XAFS: a Versatile Recent Technique for Sample Characterization

***Dr. (Ms.) Debdutta Lahiri** completed her Bachelors' (1994) and Masters' in Physics (1996) from Jadavpur University, Calcutta. In 1996, she left for the United States (University of Notre Dame) to pursue PhD program in Experimental Condensed Matter Physics. Her PhD work primarily involved study of nano-composite systems using XAFS technique. Following her PhD, she joined the University of Washington, Seattle as a postdoctoral associate. All her experiments during PhD and postdoctoral tenure were performed at the XAFS beamlines of Advanced Photon Source (APS), Argonne National Laboratory. She has measured XAFS in all possible modes at APS, to study a wide variety of systems such as nano-catalysts, biosensors, nano-alloys, superconducting systems, thin films, liquid-solid interfaces and liquid alloys. She was adjudged Awardee, Outstanding Recent result, APS-survey (2005) for her publication "Core-shell and alloyed Pt-Ag and Pd-Ag nanoparticles" in Journal of Applied Physics 97, 094304 (2005). Besides XAFS experiments, she was largely involved with the technological development of these XAFS beamlines, including the initiation of novel ns-resolved pump-probe XAFS experiments, and microfabrication of x-ray windows. In 2005, she joined Synchrotron Radiation Section, BARC, as a visiting scientist and secured a permanent position in High Pressure Physics Division in 2006. Her work at BARC, so far, has mainly been associated with the Indus-2 beamline development program. She has recently initiated XAFS experiments in collaboration with international synchrotron facilities. Her interests include problems in basic physics as well as applied research.*

Introduction

X-ray absorption spectrum of any material, around the absorption edge of any of its component atoms, exhibits a series of oscillatory fine feature (called "structure") that modulates the monotonically decreasing atomic absorption μ_0, typically by a few percent. This modulation is what is called "X-ray Absorption Fine Structure" i.e. XAFS (shown in Fig. 1) and has been attributed to the presence of other atoms around the excited atom. By analyzing these oscillations, detailed structural information (e.g. near neighbor species, their coordination, bond-lengths, Debye-Waller factor) about the "local" environment (within 8-10 Å) of the excited atom can be derived.

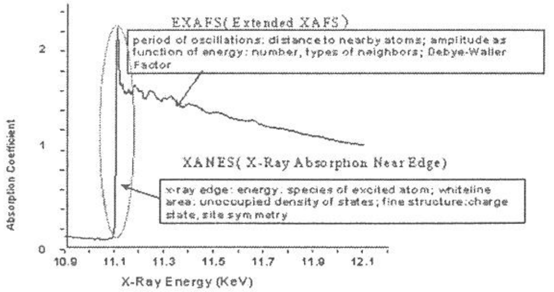

Fig. 1 A typical XAFS spectrum

The "local" nature of information is the key to the dramatic evolution of XAFS as a unique structural tool: it does not impose the requirement of crystallinity in a sample for analysis. This is particularly useful, in fact unique, for disordered samples (e.g. nanoparticles, glass, soil, liquid) where long-range-order (LRO) is absent and structural tools such as diffraction, HRTEM fail to extract details beyond a certain limit. Moreover, the "local" structural information, by itself, is often more important than the LRO information, as will be

Debdutta Lahiri, High Pressure Physics Division, Bhabha Atomic Research Centre, Trombay, Mumbai 400 085;
E-mail: dlahiri@barg.gov.in

discussed in the following section. The theoretical basis for XAFS being a "local" structural tool will be addressed in a later section. The second advantage of XAFS is tunability. In a multi-component sample, each of the atomic species can be separately excited to extract the structural information around it, i.e. yield the partial pair correlations. This is particularly useful to extract the information on the immediate neighborhood of a dilute dopant in a material, for example and separately establish the exact roles of the different atoms in the scientific problems of interest. Finally, XAFS is not inherently surface sensitive. By changing the angle of incidence of the x-rays on the sample, the penetration depth i.e. the information depth can be controlled and both bulk / surface studies can be made. Moreover, XAFS can be measured under any experimental condition viz. high- temperature, low-temperature, high-pressure. All of these advantages amount to the wide recognition of XAFS as unique technique.

The XAFS oscillations in the absorption spectrum, can be divided into 2 regions: the region close to the edge (within about 30 eV) is known as X-Ray Absorption Near Edge Structure (XANES) as shown in Fig. 1. The oscillations well above the absorption edge ($\geq$ 30 eV) are known as Extended XAFS (EXAFS). The local structural information comes from the EXAFS portion of the spectrum. On the other hand, XANES is sensitive to oxidation state of the excited atom (to be discussed). It has become clear in recent years that there is no fundamental distinction between the physics of EXAFS and XANES and the only distinction is one of resolution and complexity of the spectra. EXAFS and XANES are generally unified under the term "XAFS". XAFS is by far the only technique that gives simultaneous information on local structure and oxidation state. This unique strength of XAFS has significant applications, particularly in systems, where a correlation of structure and oxidation state may be important. Depending on the scientific problem of interest, either EXAFS or XANES or the entire spectrum may be used. The application of XAFS is wide-ranged: from basic physics, chemistry, biology to applied research such as catalysis, polymer science, environmental science, geochemistry, geophysics, optoelectronics, devices, materials science, surface / interfacial science etc.

Local Structure and its importance in Science

The term "local structure" is used to imply the structure in the immediate vicinity of a particular atom, say within 10 Å i.e. within a unit cell. Important length-scales in science such as coherence length of charge carriers in high-T_c superconductors, length-scale of magnetic interactions, chemical interactions, interfacial binding fall in the regime of "local" structure. Thus, any perturbation within this distance can significantly modify the relevant properties of a material. This "local" structure may be significantly different from the "average" LRO, detected by conventional structural tools such as diffraction. Details of local structure information can provide a key to understanding some of these material properties and novel phenomena. For example, (1) Nanophase separation or local structural inhomogeneities (undetected by diffraction) would have profound effect on superconducting properties. Such an anomalous mismatch in the crystallographic (from diffraction) and superconducting phase boundaries was indeed observed in La/Sr Cuprate [1]. The anomaly was resolved by XAFS which revealed the presence of "hidden" phases or locally tilted cuprate octahedra responsible for the persistence of superconductivity even beyond crystallographic transition. (2) An intrinsic (independent of sample preparation method) nanoscale clustering of the Sr ions in La/Sr-manganite CMR materials was detected, using XAFS [2]. This structural inhomogenity has strong implications for the physics of manganites, since almost all theoretical treatments of these materials have assumed homogeneity on the length scale of a few atomic bonds. Such clusters could act as nucleation sites for and account for larger-scale magneto-electronic phase separation. (3) The different degree of disorder induced by different dopants (Zn/Ni) in La/Sr Cuprates, detected by XAFS, could explain the different transport properties in these compounds (from scattering theory, wider perturbation is expected to result in stronger peaking of forward scattering and consequently, longer transport time) [3]. (4) Metal-insulator transition (MIT) has been observed in certain strongly (electron) correlated systems despite finite DOS at the Fermi level and macroscopic homogeneity of samples [4]. Such anomaly too could be accounted for only by local

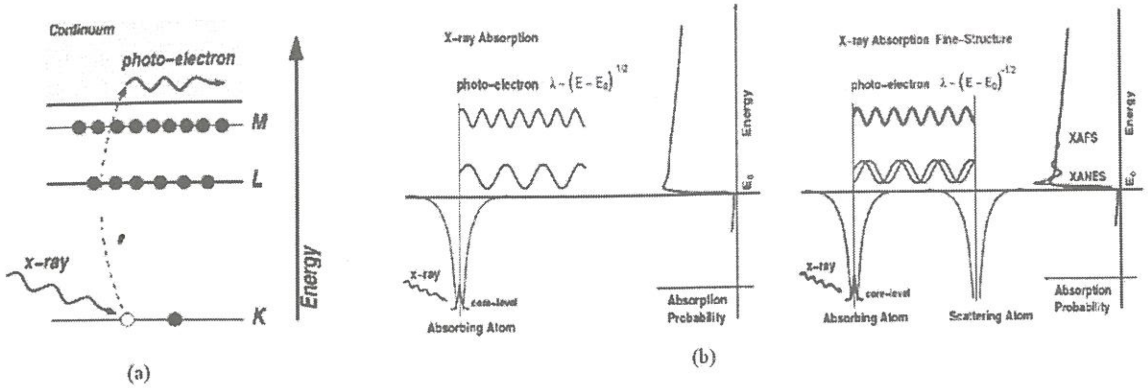

(a)

(b)

Fig. 2 *(a) the ejection of photoelectron following X-ray excitation. (b) The underlying physics of XAFS oscillatons the outgoing photoelectron wave gets backscattered from neighbouring atoms. The backscattered wave interferes with the original outgoing wave, giving rise to oscillations in the final state*

disorder. (6) Counter-intuitive switching of Se /Te atoms, resulting in higher strain, was detected near the interface of ZnTe/CdSe superlattices [5], using XAFS. This observation led to reconsideration of the strain theories for epitaxial film growth. (7) The luminescence stability of CdSe biosensors (size 3 nm) was observed to be much better for particles synthesized with a starting ratio of excess Cd. With XAFS, it was detected that, for the samples synthesized with excess Cd, Cd formed an extra coating on the surface of CdSe nanoparticle. This coating is believed to render the nanoparticle better protection and stability against light and water and hence, the observed better stability in luminescence [6]. In this context, the extent of coating / wetting (whether complete coating or partial wetting of the surface) is important to know and can be determined to a large extent, using XAFS [7]. (8) Room–temperature alloying was detected in 2 nm core-shell particles and several cylindrical nano-alloys, using XAFS [8]. Such detection of room-temperature alloying, absent in bulk, shed important light on the basic physics of nanoparticles (viz. defects, kinetics, etc.) and has potential application in nano-sensors (where alloying is an important consideration) [7,9]. (9) The exact mechanism of preferential glass formation in certain alloys (e.g. Pd-doped Zr-alloy) was recently established by XAFS [10] : such finding has important bearing on the successful synthesis of metallic glasses. (10) The exact structures of ion-water and ion-ion species at high temperatures, measured by XAFS, have improved our understanding of these systems and will have an impact on all systems that contain water (biochemistry, chemistry, geochemistry, waste destruction, corrosion, ion separations) [11]. (11) Using microbial activity to 'fix' radionuclides into an insoluble form (that cannot be readily dispersed) has been accepted as a strategy to control actinide contamination of soils, sediments and water. XAFS analysis indicated a contraction of 0.07 Å in U-U distances in such biogenic uraninite (UO_2) particles (2 nm size) compared to bulk uraninite, implying a significant displacement of surface U(IV) ions. This contraction quantitatively amounts to a stress that represents more than a billion-fold increase in the solubility product and determines the fate (mobility and reactivity) of these particles [12]. These are only a few examples of the kind of local structural information XAFS can extract and their implications in science and technology.

Theory of XAFS

The interpretation of XAFS was originally envisaged from band-structure considerations [13] and it took nearly three decades (until the late 1970-s) to realize the present short range order (SRO)-based theory and covert XAFS into a useful quantitative structural tool [14]. The development of the current XAFS theory is credited to Stern, Sayers and Lytle. The present theory of XAFS rests on the simple picture of photoelectron ejection from an atom following the absorption of x-rays with energy above one of the binding energies of the atom [15]. X-Ray absorption in the regime of these binding energies (hard x-rays and soft x-rays to a certain range) is indeed dominated by photoelectron absorption. While the final state of the ejected photoelectron is a free electron state for an isolated atom, the photoelectron gets backscattered when there are neighboring atoms around (Fig.2). The backscattered electron wave then interferes with the original outgoing photoelectron wave, giving rise to an oscillatory final state vector. This is the origin of the XAFS oscillations, observed in the absorption spectra (Absorption is proportional to the transition matrix between the initial and final state vectors [16]. The final state vector being oscillatory in this case results in oscillatory absorption).

XAFS is defined as the fractional change in absorption from the mean absorption (i.e. $\chi = \frac{\mu - \mu_0}{\mu_0}$) where μ_0 is the slowly varying background absorption from an isolated absorbing atom and other processes. The equation for XAFS can be derived using the electron-photon interaction Hamiltonian [15,17] and is simplified for the EXAFS regime (photoelectron kinetic energy > 30 eV) with certain valid assumptions for elastic scattering [15]. With these assumptions, the XAFS equation stands as

$$\chi(k) = 3\sum_j \frac{S_0^2 m}{2\pi\hbar^2} \frac{t_i(2k)}{(kr_j)^2} e^{-k^2\sigma^2} e^{-2^r/\lambda} \cos^2\theta_j \sin\left[2kr_j + \delta_j(k)\right]$$

The XAFS oscillations are thus expressed as a function of photoelectron wave vector k, since k and r (real space coordinate) are conjugate variables. From the expression, it is observed that the period of XAFS oscillations is given by r_j – radial coordinates of the neighboring atoms and the amplitude is proportional to N_j, the (coordination) number of such neighboring atoms. $t_j(k)$ and $\delta j(k)$ are respectively the backscattering factor and phase shift introduced by the surrounding atoms and are specific to the atomic type. The Z-dependence of these factors is well-tabulated [18] or can be calculated ab-initio and is used to distinguish the type of surrounding atoms, with a resolution of $\Delta Z \geq 5$. The $e^{-k^2\sigma^2}$ factor (Debye-Waller factor or DWF) accounts for the bond-length distribution (for small disorder). This disorder could be static (structural) or thermally induced. For large or non-Gaussian disorder, cumulant and other non-Gaussian theories have been developed [15,19]. θ_j is the angle between the inter-atomic bond and electric vector. In a polycrystalline sample, the unit cells are randomly oriented and $\langle \cos^2\theta_j \rangle = \frac{1}{3}$. In polycrystalline samples, therefore, angular-resolved structural information is lost. However, in samples with well-defined axis, this $\cos^2\theta_j$ dependence can be utilized for a better resolved structure – a method called "polarization" XAFS (to be discussed later).

A very important factor in the XAFS equation is the exponential decay factor $e^{-\frac{2r_j}{\lambda}}$ in the numerator, which arises due to the inelastic losses suffered by the photoelectron wave. In order for the original outgoing and the backscattered photoelectron waves to interfere, coherence of the two waves needs to be preserved. λ is the mean free path distance of the electron up to which it can travel without being inelastically scattered and is usually of the order of 10-15 Å (represented by a universal curve) [15,20]. Contributing to these inelastic losses are excitations such as plasmons, electron-hole pairs and finite lifetime of the core hole [21]. The "local" nature of structural information obtained from XAFS analysis stems from this exponential decay factor and r_j^2 factor in the denominator of the XAFS expression. Due to both these factors (λ) and (r_j^2), structural information beyond 6-8 Å from the central absorbing atom is almost absent. It may be further mentioned that core widths can be as large as several eV for the deeper core states of heavy atoms, washing out the fine structure.

As can be seen, the XAFS expression is the superimposed result of the structural information from different atoms at different distances. To decouple the information, the XAFS oscillations are Fourier transformed to r-space that yield a radial distribution function (corrected for phase-shifts) of atoms – the position of the peaks indicate the different radial distances at which the surrounding atoms are located and the height of the peaks are proportional to the coordination number of the atoms

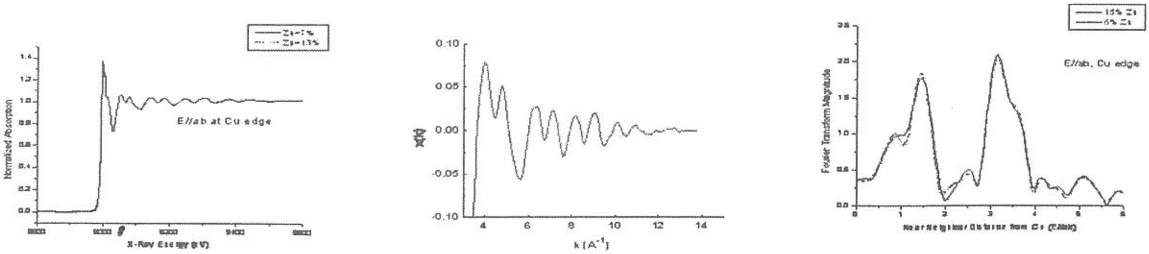

Fig. 3 XAFS spectrum; oscillations extracted in k-space; Fourier transform of the oscillation in r-space. The location of the peaks corresponds to the different bond-lengths and the height / shape of the peaks corresponds to coordination number. Debye-Waller factor and atomic species

(Fig. 3). Each of these peaks is then fitted using the structural parameters (viz. coordination number, species type, bond-length, DWF) as variables. Theoretically, the accuracy within which these parameters can be determined are $r = \pm 0.01$ Å, $\sigma^2 = \pm 0.002$ Å^2, $N = \pm 1$ and $Z = \pm 5$.

Although the above XAFS equation is derived for the K-edge excitation, it can be generalized for the L- or M-edges, except for the angular dependence-related complication arising in oriented samples at these edges [15]. The above equation rightfully ignores the contribution from multiple scattering, which is low in the EXAFS regime except for forward scattering [15]. Generalizing the equation to accommodate multiple scattering is straightforward. Recent advances in XAFS analysis attempt to utilize the multiple scattering phenomena to detect angular distortion: any deviation from forward scattering (i.e. linear configuration) results in abrupt drop in scattering amplitudes [22].

Data Analysis

XAFS data analysis is mostly non-trivial and may be divided into two steps: (1) Data Processing, which isolates the fine structure oscillations from the experimental absorption data and (2) Data fitting, which involves Fourier transforming the XAFS oscillations from k-space into r-space, constructing the appropriate structural model and then fitting the peaks in r-space using a least squares fitting method.

Data Processing

The data is popularly processed with a program called ATHENA [23] and involves (a) merging of several scans to reduce statistical noise, (b) removal of artifacts like glitches if present in the raw absorption data, (c) determining the edge energy E_0 (to be set as the "0" point in k-space): the edge is usually defined at half the rise of absorption curve, (d) pre-edge background removal (note that the pre-edge extends as a background into the post-edge and needs to be subtracted before normalization), (e) normalization to the edge step to make all datasets comparable, (f) post-edge background removal (polynomial fitting), (g) extracting the oscillations and interpolating them to an equally spaced grid in photoelectron wavenumber k. The biggest challenge in data processing is the post-edge background removal. In fact, the credibility of structural information from XAFS analysis hinges on the accuracy of background removal, to a great extent. Incorrect background removal will lead to distorted oscillations and consequently, incorrect structural information. The background subtraction requires scrutiny of an experienced analyst.

Data Fitting (post background-subtraction process)

The background-subtracted XAFS data (in k-space) is Fourier transformed to obtain radial distribution function of the atoms in real (r) space. After the Fourier transform is extracted, the next step is to fit the r-space data with a reasonable physical model. The scattering functions are calculated from the input model with the program called FEFF8.0 [24] and are fit to the data using the fitting program FEFFIT [25]. FEFF8.0 program requires an initial input for the geometric distribution of neighboring atoms to calculate the scattering contribution from each of them. FEFFIT allows for a variation of these initial input parameters to fit the peaks of interest, using Levenberg-Marquardt method of nonlinear least-square minimization [26]. The fit quality is judged by a well-defined figure-of-merit [27].

Complications in XAFS analysis arise from (1) limitation on the number of variables due to the finite content of an XAFS signal: [28] The data range is constrained by data quality or the degree of disorder in the sample. While the fitting variables suffice in most cases, often a peak may have contribution from multiple atoms. The number of variables required for fitting, then, may fall short of what is available from the finite data content. This often poses an upper limit on the feasibility of XAFS analysis of certain samples. While this problem can sometimes be resolved by certain analytic strategies, it is generally encouraged that good quality data up to a long range in k-space be obtained to increase the information content. (2) Correlation between different variables: The correlation between different variables is clear from the XAFS equation. Unambiguous values for most of these variables can be isolated in the simplest case (say, where the near neighbor species are clearly distinguishable) since bond-length value will be defined by the location of the peak, Debye-Waller factor will be determined by the width of the peak. However, ambiguity in these parameters may arise due to leakage from other peaks and other factors. The problem is then similar to having excess variables for solving a single equation. Some of these ambiguities may be resolved by using physical intuition about the samples. Before stating conclusive results, several models need to be considered and accounted for by adding appropriate error bars to the parameter values. It is said that in XAFS analysis, knowledge of the error bars is as important as the parameters. The error bars are often reduced by simultaneous fitting of different datasets. For example, in a Pt-Ag alloy, the Pt-Ag bond parameters can be simultaneously fit from both Pt and Ag edges to obtain a unique answer.

Including all of the above steps, XAFS data analysis can be considered to be mostly non-trivial and rigorous and must be carefully done to arrive at the correct conclusion.

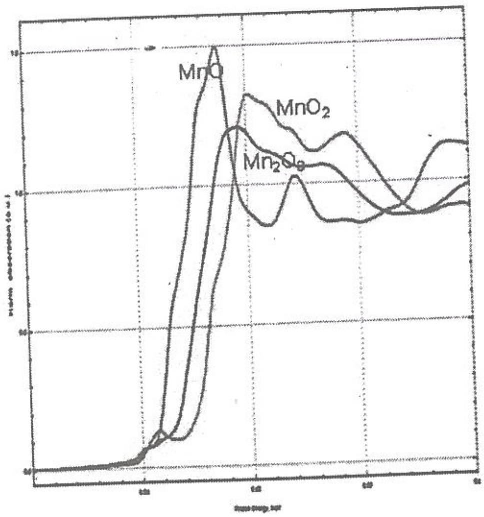

Fig. 4 *The edge position shifts higher energies with increase in valence state*

XANES

Although the basic physics of XANES is the same as XAFS, the kinetic energy of the photoelectron is low in the XANES regime which results in phenomena different from EXAFS. First, the De-Broglie wavelength of the photoelectron is very large (~ 100 Å) at this low energy. This spills over several bond-lengths and therefore, the resolution to detect local structure is lost. Secondly, the assumptions (e.g. hard-sphere scattering potential, plane-wave approximation, single-scattering) leading to the simplified solvable XAFS equation are no longer valid in the XANES regime [29]. For all these factors, XANES interpretation is complicated and cannot be employed to derive structural information directly. On the other hand, because of the low kinetic energy, the photoelectron becomes very sensitive to the surrounding potential and important information such as charge transfer / change in valence state etc. can be obtained from the XANES features.

Valence State

A change in valence state is reflected in a shift in the absorption edge position – the shift is towards higher binding energies for a higher oxidation state (Fig.4) [30]. The positive shift in the edge energy

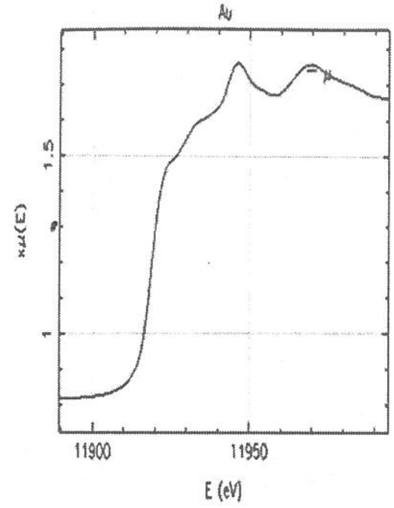

Fig. 5a Whiteline absent in metallic Au

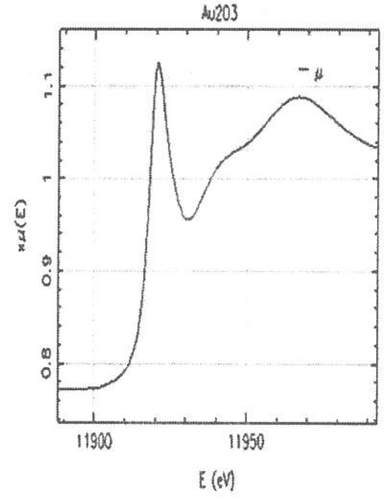

Fig. 5b A shart whiteline is present in Au_2O_3.

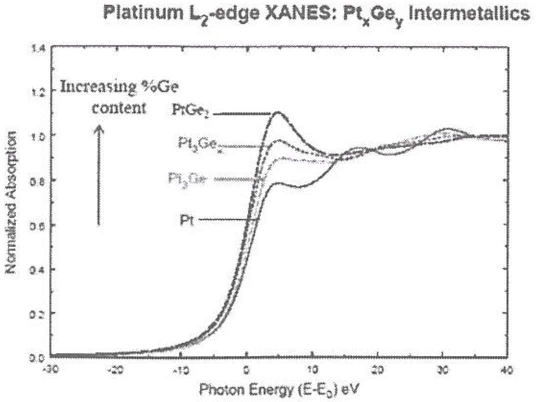

Fig. 6a Whiteline intensity used to monitor charge transfer in Pt-Ge intermetallics. With increasing Ge content, there is more electron transfer from Pt to Ge

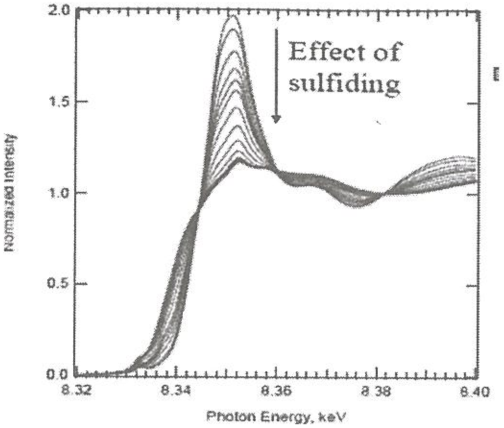

Fig. 6b Ni K-edge XANES of in situ sulfiding of a Ni/Al_2O_3 catalyst.

with increase in valence can be understood conceptually to be due to an increase in the attractive potential of the nucleus following the loss of an electron. Another indicator of oxidation state is the so-called "white-line" which is a sharp peak in the spectra (Fig.5) just above the edge [31]. The white-line intensity is proportional to the density of the unoccupied final states which is related to the oxidation state of the sample: the higher the oxidation state, the sharper is the whiteline intensity [32]. The determination of the exact oxidation state from whiteline intensity is, however, complicated by the effect of coordination geometry on the transition probabilities [30]. Nevertheless, the systematic (relative) change in whiteline intensity can be used to monitor relative charge transfer-related phenomena such as in intermetallics, as a function of dopant concentration or the time evolution of species (oxidation/ reduction) during a chemical reaction by time-resolved in-situ experiments (Fig.6). In this regard, two very important applications of XANES lie in (1) environmental science where the speciation of metals in contaminated soil, water is important to understand their fate, toxicity, mobility etc. [33] and

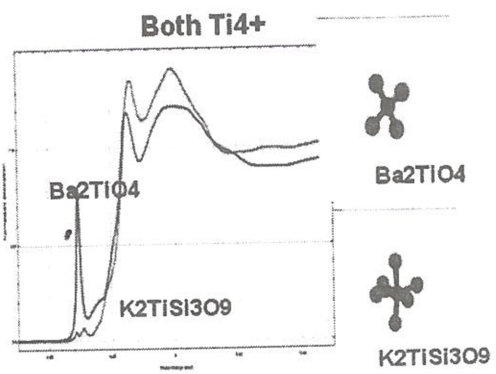

Fig. 7a Ti K-edge XANES shows dramatic dependence on the local coordination chemistry

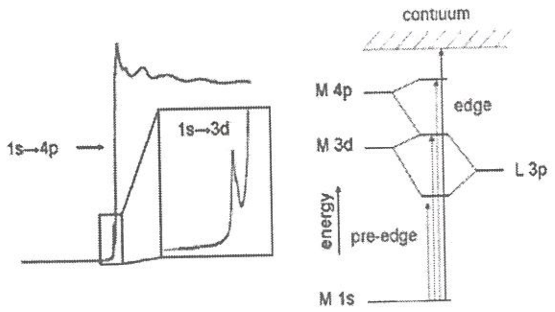

Fig. 7b The physics of pre-edge features. Intense edge absorption due to dipole allowed s → p transition (Δl=±1). Weaker pre-edge feature results from mixing of 3d-4p orbitals of suitable symmetry (or from quadrupolar allowed transition-~2orders magnitude weaker)

(2) catalysis – e.g. speciation of segregated metallic phases in fuel cell, etc. [34]. In this context, a major advantage of XANES, compared to other techniques (such as XPS) for speciation, is that it can be employed on solutions / aqueous systems (e.g. Arsenic-contaminated water) or very dilute systems (with ppm concentration) and it is not inherently surface-sensitive. The surfaces of many samples are prone to oxidation. In surface-sensitive techniques such as XPS, the signal from surface oxidation often overshadows the signal of interest. This problem is eliminated in XANES since, for bulk-mode measurement, signal from the surface constitutes an insignificant fraction of the data.

Site Symmetry

XANES can be used to quickly identify the coordination geometry (4-, 5-, 6-fold) of the near neighbors, bypassing detailed structural analysis with EXAFS. The coordination chemistry often becomes important to know in order to determine an element's toxicity / reactivity [35]. An element, with the same oxidation state, may exist in different coordination geometry in different compounds. Coordination geometry lays its signature in XANES via orbital hybridization of the unoccupied states. Although X-ray absorption is dominated by dipole transition rule ($l = \pm 1$, e.g. s-p transition), weaker pre-edge feature results in XANES if hybridization of 3d-4p orbitals of suitable symmetry exists (or from quadrupolar allowed transition – ~2 orders magnitude weaker) (Fig.7). For octahedral symmetry, no p-d mixing is allowed and only a weak pre-edge feature may be present from quadrupole transition. Mixing is allowed for distorted octahedral symmetry increasing the intensity of pre-edge feature. The intensity of pre-edge feature is the highest for tetrahedral symmetry.

XANES Data Analysis

Ab-initio XANES data analysis is far more complicated than EXAFS. Because of high sensitivity of the photoelectron to subtle variation in the surrounding potential, the biggest challenge in ab-initio XANES calculation is the construction of the appropriate potential. Unlike EXAFS, no simplified approximation for scattering is valid in the XANES regime and there is no end to the accuracy or details that need to be accommodated to construct the correct XANES features. The contributing factors to XANES features are many (e.g. multiple scattering, bond-length, oxidation state) and there is no simple way to decouple these. Thus there is no clear way to determine if the deviation in XANES data from the calculations is due to an incorrect model or inaccurate scattering approximations. Although recent fitting programs (FEFF8.0) have been successful in fitting the XANES of known metals and oxides, the ab-initio fitting of the XANES for an unknown material has not been reported yet.

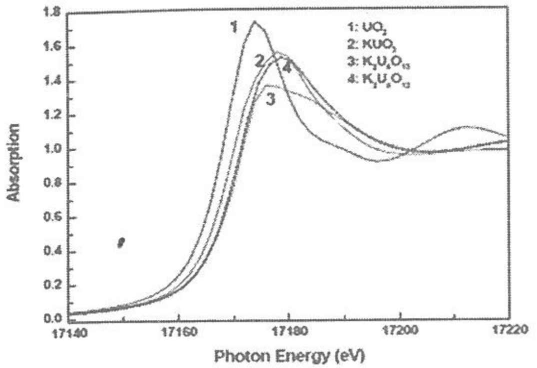

Fig. 8 The XANES of $K_2U_4O_{12}$ lies between the XANES of KUO_3 (+5 valence) and $K_2U_4O_{13}$ (+6 valence). It is clear that +4 valence state is absent in $K_2U_4O_{12}$. UO_2 was used as the standard for +4 valence state.

The analysis of XANES for unknown materials has thus largely been qualitative in nature and limited to speciation / fingerprinting, rather than deriving the electronic structure ab-initio. It need be mentioned that for speciation, the absolute values of edge position or whiteline intensity do not matter. It is the relative change in whiteline intensity or edge position that is used to monitor charge transfer phenomena. For example, one could say if Au in a particular material is in a positive oxidation state or in the pure metallic form, by comparing its XANES (whiteline, edge position) with the XANES of pure Au metal [36,37]. XANES has been employed to fingerprint mixed-valent systems, using the XANES fitting program in ATHENA software [23]. If a particular element is in mixed valence state, the proportion of the different oxidation states can be determined by linearly fitting its XANES with the weighted combination of the XANES measured on relevant standard oxides [38]. In this context, the purity of the standards is extremely important. As shown in Fig. 8, the (mixed) oxidation state of U in $K_2U_4O_{12}$ was found to have 66% (+ 5) and 34% (+6) states. $K_2U_4O_{12}$ is a reactor by-product and the speciation was important to explore its catalytic potential. The references used for +5 and + 6 oxidation states were KUO_3 and $K_2U_4O_{13}$ respectively. The possibility of +4 oxidation state was ruled out, by comparing with standard UO_2. This quantitative speciation might not have been unambiguous though, had there been too many mixed phases. Despite such limitations, XANES is widely used for its clear advantages (mentioned earlier) over other speciation techniques and publications from XANES itself amount to 500 per year.

Some recent work in catalysis, involving XANES (and EXAFS for structural correlation), include correlating local structure with redox reactions in novel catalysts [39], identification of novel potential catalysts from reactor by-products etc. [38], understanding the performance of photo-catalysts [36,37], doped-lithium ion batteries [40], self-regeneration mechanism of perovskite catalysts for automotive emissions [41], etc. Some recent work in environmental science, involving XANES, include lead speciation in municipal solid waste incineration (by weathering) for safety improvement [42], speciation of tin in sediments for toxicity [43], study of Zn sorption to natural apatites for remediation of contaminated sites [44], Co, Ni speciation in cement [45] etc.

Experimental Method

Experimental Setup

XAFS detection basically involves measuring absorption, either directly by transmission through the sample or indirectly from processes (fluorescence or Auger electrons) that are proportional to absorption. In a transmission experiment, the absorption is directly measured by the attenuation of the x-ray as it passes through the sample. The absorption is then obtained from the equation: [ìx = ln (I_0 /I_t)] where I_0 is the intensity of the beam before the sample and I_t is the intensity of the beam after the sample. Fluorescence-mode measures the absorption indirectly through the fluorescence photons (= I_f / I_0), emitted from the excited atom. In the fluorescence-mode, the sample and the fluorescence detector are aligned at 45° and 90° respectively, wrt the beam. This geometry minimizes the background from elastically scattered photons. The Auger electron current (=I_e/I_0) is measured in the so-called total-electron-yield (TEY) mode. The information depth is defined by the mean free path of these electrons (~30 Å), which makes these measurements surface-specific. The different experimental configurations are shown in Fig. 9a

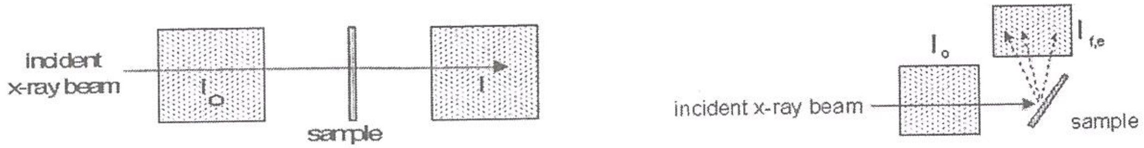

Fig. 9 The experimental configuration of (a) transmission and (b) fluorescence / TEY XAFES

and 9b. Out of the three methods, transmission always measures the bulk, TEY always measures the surface and fluorescence can be used to measure bulk or surface, depending on the angle of incidence of the beam on the sample.

These measurement methods have their own advantages. While the experimental setup of the transmission-mode is easier, the sample requirements are much more stringent due to the logarithmic nature of the signal [46]. The samples are required to be uniform and fairly concentrated. Fluorescence- and TEY-mode experiments are a lot more flexible this way. However, the fluorescence yield is low (20-30%) for low-Z atoms (Z < 30) and a good XAFS signal cannot be obtained in fluorescence mode at the absorption edges of these atoms. Then, for thick samples (not measurable in transmission mode), it is very important that the concentration of the element of interest not be too large; else, it results in a nonlinear distortion of the measured spectra, the so-called "self-absorption" artifact [47]. Moreover, the instrumentation required for fluorescence-mode measurements is very expensive (to be described in the instrumentation section) and not available at many beamlines. TEY is the most widely used detection technique in the soft x-ray region (< 2 keV), since fluorescence yield is low. Although it should be clearly preferred for surface experiments in particular, there are often artifacts caused by sample charging for insulating samples [48]. This poses a restriction on the range of samples that can be actually measured by TEY. The final choice of the mode of XAFS measurement is thus determined by the sample in question, the energy edges to be measured and the availability of the facilities.

Instrumentation

The main requirement for XAFS measurements is a source with (1) a continuous energy spectrum to be able to explore the structure around a wide range of atomic species and (2) very high flux in order to reduce statistical noise in the data. Any noise in the data can be misinterpreted to be sharp oscillation which, when Fourier-transformed, gives rise to spurious peaks in r-space and interfere with the real structure. Both of these experimental requirements are fulfilled by a synchrotron source which has emerged as almost the singular and indispensable seat of XAFS measurements today. Although laboratory XAFS facilities are in vogue, the scope of XAFS studies at a laboratory source are limited by statistics, resolution and energy range [49]. For example, the data collection time at a laboratory is 20 hours compared to 1 hour at synchrotrons. The laboratory system can be useful, though, for fast implementation of idea by timely experiment since allocation of synchrotron beamtime is infrequent and competitive. Current laboratory-based XAFS literature mainly report XANES studies with improved resolution at the cost of intensity.

The strength and impetus of XAFS as a technique has evolved largely with the development of synchrotrons. The instrumentation for XAFS experiments is standardized [50] and involves (a) cryostat-cooled monochromator / polychromator (usually Si in the hard x-ray regime) to filter out the required energy range from the entire synchrotron spectrum; (b) harmonic rejection mirror to reject the higher harmonics of the fundamental energy, reflected off the monochromator; (c) high-Z material slits to define the beam; (d) translation stage to optimize the sample position on the beam and (e) detectors.

During the experiments, this instrumentation is optimized for maximum flux / signal. The exact selection of the monochromator plane (e.g.111 vs. 311), mirror material (glass / Pt / Rh/ Au), etc. is determined by the energy edges to be measured. For detectors, gas-filled ionization chambers work best in most of the cases. Selection of the correct gas mixture in the right proportion, for maximum signal, involves absorption calculations. Besides ionization chambers, photodiodes, scintillation detectors etc. may be used for monitoring the transmitted intensity. The detectors for fluorescence detection are a little different because the fluorescence x-rays are emitted isotropically and are of much lower flux. These detectors are designed to subtend a large solid angle with respect to the sample and consequently, to collect as many fluorescence photons as possible. The so-called "Lytle" detector [51], the solid-state energy-discriminating detectors (e.g. Ge multi-element detector), "Bent Laue Analyzer" detectors [52] are used to measure fluorescence. It has been seen that the quality of fluorescence data deteriorates drastically in the absence of these specialized (expensive) detectors, which makes the fluorescence-mode experiments an expensive proposition. The detector for TEY involve grid detector and electron multipliers [53].

All of this instrumentation can be adapted for soft x-ray regime by including vacuum paths and suitable optical elements.

Alignment

As mentioned above, noise is a major consideration for XAFS and the entire experiment should be optimized to reduce statistical noise to about 0.1% of the signal. This requires a counting statistics of ~ 10^6-10^7/ sec and incident photon flux of ~ 10^9/ sec for efficient data collection. In this regard, care is taken in every step of the alignment procedure, viz. selection of the appropriate monochromator plane, mirror material etc. and aligning them to maximize the beam intensity reflected from the optical elements, controlling the slit size, selecting the best part of the sample (for non-uniform samples), optimizing the detectors and the associated electronics (voltage, amplification, offset etc.) to obtain maximum signal-to-noise ratio. Sources of systematic noise such as microphonics (e.g. vibrating sample holders, detectors), non-linearity of detectors, beam movement, etc. must be eliminated [54]. The entire optimization process, with all these parameters, is non-trivial and can take up to 70% of the allocated experimental beamtime.

Sample Preparation

Good sample preparation is crucial to obtaining correct XAFS data. From calculations and experiments, it has been realized that for good signal-to-noise ratio in transmission experiments, the sample should have a thickness of ~2 absorption lengths at the edge of interest [55]. The absorption thickness (5-20 μm) of a sample is pre-calculated from the absorption cross-sections of the constituent atoms and atomic density information [56]. For certain samples, it may be difficult to obtain such small thickness due to limitations of synthesis technique. In these cases, the samples could be referred for measurement in fluorescence-mode, as long as it is dilute [47]. As mentioned earlier, samples should be made uniform on a scale of one absorption length, for transmission-mode experiments. The sample requirements for fluorescence-mode experiments are much more relaxed. In general, even for fluorescence measurements, uniform sample is preferred to compensate for noise due to possible beam movement, structure in beam etc.

Single crystals are discouraged for XAFS measurements. The easiest form of samples for XAFS is powder, uniformly spread on tape. The tape material (e.g. Teflon, Kapton, Mylar, Scotch) should not have an absorption edge close to the edge of interest and should be thin in order to reduce extraneous absorption. The particle size of the powder should preferably be of the order of 5 ìm, especially for low edge measurements. For temperature-dependent experiments, the powder should be mixed with resin and graphite and pressed into the form of thin pellets. The thickness of the pellet can be carefully controlled by mixing the sample, graphite and resin in the right ratio. The details of sample preparation are described elsewhere [3]. Liquid samples are usually contained in quartz holders with Kapton-sealed windows for x-rays to pass. Thin films are generally measured in fluorescence or TEY-mode, unless the substrate is transparent enough for transmission experiments (such as nm-thick quartz or silicon nitride windows). All samples, in general, should be free from contamination.

Sample holder designs may range from simple to moderately complex, depending on the experimental requirement. The material of the sample holder is usually a non-reactive low-Z material (such as Boron Nitride, Aluminium, plexiglass, glass, Teflon), with well-sealed micron-thin transparent windows (Kapton, Beryllium, Si_3N_4, Mylar, diamond) for the passage of x-rays.

XAFS Measurements under Special Conditions

High- and low- temperature, High Pressure

Many interesting phenomena occur under special thermodynamic conditions. XAFS may be used where a local structural understanding of these phenomena / phase transitions is required [57]. The XAFS experiments then require special sample holders and in the case of high pressure measurements, special focusing optics, to obtain a very small spot size on the small sample [58,60].

Grazing-angle XAFS

Knowledge of the local surface / interfacial ordering, strain, segregation, preferential bond formation, binding environment of adsorbates etc. can be extremely important for the development of devices (e.g. superlattices) [61] or understanding wetting phenomena in general [62]. Such relevant surface/interface structure can be probed, measuring fluorescence in the grazing-angle mode. The sample is mounted on a goniometer, at an angle of incidence lower than the angle for total internal reflection. By changing the angle, the penetration depth of the x-rays can be controlled and depth-dependent information can be extracted. Due to the specialization, expense and complication involved, many XAFS beamlines do not house this facility, often restricting the scope of these studies. The difficulties in grazing-mode XAFS can be overcome by substituting with TEY-mode XAFS measurements, for a restricted range of samples and where only surface (within 30 Å) study is sufficient.

Polarization-dependent XAFS

Synchrotron x-rays have the advantage of being plane polarized in the plane of the beam. For a sample with a well-defined axis, the $\cos^2\theta$ dependence of the XAFS equation can be used to resolve the structure of the sample into two directions viz. along the axis and perpendicular to the axis. This is achieved by orienting the sample axis once along the plane of polarization of the beam and then perpendicular to the plane of polarization. This technique is extremely useful in detecting anisotropic structural changes such as Jahn-Teller distortions, etc. In fact, this technique always provides with better-resolved and more detailed structural information, compared to ordinary XAFS and is evidently preferred. Typically, powder samples are magnetically aligned for these experiments [3]. The feasibility of the polarization experiments hinges on the feasibility of magnetic alignment, which depends on the magnetic moment of the sample of interest. Moreover, L- or M- edge measurements are discouraged for oriented samples because of the complication in angular-dependent analysis [15]. This narrows the range of samples that can be studied using polarization-dependent XAFS.

Feasibility / Plausibility of XAFS study

The feasibility / plausibility of XAFS study is determined by certain scientific and practical considerations: (1) The scientific problem of interest: whether XAFS is the most appropriate technique to solve the problem. XAFS applies best to problems where local structure can be expected to be different from LRO and can account for certain observed properties; or, in amorphous/ disordered/ nano-systems where other structural techniques such as diffraction, where HRTEM fail to give detailed information; or, for the determination of oxidation state, particularly, when the correlation between structure and oxidation state is important. Besides the scientific interest, the feasibility of data analysis should be taken into consideration: whether the structure of interest can be analyzable / resolved unambiguously (e.g. bond-lengths of interest are separable, etc.). Analyzable quality XAFS data is largely reliant on the availability of synchrotron x-rays. Since beam-time is infrequently allocated, it is encouraged that comparable in-house techniques should be employed to resolve the systems to the maximum possible extent and XAFS should be considered only when it is absolutely indispensable and realized to be feasible. (2) Technological considerations: The choice of samples is often limited by technological considerations: (a) whether the edges of interest (atomic species) are available with reasonable flux, at the synchrotron. (b) For XANES studies, whether the available energy resolution is sufficiently small. (c) Whether there are similar atoms in the sample: in samples with similar (ΔZ=1, e.g. Cu, Zn) atoms, sharp XAFS oscillations from one edge (Cu) may extend into the next edge (Zn), resulting in an oscillatory pre-edge for the latter edge and rendering the data unusable [3]. (d) Whether the sample is non-uniform or very dilute: many XAFS beamlines do not house the expensive detectors for fluorescence-mode measurements, required for these samples. (e) For XAFS experiments under special conditions, the availability of the required equipments should be confirmed e.g. cryostat sample holder for low-temperature measurements, high temperature furnace, goniometer for surface studies, diamond anvil cell for high-pressure XAFS.

Scope of XAFS at Indus-2

The present XAFS beamline at Indus-2 synchrotron, RRCAT is designed for transmission-mode experiments, using a polychromator and CCD detector [63]. Hence, uniform, not-too-thick and not-too-dilute samples is a pre-requisite. The beamline delivers energy between 5-20 keV, with a reasonable flux, which covers the edges of a wide range of atomic species (K-edges: Z=22-41; L_3-edges: Z=73-83, Lanthanides, Actinides). The energy resolution varies between 0.5 eV at 5 keV and 2 eV around 20 keV. Many samples, compatible with transmission-mode and not requiring any special thermodynamic condition or surface/interface XAFS, may be considered for measurement. Time-resolved (~ 1sec) experiments may be performed in addition. Under the XIth plan, instrumentation is being developed for accommodating high-pressure, high-temperature and low-temperature experiments at the present XAFS beamline and constructing a separate DCM-based XAFS beamline [64] for fluorescence-mode measurements (to accommodate thick, dilute, non-uniform samples) with better energy resolution. After the execution of the XIth plan, Indus-2 is expected have a versatile and comprehensive XAFS facility, comparable with any international XAFS beamline.

References

1. D. Haskel, E. A. Stern, D. G. Hinks, A. W. Mitchell, J. Jorgensen and J. Budnick, Phys. Rev. Lett. 76, 439 (1996).
2. Tomohiro Shibata, Bruce Bunker, J F Mitchell and Peter Schiffer, Phys. Rev. Lett. 88 (20), 207205-1 (2002).
3. D. Haskel, E. A. Stern, V. Polinger and F. Dogan, Phys. Rev. B 64, 104510-1 (2001); Debdutta Lahiri, Physica C 436, 32 (2006).
4. Kalobaran Maiti, Ravi Shankar Singh and V. R. R. Medicherla, Phys. Rev. B 76, 165128 (2007); Jungho Kim, J.-Y. Kim, B.-G. Park and S.-J. Oh, Phys. Rev. B 73, 235109 (2006).
5. K. M. Kemner, B. A. Bunker, H. Luo, N. Samarth, J. K. Furdyna, M. R. Weidmann and K. E. Newman, Phys. Rev. B Rapid Comm.46, 7272 (1992).
6. Debdutta Lahiri, Shailesh N. Sharma, S. Zeena and Bruce A. Bunker, J. Surface Sci. Technol. 21(1-2), 11 (2005).
7. Debdutta Lahiri, Bruce Bunker, B. Mishra, Z. Zhang, D. Meisel, C. M. Doudna, M. F. Bertino, F. D. Blum, A. T. Tokuhiro, S. Chattopadhyay, T. Shibata and J. Terry, J. App. Phys. 97, 094304 (2005).
8. Tomohiro Shibata, Bruce A. Bunker, Zhenuan Z. Zhang, Dan Meisel, Charles. F. Vardeman II and J. Daniel Gezelter, J. Am. Chem. Soc. 124, 11989 (2002).
9. C. M. Doudna, M. F. Bertino, F. D. Blum, A. T. Tokuhiro, D. Lahiri, S. Chattopadhyay and J. Terry, J. Phys. Chem. B 107, 2966 (2003).
10. L. Yang, J. Z. Jiang, T. Liu, T. D. Hu and T. Uruga, Appl. Phys. Lett. 87, 061918 (2005).
11. Y. Chen, J. L. Fulton, W. Partenheimer, J.Am. Chem. Soc. 127, 14085 (2005); J. L. Fulton, S. M. Heald, Y. S. Badyal, J. M. Simonson, J. Phys. Chem. A 107, 4688 (2003).
12. Y. Suzuki, Shelly D. Kelly, Kenneth M. Kemner, Jillian F. Banfield, Nature 419, 134 (2002).
13. L. V. Azaroff, Rev. Mod. Phys. 35 (4), 1012 (1963); F. W. Lytle, J. Sync. Rad. 6, 123

(1999); L. G. Parratt, Rev. Mod. Phys. 31, 616 (1959).

14. E. A. Stern, J. Sync. Rad. 8 (2), 49 (2001).
15. X-ray absorption: principles, applications and techniques of EXAFS, SEXAFS and XANES, ed. by D.C. Koningsberger and R. Prins (Wiley); Chap 1(1988).
16. J. T. Sakurai, Advanced Quantum Mechanics, Addison-Wesley, reading, MA, Chap 2 (1967).
17. J. Rehr and R. C. Albers, Rev. Mod. Phys. 72, 621 (2000).
18. B. K. Teo and P. A. Lee, J. Am. Chem. Soc. 101, 2815 (1979); P. A. Lee and G. Beni, Phys. Rev. B 15 (6), 2862 (1977).
19. G. Bunker, Nucl. Instr. Meth. 207, 437 (1983); A. Di Cicco and A. Filipponi, Journ. of Non-Crystalline Solids 156-158, 102 (1993); L. Ottaviano, A. Filipponi, A. Di Cicco, S. Santucci, and P. Picozzi, Journ. of Non-Crystalline Solids 156-158, 112 (1993); A. Filipponi and A. Di Cicco, Synchrotron Radiation News 6, 13 (1993); Angela Trapananti and Andrea Di Cicco, Phys. Rev. B 70, 014101 (2004).
20. C. J. Powell, Surf. Sci. 44, 29 (1974); L. V. Azaroff, Rev. Mod. Phys. 35, 1012 (1963).
21. Keski-Rahkomen and M. O. Krause, At. Data Nucl. Data Tables 14, 140 (1974).
22. Daniel Haskel, Ph. D thesis, "Local structural studies of oriented high temperature superconducting cuprates by polarized XAFS spectroscopy" Appendix A (1998).
23. http://cars9.uchicago.edu/~ravel/software/doc/Athena/html
24. M. Newville, J. Synchrotron rad. 8, 96 (2001).
25. http://depts.washington.edu/uwxafs/Docs/feffit.ascii.
26. D. W. Marquardt, J. Soc. Ind. Appl. Math. 11, 431 (1963).
27. M. Newville, B. Boyanov and D. E. Sayers, J. Sync. Rad. 6, 264 (1999); M. Newville, B. Ravel, D. Haskel, J. J. Rehr, E. A. Stern and Y. Yacoby, Physica B 208 & 209, 514 (1995).
28. L. Brillouin, Science and Information Theory, Academic Press, New York (1962).
29. X-ray absorption: principles, applications and techniques of EXAFS, SEXAFS and XANES, ed. by D.C. Koningsberger and R. Prins (Wiley), Chap 2, 11 (1988); J. J. Rehr and R. C. Albers, Phys. Rev. B 41(12), 8139 (1990); A. Bianconi, Appl. Surf. Sci. 6, 392 (1980); A. Bianconi, S. Doniach and D. Lublin, Chem. Phys. Lett. 59, 121 (1978).
30. J. Wong, F. W. Lytle, R. P. Messmer, D. H. Maylotte, Phys. Rev. B 30, 5596 (1984); A. Pantelouris, G. Kuper, J. Hormes, C. Feldmann, M. Jansen, J. Am. Chem. Soc. 117, 11749 (1995).
31. M. Brown, R. E. Peierls and E. A. Stern, Phys. Rev. B 15(2), 738 (1977).
32. Z. H. Lu, T. K. Sham, M. Vos, A. Bzowski, I. Mitchell, P. R. Norton, Phys. Rev. B 45, 8811 (1992).
33. Christopher A. Impellitteri, Otis Evans and Bruce Ravel, J. Environ. Mon. 9, 358 (2007).
34. Stanislav Stoupin, Eun-Hyuk Chung, Soma Chattopadhyay, Carlo U. Segre, and Eugene S. Smotkin, J. Phys. Chem. B 110, 9932 (2006).
35. U. Skyllberg, P R Bloom, J. Qian, CM Lin, W. F. Bleam, Environ. Sci. & Tech. 40, 4174 (2006); J. Gardea-Torresdey, J. Peralta-Videa, G. de la Rosa, J. Parsons, Coord. Chem. Rev. 249 (17–18), 1797 (2005).
36. Debdutta Lahiri, Vaidyanathan Subramanian, Tomohiro Shibata, Eduardo Wolf, B. A. Bunker, Prashant V. Kamat; J. of Appl. Phys. 93(5), 2575 (2003).
37. Debdutta Lahiri, V. Subramanian, P. V. Kamat and B. A. Bunker; J. Chem. Phys 124, 204720 (2006).
38. Nand Lal Misra, Debdutta Lahiri, Khush Dev Singh Mudher and Surinder M. Sharma, accepted, X-ray Spectrometry (2008).
39. G. Vlaic, E. Fonda, R. Psaro and L. Sordelli, Jap. J. Appl. Phys. 38, 24 (1999); L. Sordelli, R. Psaro, G. Vlaic, A. Cepparo, S. Recchia, C. Dossi, A. Fusi and R. Zanoni, J. Catal., 182, 186 (1999); G. Vlaic, R. Di Monte, P. Fornasiero, E. Fonda, J. Kaspar and M.

Graziani, J. Catal. 182, 378 (1999); C. Lamberti, S. Bordiga, D. Arduino, A. Zecchina, F. Geobaldo, G. Spano, F. Genoni, G. Petrini, A. Carati, F. Villain and G. Vlaic, J. Phys. Chem. B 102, 6382 (1998); G. Vlaic, R. Di Monte, P. Fornasiero, E. Fonda, J. Kaspar and M. Graziani, Catalysis and Automotive Pollution Control IV Stud. Surf. Sci. Catal. 116, 185 (1998); G. Vlaic, D. Andreatta and P. E. Colavita, Cat. Today 41, 261 (1998); G. Vlaic, P. Fornasiero, S. Geremia, J. Kaspar and M. Graziani, J. Catal. 168, 386 (1997); L. Basini, A. Aragno and G. VLAIC, Catal. Lett. 39, 49 (1996).

40. Y. Uchimoto, S. Goto, Y. Terada, Spring-8 User Experiment Report (No. 13), 8 (2004A).

41. M. Ueneshi, H. Tanaka, M. Taniguchi, K. Naitou, H. Hiraoka, Y. Nishihata, J. Mizuki, Spring-8 User Experiment Report (No. 13), 12 (2004A).

42. M. Takaoka, T. Yamamoto, T. Tanaka, K. Oshita, H. Hirada, T. Izawa, Spring-8 User Experiment Report (No. 13), 1 (2004A).

43. Y. Takahashi, S. Kodama, M. Fukukawa and Y. Yamashita, Spring-8 User Experiment Report (No. 13), 12 (2004A).

44. T. T. Eighmy, C. Gonzalez, T. Shimaoka, T. Yamashige, J. Etoh, S. Sakita, A. Motohata, T. Haraguchi, Spring-8 User Experiment Report (No. 13), 12 (2004A).

45. M. Vespa, R. Dahn, D. Grolimund, E. Wieland and A. M. Scheidegger, Environmental Science & Technology 41 (2007), no. 6, 1902-1908; M. Vespa, R. Dahn, E. Gallucci, D. Grolimund, E. Wieland and A. M. Scheidegger, Environmental Science & Technology 40 (2006), no. 24, 7702-7709.

46. http://gbxafs.iit.edu/training/thickness_effects.pdf

47. P. Pfalzer, J.-P. Urbach, M. Klemm, S. Horn, M. L. denBoer, A. I. Frenkel and J. P. Kirkland, Phys. Rev. B 60, 9335 (1999).

48. D. Vlachos, J. Sync. Rad. 12, 224 (2005).

49. F. W. H. Kampers, EXAFS in Catalysis: Instrumentation and Applications, Chap. 3 (1988); Y. Udagawa, The Rigaku Journal 6 (1), 20 (1989); T. Taguchi, Q-F Xiao and J. Harada, J. Sync. Rad. 6, 170 (1999).

50. http://mrcat.iit.edu/mrcat instrumentation.html; http://www.elettra.trieste.it/experiments/beamlines/xafx/index.html

51. http://www.exafsco.com

52. A. J. Kropf, R. J. Finch, J. A. Fortner, S. Aase, C. Karanfil, C. U. Segre, J. Terry, G. Bunker and L. D. Chapman, Rev. Sci. Instrum. 74 (11), 4696 (2003).

53. X-ray absorption: principles, applications and techniques of EXAFS, SEXAFS and XANES, ed. by D.C. Koningsberger and R. Prins, Wiley; Chap 10 (1988); K. M. Kemner, Z. Whang, R. Mayovanic and Bruce A. Bunker, Nucl. Instrum. Meth. B 71, 345 (1992).

54. http://gbxafs.iit.edu/training/Noise.pdf

55. P. A. Lee, P. H. Citrin, P. Eisenberg and B. M. Kincaid, Rev. Mod. Phys. 53, 769 (1981).

56. http://www.csrri.iit.edu/periodic-table.html

57. F. Decremps, F. Datchi, A. M. Saitta, and A. Polian, Phys. Rev. B 68, 104101 (2003); Cristina Piquer, Fernande Grandjean, Olivier Mathon, Sakura Pascarelli, Daniel L. Reger and Christine A. Little, Gary J. Long, Inorg. Chem. 42, 982 (2003); A. San-Miguel, H. Libotte, M. Gauthier, G. Aquilanti, S. Pascarelli and J.-P. Gaspard, Phys. Rev. Lett. 99, 015501 (2007); S. Pascarelli, M. P. Ruffoni, A. Trapananti, O. Mathon,1 G. Aquilanti, S. Ostanin, J. B. Staunton and R. F. Pettifer, Phys. Rev. Lett. 99, 237204 (2007); C. B. Vanpeteghem, R. J. Nelmes, D. R. Allan, M. I. McMahon, A. V. Sapelkin and S. C. Baylis, Phys. Stat. Sol. B 223, 405 (2001); A. Di Cicco and A. Filipponi, J. Non-Cryst. Solids 205-207, 304 (1996); A. Di Cicco, M. Minicucci and A. Filipponi, Phys. Rev. Lett. 78, 460 (1997); A. Di Cicco, Phys. Rev. Lett. 81, 2942 (1998).

58. N. C. Das, D. Lahiri and D. Bhattacharyya, J. Optics 36 (1), 8 (2007); S. Pascarelli, O. Mathon and G. Aquilanti, J. Alloys and Comp. 362, 33 (2004).

59. http://www.esrf.eu/UsersAndScience/Experiments/XASMS/BM29/UsersGuide/cryostat

60. John L. Fulton, Yongsheng Chen, Steve M. Heald and Mahalingam Balasubramanian, Rev. Sci. Instrum. 75 (12), 5228 (2004); John Fulton, John G. Darab and Markus Hoffman, Rev. Sci. Instrum. 72 (4), 2117 (2001); J. Rohler, J. P. Kappler and G. Krill, Nucl. Instrum. Meth. 208, 647 (1983); Simon R. Bare, George E. Mickelson, Frank S. Modica, Andrzej Z. Ringwelski, N. Yang, Rev. Sci. Instrum. 77, 023105 (2006).

61. S.-K. Cheong, B. A. Bunker, T. Shibata, D. C. Hall, C. B. DeMelo, Y. Luo, G. L. Snider, G. Kramer and N. El-Zein, Appl. Phys. Lett., vol. 78, no. 17, pp. 2458-2460 (2001); B. A. Bunker, Materials Science Bulletin 13, 36 (1988); W. F. Pong, R. M. Mayanovic, and B. A. Bunker, Physica B 158, 617 (1989); P. Bandyopadhyay and B. A. Bunker, Physica B 158, 653 (1989); K.M. Kemner, B.A. Bunker, H. Luo, N. Samarth, J.K. Furdyna, M.R. Weidmann, K.E. Newman, Jpn. J. of Appl. Phys. 32-2, 399 (1993); Q. Lu, B. A. Bunker, H. Luo, A. J. Kropf, K. M. Kemner, J. K. Furdyna, Phys. Rev. B. 55, 9910 (1997).

62. M. I. Boyanov, Jan Kmetko, T. Shibata, Alokmay Datta, Pulak Dutta, and B. A. Bunker, J. Phys. Chem. B 107, 9780 (2003); E. A. Stern, D. E. Sayers, J. G. Dash, H. Schecter, and B. A. Bunker, Phys. Rev. Lett. 38, 767 (1977).

63. N. C. Das, S. N. Jha and A.P. Roy, BARC Report BARC/ 1999/ E/ 035 (1999).

64. N. C. Das, D. Lahiri, D. Bhattacharyya and A. K. Poswal, J. Optics 35 (2), 101 (2006).

Laser Induced Breakdown Spectrometry (LIBS) For Material Characterization

Dr. S.K. Aggarwal *has been heading Fuel Chemistry Division, BARC since July 2005 and is a Professor of Chemistry at Homi Bhabha National Institute (HBNI). He joined the 16th Batch of BARC Training School in 1972 and received the Homi Bhabha Award. He did his Ph.D. from Mumbai University and had his post-doctoral training at University of Virginia, USA. Dr. Aggarwal was honoured with Eminent Mass Spectrometrist Award by the Indian Society for Mass Spectrometry (ISMAS) in 1996 and was recently conferred with DAE Special Contributions award 2006. He is a specialist in the field of atomic mass spectrometry and alpha spectrometry and is interested in various mass spectrometric techniques. His other areas of interest include laser based analytical techniques, Electrochemistry, X-ray spectroscopy and Separation techniques like HPLC, solvent extraction etc. He has more than 100 publications in reputed International Journals and is a recognized Ph.D. Guide of the Mumbai University and of HBNI.*

Mrs.D.Alamelu *obtained her M.Sc. Degree in Physics from Annamalai University. After graduating from 38th Batch of Training School, BARC, she joined Mass Spectrometry Section of the Fuel Chemistry Division in 1995. Initially, she was involved in the indigenous development of Time of Flight Mass Spectrometer. Her other areas of interest include thermal ionisation mass spectrometry, alpha spectrometry and laser induced breakdown spectroscopy (LIBS).*

Introduction

Laser Induced Breakdown Spectrometry (LIBS) is a laser based emission spectroscopic technique that provides non-intrusive, qualitative and quantitative determination of elements in various matrices. LIBS has been developed for a number of applications due to its many advantages in comparison to other emission spectroscopic techniques. These include (i) minimal or no sample preparation (ii) simultaneous multi-elemental analysis capability (iii) applicable to both electrically conducting and non-conducting samples (iv) possibility to use in hazardous and industrial environments etc. Its major limitations are its sensitivity to fluctuations in the analysis conditions such as laser fluence etc. and limited sensitivity for some of the elements due to small amount of material consumption. The physics of the formation of plasma and the basic components of LIBS system are discussed below.

The application of LIBS for elemental analysis has increased over the past decade substantially. The wide range of applications of LIBS can be seen from the number of publications in international journals, and also from the international biannual Conference proceedings of LIBS. In this manuscript, brief theory, a few typical applications and some of the limitations of LIBS would be discussed. For detailed study of LIBS, the readers are referred to a number of reviews as well as books on LIBS published in the recent years [1-12].

Physics of Laser Induced Breakdown Process

For laser pulse width of the order of a few nanoseconds, the absorption of the laser light can be explained based on the thermal transport model [13]. The basic effects that are caused by the absorption of focused laser radiation at the surface of solids are (i) heating (ii) melting (iii) vaporization (iv) excitation

Dr. S.K. Aggarwal and Dr. D.Alamelu, Fuel Chemistry Division, Bhabha Atomic Research Centre, Trombay, Mumbai 400 085;
E-mail: skaggr@barc.gov.in

& ionization of the material. In the time scale of a few picoseconds, the electrons absorb the photons and transfer this energy to the lattice through a number of collisions both among themselves and with the lattice phonons. Thus this optical energy can be considered to be converted as heat instantaneously. The intense local heating experienced by the target results in an increase of the surface temperature of the material. Heat is conducted into the interior of the target and a thin molten layer of the material is formed just below the surface. As the thermal energy deposited increases, a point is reached where the deposited energy exceeds the latent heat of vaporization. At this point, heat is no longer conducted into the material. The surface reaches the boiling temperature and evaporation occurs from the surface. Distribution of energy occurs so rapidly that one can assume reaching a local thermodynamic equilibrium (LTE) during the duration of the laser pulse. However, this assumption is not valid for laser pulses of very short duration (pico and femto seconds).

The energy density deposited at the surface of the target by a laser pulse of power density F and duration T_L is given by FT_L. The average energy acquired by the thin layer of molten metal per unit mass is then given by $FT_L/[\rho\,(aT_L)^{1/2}]$ where ρ is the mass density and a is the thermal diffusivity of the material. For evaporation to occur, the energy deposited in this thin layer must exceed the latent heat of vaporization (L_V) of the material

$$FT_L/[\,\rho\,(aT_L)^{1/2}] > L_V$$

The minimum power density below which no evaporation from the surface would occur is then given by

$$F_{min} = \rho\, L_V a^{1/2} T_L^{-1/2}$$

Temperature of the vapor leaving the surface is higher than the boiling temperature and hence the vapor is partially ionized. A stream of vapor leaves the surface with velocities of 10^6 cm/sec. The micro plasma formed above the surface absorbs the later part of the incoming laser pulse and is further heated. Depending on the type of material, ejection of material in the form of metal droplets can also be observed.

Two mechanisms that are responsible for electron generation and the growth of laser induced breakdown are (i) multi-photon absorption and (ii) collision induced ionization. The multi-photon absorption involves simultaneous absorption of certain number of photons by an atom /molecule leading to its ionization. This mechanism is important in case of short wavelength lasers ($\lambda <$ 1000 nm) and at low pressures (< 10 torr). In the collision induced ionization process, the electrons in the focal volume are accelerated by the electric field of the laser and gain energy by colliding with neutral atoms. After the electrons have gained sufficient energy, they can ionize atoms by collisions and this causes the electron density to grow exponentially with time. This process is dominant at high pressure (> 100 torr in N_2) and long wavelength ($\lambda >$ 1000 nm).

Characterization of the laser-induced plasma has been carried out both in time and spatial evolution of the plasma. The evolution of laser plasma can be divided into several transient phases. The initial plasma (0-100 ns) is characterized by high electron and ion densities (10^{17} to 10^{20} cm^{-3}), and temperatures around 20,000 K. The emission spectrum from the early stage of the plasma is characterized by a continuum background emission due to bremsstrahlung (collisions between the free electrons and the excited atoms and ions) and recombination of electrons with ions present in the plasma. Emission lines from ions and atoms can be found after about 300 ns delay. These lines are superimposed on the strong continuum background and are broadened by the Stark effect due to the high electron density. As the plasma expands and cools, the electrons and ions recombine, and a characteristic loud sound can be heard due to the shock wave emitted from the plasma. The continuum background decays rapidly and the atomic emission lines become narrower and weaker. After the initial plasma (300 nsec), the atomic emission decays slowly, and emission from the sample molecules appears. A properly selected detection window can improve the signal-to-background ratio (S/B) of the data, which is important for quantitative measurements.

The excitation characteristics of the laser plasma are determined by the plasma properties, which can be described by the temperature and electron density of the plasma. The analytical measurements are generally performed after the initial plasma, when a state of LTE is achieved. At the LTE condition, the analyte intensity is proportional to the relative population of the level, and follows the Boltzmann distribution.

$$\frac{N_j}{N_o}=\frac{g_j}{Z}\exp\left(\frac{-E_j}{kT}\right)$$ with respect to the ground state

$$\frac{N_j}{N_i}=\frac{g_j}{g_i}\exp\left(\frac{-(E_j-E_i)}{kT}\right)$$ for relative populations

where i & j refer to the lower and higher levels, N_o is the total species population, N_i and N_j are the populations of the levels of energy E_i, and E_j, g_i and g_j are the statistical weights of the levels, Z is the partition function, which is usually taken as the statistical weight of the ground state.

Since the laser induced plasma is usually at high temperatures, it is useful for emission spectroscopic studies. When an optical transition occurs between two levels (n & m) of an atom or ion, the observed intensity I_x integrated over the line profile is given by

$$I_x = h\nu_{mn}A_{mn}N_m$$

where
h = Planck's constant
ν = Frequency of the optical transition
A_{mn} = Einstein coefficient for spontaneous emission from the upper energy level "m"
N_m = Number of atomic/ molecular species in level m

In case of LTE, we have

$$I_x = h\nu_{mn}A_{mn}N_n\frac{g_m}{g_n}\exp\left(\frac{-\Delta E_{nm}}{kT}\right)$$

LIBS for trace constituents determination is based on the measurement of the line intensities which are correlated to the concentration/ amount of element in the sample. Conventionally, another element (e.g. matrix element) is used as an internal standard and the intensity ratios are used instead of absolute intensities.

Instrumentation

LIBS is a plasma based method of emission spectroscopy. It employs instrumentation similar to that in the other atomic emission spectroscopic techniques. Typical components of an LIBS system and their functions are explained below in Table 1. The schematic of an LIBS system is shown in Fig. 1.

TABLE 1. Typical Components of an LIBS System and their Functions

Component	Function
Pulsed laser	Generates the powerful optical pulse to create a micro plasma on the surface of the sample
Sample chamber	For placing the sample at a particular geometry reproducibly with suitable movement for bringing fresh sample surface for individual laser shots; air tight arrangement for use under vacuum or under different gaseous atmosphere
Focussing & light collection system	Directs the laser pulse on to the sample and provides sufficient fluence for the formation of micro plasma. The spectral emission from the plasma is collected and is transported to the detection system
Dispersion system	Consists of an equipment e.g. grating for suitable dispersion of the spectrum
Detector	Such as charge coupled devices (CCDs) for recording the spectra
Control electronics	To control the gating of the detection system, storage of the spectrum for further analysis etc.

Calibration in LIBS

The basis of any emission spectroscopic analysis can be written as follows:

$$C_x \rightarrow N \rightarrow N^* \rightarrow J \rightarrow Q \rightarrow I_x\ S_x$$

where
C_x = Concentration of analyte in the sample
N = Number of atoms of the analyte in the plasma

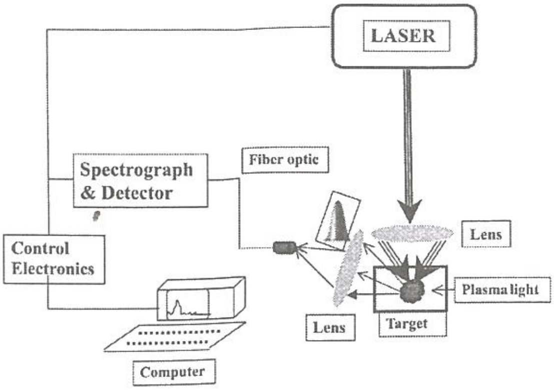

Fig. 1 Schematic of a Laser Induced Breakdown Spectrometer

N^* = Number of analyte atoms in the particular excited state
J = Total radiation from these atoms
Q = Fraction of this radiation entering the spectrograph
I_x = Intensity of the radiation of the analyte at a given wavelength
S_x = Measured signal

Quantitative analysis is based on the development of the function

$$S_x = f(C_x)$$

which expresses the relationship between the intensity of the analytical line (S_x) and amount (C_x) of the element x in the sample.

The ultimate goal of developing this relationship is to provide quantitative analysis with high precision and accuracy. For achieving this, a calibration curve of the instrument response vs. the absolute mass (amount) of the element present is prepared. Calibration curves are established using a set of certified reference materials or secondary standards or calibration samples having a composition as close as possible to the unknown samples. This provides the best results as matrix effects will be identical are usually minimized if the standards and the unknown samples have the same bulk composition.

Applications of LIBS

LIBS has been widely applied in different areas of science and technology such as industrial, environmental, forensic, geology and nuclear science and technology. A few examples of these applications are given below.

Nuclear Science and Technology

Trace Elemental Determination

Since LIBS involves minimal sample preparation steps, has remote analysis capability and a few nanograms are consumed per analysis with minimal damage to the sample, it is ideally suited for different applications in nuclear science and technology. LIBS has been employed to detect trace elements in uranium and plutonium di-oxide pellets [14]. A second harmonic of Nd-YAG (532 nm) of energy 15 mJ was used in this work at atmospheric pressure. Fifteen impurities at concentrations of about 500 ppm and twelve impurities at concentrations of 100 ppm were detected in emission rich matrices of UO_2 and PuO_2. Detection limits for impurities in PuO_2 were slightly better than those in UO_2 matrix due to the simpler spectrum of Pu. These studies were then extended to powder samples and an on-line analysis of the PuO_2 powders was demostrated.

LIBS has been applied for on-line multielement analysis of glass melts in the vitrification process of high level liquid waste [15]. The third harmonic of Nd-YAG laser of 4 mJ energy was used in this work. The plasma generated from the molten surface of the glass was then monitored by an echelle spectrograph in the wavelength region of 200 – 780 nm. Twelve different reference high level liquid waste (HLLW) glass melts with different chemical compositions of 27 elements were simulated. By real-time analysis of these glass melts at 1200° C, the analytical method was calibrated and applied for multielement characterization of molten glass samples from a prototype vitrification plant. The results showed the potential of LIBS for on-line analysis during vitrification process of the highly radioactive glass melts.

LIBS has also been used for the determination of Ga in PuO_2 [16]. The samples were generated by the thermally induced gallium removal (TIGR) process which is one of the pretreatment steps prior to MOX fuel processing. Nd-YAG laser fundamental (1064 nm) of energy 420 mJ/pulse was used in this work. LIBS was found to have useful analytical range of 30 to 400 ppm for Ga in PuO_2.

LIBS has been developed for on-line monitoring at the reprocessing plant at Sellafield, West Cumbria. Remote analysis capability of LIBS was reported for the characterization of solid material collected in the redundant dissolver baskets [17]. Remote analysis of a material within a hot cell was carried out by directing the laser beam of a telescope LIBS instrument through a lead-glass radiation shield window. The results of the analysis showed that the material was rich in zirconium and molybdenum. Combining this information with the existing knowledge of the chemistry of the process, it was deduced that the contaminant material consisted mainly of zirconium molybdate - a material that is known to form during the reprocessing of spent fuel and which is largely insoluble in nitric acid.

Isotopic Analysis

LIBS is conventionally used for trace elemental analysis, but it has been employed for the determination of isotopic composition by employing high resolution spectrograph. In one such study, $^{240}Pu/^{239}Pu$ atom ratio was determined by LIBS by using the isotope shift of the isotopes (0.355 cm^{-1}) in the spectral line 594.52202 nm [18]. In this work, Nd-YAG fundamental of energy 25 mJ was used and spectral deconvolution was employed by studying the two isotopic standards of Pu. The isotope ratio was obtained with a precision of around 10% in these studies. The technique is sensitive, essentially non-destructive, and can produce accurate results with reasonable precision. The authors stated that the linewidths observed under these conditions for plutonium should be applicable to all of the light actinides (Th-Cm) under the same experimental conditions because the first ionization potentials are similar, ranging from 5.97 eV for Am to 6.27 eV for Np and changes in the relative masses are small.

LIBS has been reported for the quantitative analysis of deuterium with a detection limit of 50 ppm [19]. 1064 nm Nd-YAG laser with an output energy of 75 mJ was used. Simultaneous detection of deuterium and hydrogen in solid samples was demonstrated using helium gas at low pressures (5 torr). Due to the much lower density of electrons and ions in the He plasma compared to that of air, the stark broadening was significantly reduced and simultaneous detection of H_α (656.2 nm) and $D\alpha$ (656.0 nm) which were separated by 1.8 nm was achieved. Acquisition delay and gate width of 5 and 50 ms, respectively, were used in this work. Porous alumina samples were dipped in solutions containing varying proportions of H_2O and D_2O and were used for preparing a calibration curve. These studies are interesting since in the nuclear industry, determination of H & D in zirconium based materials is very important.

Forensic

Due to its non-destructive capabilities, LIBS is widely developed for forensic applications. LIBS has been used to determine whether the hands of a suspected gun user contain traces of gunshot residue (GSR) [20]. Monte-Carlo simulation techniques have been employed for deriving at the error rates. Multiple spectral line data have been used for clearly evaluating the error rates in this study and LIBS has been recommended as a screening test for GSR analysis.

In the present scenario, the ability to detect trace amounts of explosives and their residues in a short span of time is of vital interest. The application of LIBS for the detection of energetic materials has been demonstrated. Recently, a double-pulse standoff system (ST-LIBS) was reported to detect explosive residues from a distance of 20 m [21]. Chemometric techniques such as linear correlation, principal components analysis (PCA), and partial least squares discriminant analysis (PLS-DA) for the identification of explosive residues were employed. It was reported that despite the typical characterization of LIBS as an elemental technique, the relative elemental intensities in the spectra are representative of the stoichiometry of the parent molecules and can be used to discriminate materials containing the same elements. Simultaneous biohazard and explosive residue discrimination at standoff distances was also demonstrated in this work.

LIBS has also been used to study the colonies of vegetative cells or spores of five bacterial strains: Bacillus thuringiensis T34, Escherichia coli IHII/pHT315, Bacillus subtilis 168, Bacillus megaterium QM B1551, and Bacillus megaterium PV361 [22]. The major inorganic components of the bacterial samples, including Ca, Mn, K, Na, Fe, and phosphate, were clearly identified from the breakdown emission spectra. The bacterial spores accumulate a lot of calcium that showed strong LIBS emissions at 393.7 nm and 396.9 nm. The diverse emissions from the phosphate component at 588.1 nm and 588.7 nm provide a fingerprint for bacterial strains. The relative change of inclusions in the bacteria was distinguished by two-dimensional charts of the bacterial components. The results demonstrated the potential of LIBS for rapid and low false-positive classification of bacteria with minimum sample preparation.

Material analysis and characterization can provide important information evidence in legal proceedings. LIBS was evaluated for the forensic elemental analysis of casework size glass samples collected from different cars [23]. The identification of ball-pen ink in questioned documents (QD), by using "elemental fingerprint" comparison was carried out [24]. Similarly identification of originality of artistic painting was also reported [25].

Environmental Sciences

LIBS has been employed for the determination of nitrogen [26] and total carbon [27] in sand and soil samples. Nitrogen measurements were carried out at reduced pressures of 0.04 torr to minimize the contribution from the atmospheric nitrogen. Emission data in the spectral region of 741 - 749 nm generated using a laser energy of 60 mJ of Nd-YAG fundamental was recorded. Calibration curves were obtained using nitrogen spiked sea sand samples in the region of 0.33 % to 6 %. The limit of detection was found to be 0.8 % N. Similarly, total carbon content in soils was also obtained using Nd-YAG laser fundamental of energy 50 mJ and the results were compared with those obtained by the conventional dry combustion methods.

Platinum group elements (PGEs) are used in the automobiles as catalytic convertors to reduce the amount of pollutants from the automobile exhaust. Due to the complex structure of these systems, the study of the distribution by wet chemistry routes is unpractical. LIBS has been employed for the study of three dimensional compositional [28] distribution of these elements. It was found that while Pt is homogeneously distributed, the distribution of Pd and Rh is inhomogeneous.

Industrial Applications of LIBS

Since LIBS can provide data on major and trace constituents in various matrices on a real time and also spatial distribution of the different constituents, the technique is ideally suited for many industrial applications as well as in diagnostics of a variety of finished products. A number of industrial applications have been developed using LIBS.

LIBS has been employed for the 2D elemental composition mapping in aluminium alloys with a lateral resolution of 10 micron [29] using 0.008 mJ of a quadrupled Nd-YAG laser (266 nm). The precipitates in the alloy matrices namely Al-Cu-Fe-Mn (type-I) and Al-Cu-Mg (Type –II) were unambiguously distinguished.

LIBS has also been developed for the rapid in-situ analysis of solid and molten metals at variable distances of up to 1.5 m. Laboratory experiments using an induction furnace have shown the response and usefulness of LIBS for in-situ monitoring of Cr, Cu, Mn and Ni in the concentration ranges of 0.11 to 13.8 wt %, 0.044 – 0.54 %, 1.38 – 2.5% and 0.049 – 5.92 %, respectively, in liquid steel [30].

LIBS has been investigated as a diagnostic tool for elemental composition analysis of thin films of FeHfO. The Fe/Hf ratio was investigated to obtain a semi-quantitative data for the stoichiometry of the films in this work [31].

LIBS has been applied for the diagnosis and analysis of uncorroded and artificially weathered glasses [32]. Data on the major components as well as the chromophores of the glass samples were obtained. Stratigraphic analysis, by applying the laser pulse on the same spot, allowed the detection of different corrosion layers that build up during the weathering process. The results from LIBS have been compared and agreed well with the conventional techniques such as SEM/EDAX, XRF and UV-Vis spectroscopy.

LIBS was also employed for the real-time monitoring of high temperature corrosion in stainless steels [33]. LIBS was applied for studying the compositional changes with high temperature conditions from 20 to 1200 °C to the protective anti-corrosion layer from a distance of around 10 m. Real time monitoring of Fe and Cr content as a function of temperature and exposure time was carried out.

LIBS was applied for the study of titanium dioxide anti-reflection coatings for photovoltaic cells [34]. The depth profilings from several samples with different thicknesses of TiO_2 was studied. Depth resolution of the order of 40 nm was obtained in this work. The valuable aspect of LIBS is the ability to perform measurements in a contactless manner at room temperature and also in different atmospheres on wafer-sized samples.

Miscellaneous Other Applications

Hydrogen gas is primarily used as a fuel in the space program and is also important in fuel cells and other non-hydrocarbon based power cycles. Since H is highly inflammable and its real time monitoring in such systems is desirable. LIBS has been investigated as a technique for hydrogen gas sensor [35]. Studies were reported on using the direct plasma in the gas stream as well as on a solid substrate where the gas is adsorbed. Using stainless steel as the substrate, detailed analysis of hydrogen in the binary gas mixture with nitrogen has been performed. Using the 656.28 H line, the detection limit of 20 ppmw was obtained.

Classification of meteorites is generally made by studying the emission line ratio of some of the characteristic elements when geochemical analysis is not feasible. The plasma generated in LIBS has similar characteristics to that of the plasma generated during the impact of meteorite with earth's atmosphere. Hence LIBS can be useful for meteorite classification and for developing on-flight techniques for investigation of asteroids. LIBS has been applied for standard meteorites of different typologies [36]. In this work, lunar and Martian meteorites were examined. These studies show the possibility of using LIBS for measurement of real surface of Mars and Moon and recognition of different kinds of extraterrestrial basalts.

Analysis of Liquids

LIBS is mostly applied for the analysis of solid samples providing high sensitivity and reproducibility for most of the elements in the Periodic Table. The application of LIBS for liquid samples has some inherent draw-backs such as splashing, surface ripples, quenching of emitted intensity, a shorter plasma life-time etc [37–39]. Different methodologies have been developed for analyzing liquids. These include (a) freezing samples [40] (b) laminar flows and liquid jets [41,42] (c) double-pulse technique [37] (d) liquid to solid conversion technique [43] (e) on droplets [44,45] (f) solid surface analysis [46]. LIBS has been used for the determination of several elements (Mg, Ca, Cr Ni) [38] and some chlorinated hydrocarbons (CHCs) [47] in aqueous solutions. LIBS has also been applied for the bulk analysis of aqueous solutions containing alkali metals [37, 48] alkaline earth metals [37,48-49] and other metals[37]. Analytical experiments on droplets have been reported for the determination of Li, Na, Mg, Ca, Mn, Al [44-45] as well as for K [50,51], Ba [50], Rb Li and Cd [52] in a liquid jet. Species in organic solvents have also been determined [37].

Interferences in LIBS Analysis

In LIBS, there are many parameters which affect the precision and accuracy of the measurements and these are listed in Table 2. Parameters such as the stability of laser energy and others that are dependent on sample and sampling procedures can be controlled to a great extent. Since the materials are directly sampled in LIBS with little or no sample preparation, the chemical and physical properties of the sample can have a strong effect on the analysis.

It has been documented that the changes in the geometrical aspects can affect LIBS measurements significantly. The power intensity incident on the sample is a strong function of the lens to sample distance (LTSD). The power density usually determines the emission line intensities, relative intensity of the emission lines, the mass of the sample ablated etc. The lens used (spherical or cylindrical) to focus the laser light can have significant effect on the sampling geometry. The plasma temperature is also a function of LTSD.

TABLE . Factors Affecting Quantitative Analysis in LIBS

Source	Factors	Effects/ Control
Laser	Laser pulse energy Laser pulse power Repetition rate	Can be controlled under constant temperature operation
Sampling parameters	Lens-to sample distance (LTSD)	Through an automated focusing system, Use of long focal length lenses, Use of collimated beam to form plasma
	Changes in optical path transmission (to/from) sample	Absorption/scattering of laser pulse/ output signal by gases or aerosols.
	Change in atmosphere above the sample	Gas pressure and atmosphere can affect ablation and plasma properties
Sample	Uniformity of composition & surface	Sufficient averaging to obtain representative sample
	Chemical & physical matrix effects	Optimizing the analysis conditions
Detector	Detector gain	Can be kept constant, calibration necessary if the gain changes
	Linearity of response	Operation in the region of linearity or reducing gain to maintain linearity

Hence special care is necessary to maintain the LTSD as invariant for improving the reliability of the analysis results.

LIBS is usually a surface analysis technique. Hence surface deposits such as weathered layers, moisture and dirt can significantly interfere in the determination of underlying bulk compositions. In LIBS, sampling is done over a small region of around 200 mm diameter. Therefore, the inherent inhomogeneity of the sample can affect the determination of surface composition.

Physical matrix effects such as the size of the particle in the analysis of aerosol samples, can also affect the LIBS signal. When the size of the particle decreases, the incident laser can completely vaporize the material thus increasing the intensity of LIBS signal. Any changes in the chemical species of the analyte can also affect the LIBS signal. This is generally termed as chemical matrix effect. If an easily ionizable element such as cesium is introduced in the plasma, the electron-ion recombination is increased and the ion-neutral equilibrium in the plasma is shifted towards the neutral species. LIBS actually measures the total abundance of an element in a sample, since the plasma breaks down the original target sample into its components. In principle, all information regarding the structure and bonding in starting material is lost. However, it has been observed that the signal from an element is dependent on the form of the compound in the sample. The source of this can be due to the chemical effects, since the counter ions (such as NO_3^-, CO_3^{2-}, Cl^-, SO_4^{2-} etc.) in the compounds can change the excitation and emission characteristics of the elements. The variations could also be due to the differences in the mass of compound ablated which is dependent on the heat capacity, vaporization temperature, reflectivity at the laser wavelength since these are usually different for different compounds.

LIBS Status in India

There are two laboratories in India pursuing actively the work on LIBS. These are Fuel Chemistry Division at BARC, Mumbai and Department of Physics, University of Allahabad, Allahabad. At BARC, a commercial unit Spectrolaser 1000M from Laser Analysis Technologies (now known as XRF Scientific), Victoria, Australia is available which uses a high power Q-switched Nd:YAG laser yielding upto 200 mJ of pulse energy at the fundamental IR wavelength of 1064 nm, in a 7 ns pulse, at a repetition rate of 10 Hz and has four separate spectrographs in Czerny-Turner (C-T) configuration with CCD detectors covering the spectral range of 180 to 850 nm with a resolution of 0.6 nm. This system has been used for determination of Sm, Eu and Gd in aqueous solution [53], determination of thorium and uranium in solutions [54] as well as for determination of trace constituents in thoria [55]. The setup available at University of Allahabad consists of a Nd-YAG laser (Continuum Surelite III-10), operating at 532 nm, capable of delivering a maximum energy of 425 mJover a pulse duration of 3-4 ns (FWHM) at a maximum pulse repetition rate of 10 Hz.The characteristic light emitted from plasma is collected by using an optical fibre bundle and fed into the entrance slit of a grating spectrometer (Ocean Optics, LIBS 2000+) equipped with CCD. The spectrometer covers the spectral range 200-500 nm with a spectral resolution of 0.1 nm and 200-900 nm with spectral resolution of 0.75 nm. This system has been employed for the determination of trace elements in solid samples as well as in liquids e.g. Cr determination in industrial waste water [56], detection of elements responsibke for glycemic potential of ripe and unripe fruit peel aqueous extracts of Psidium guajava [57].

Conclusions

LIBS has significant advantages for on-line applications in a variety of matrices and has many applications in various fields of science and technology. The advantages of LIBS namely simultaneous multi-elemental analysis capability, application to remote analysis and for hazardous substances is highly attractive for many applications especially in nuclear science and Technology. With the use of many modifications such as double and multiple pulse LIBS and using fs lasers for analysis, the detection limits can be improved further. Also by employing chemometric analysis of the data, calibration-free LIBS is also possible. The commercial availability of high resolution LIBS instruments (e.g resolution of 0.06 nm at 337 nm) will further enhance the capabilities of LIBS for various other applications.

References

1. A. Bogaerts, Z. Chen, R. Gijbels and A. Vertes: Spectrochim. Acta B 58 (2003) 1867.
2. "Encyclopedia in Analytical Chemistry" by D.A. Cremers and A.K. Knignt, John Wiley and Sons, Chichester (2000).
3. "Laser Induced Plasmas and Applications" by L.J. Radzeimski and D.A. Cremers, Marcel Dekker, New York (1989).
4. "Handbook of Laser Induced Breakdown Spectroscopy" by D.A. Cremers and L.J. Radzeimski, John Wiley and Sons, Chichester (2006).
5. "Laser Microanalysis" by L. M. Blakenburg, John Wiley and Sons, New York (1989).
6. R.E. Russo, X. Mao and S.S. Mao: Anal. Chem. 74 (2002) 70A.
7. R.E. Russo, X.L. Mao, H.C. Liu, J. Gonzalez and S.S. Mao: Talanta 57 (2002) 425.
8. V. Sturm, J. Vrenegor, R.Noll and M. Hemmerlin: J. Anal. At. Spectrom. 19 (2004) 451.
9. W.B. Lee, J. Wu, Y.I. Lee and J. Sneddon: Appl. Spectrosc. Rev. 39 (2004) 27.
10. J.D. Winefondner, I.B. Gornushkin, T.Correll, E.Gibb, B.W. Smith and N. Omenetto: J. Anal. At. Spectrom. 19 (2004) 1061.
11. J.M. Vadillo and J.J. Laserna: Spectrochim. Acta B 59 (2004) 147.
12. J. Scaffidi, S.M. Angel and D.A. Cremers: Anal. Chem. 78 (2006) 24.
13. J.F. Ready: J. Appl. Phys. 36 (1965) 462.
14. P. Ficher, P. Mauchen and C. Moulin: Applied Spectroscopy 53 (1999) 1111.

15. Jong-Il YUN, Reinhardt Klenze and Jae-il Kim: Applied Spectroscopy 56 (2002) 852.
16. C.A. Smith, M.A. Martinez and D.K. Veirs: Los Alamos National LaboratoryReport LA-UR-99-2785, 1999.
17. Applied Photonics Application Note – 002.
18. C. A. Smith, M.A. Martinez, D. K Veirs, D. A. Cremers: Spectrochimica Acta Part B 57 (2002) 929.
19. K.H. Kurniawan, T.J. Lie, M.M. Suliyanti, R. Hedwig, M. Pardede, D.P Kurniawan, Y. Kusumoto and K. Kagawa: Anal. Chem. 78 (2006) 5768.
20. C.R. Dockery and S.R. Goode: Applied Optics 42 (2003) 6153.
21. J. L. Gottfried, F. C. De Lucia, Jr, C. A. Munson and A. W. Miziolek: J. Anal. At. Spectrom., 23 (2008) 205.
22. T. Kim, Z. G. Specht, P. S. Vary and C. T. Lin: J. Phys. Chem. B 108 (2004) 5477.
23. R. Almirall, B. Naes, H. Lai, Program & Abstracts, LIBS-2006, Montreal, Canada, September 5-8, 2006, P-60.
24. R.R. Hart, L.J. East, C. G. Eger, Ibid, P-61.
25. M. Oujja, A. Vila, E. Rebollar, J.F. Garcia, M. Castillejo: Spectrochimica Acta B 60 (2005) 1140-1148.
26. R.D. Harris, D.A.Cremers, M.H. Ebinger and B.K. Bluhm: Applied Spectroscopy 58 (2004) 770.
27. D.A.Cremers, M.H.Ebinger, D.D.Breshears, P.J.Unkefer, S.A. Kammerdiener, M.J. Ferris, K.M. Catlett and J.R. Brown: J. Environ. Qual. 30 (2001) 2002.
28. P. Lucena and J.J. Laserna: Spectrochim. Acta B 56 (2001) 177.
29. I.V. Cravetchi, M. Taschuk, Y.Y. Tsui and R. Fedosejevs: Spectrochim. Acta B 59 (2004) 1439.
30. J. Gruber, J. Heitz, H. Strasser, D. Bauerle and N. Ramaseder: Spectrochim. Acta B 56 (2001) 685.
31. L. Caneve, F. Colao, F. Sarto, V. Spizzichino and M. Vadrucci: Spectrochim. Acta B 60 (2005) 1098.
32. N. Carmona, M. Oujja, E. Rebollar, H. Romich and M. Castillejo: Spectrochim. Acta B60 (2005) 1155.
33. P. I. Garcia, J.M. Vadillo and J.J. Laserna: Applied Spectroscopy 58 (2004) 1347.
34. M.Hidalgo, F. Martin and J.J. Laserna: Anal. Chem. 68 (1996) 1095.
35. A.J. Ball, V. Hohreiter and D.W. Hahn: Applied Spectroscopy, 59 (2005) 348.
36. A. De Giacomo, M.Dell Aglio, O. De Pascale, S. Longo and M. Capitelli: Spectrochim Acta B 62 (2007) 1606.
37. D.A. Cremers, L.J. Radziemski, T.T. Loree: Appl. Spectrosc. 38 (1984) 721.
38. G. Arca, A. Ciucci, V. Palleschi, S. Rastelli, E. Tognoni : Appl. Spectrosc. 51 (1997) 1102.
39. L. St-Onge, E. Kwong, M. Sabsabi, E.B. Vadas: J. Pharm. Biomed. Anal. 36, (2004) 277.
40. J.O. Cáceres, J. Tornero López, H.H. Telle, A. González Ureña : Spectrochim. Acta B 56 (2001) 831.
41. W.F. Ho, C.W. Ng, N.H. Cheung: Appl. Spectrosc. 51 (1997) 976.
42. B.T. Fisher, H.A. Johnsen, S.G. Buckley, D.W. Hann: Appl. Spectrosc. 55 (2001) 1312.
43. D.M. Díaz Pace, C.A. D'Angelo, D. Bertuccelli, G. Bertuccelli: Spectrochim. Acta B 61 (2006) 929.
44. D.E. Poulain and D.R. Alexander: Appl. Spectrosc. 49 (1995) 569.
45. H. A. Archontaki and S. R. Crouch : Appl. Spectrosc. 42 (1988) 741.
46. R.L. Vander Wal, T.M. Ticich, H.R.West Jr., P.A.Householder: Appl. Spectrosc. 53 (1999) 1226.
47. L. M. Berman and P. J. Wolf: Appl. Spectrosc. 52 (1998) 438.
48. R. Knopp, F. J. Scherbaum and J. I. Kim: Fresenius Z. Anal. Chem. 355 (1996) 16.

49. T. Kitamori, T. Matsui, M. Sakagami, and T. Sawada: Chem. Lett. 12 (1989) 2205.

50. W. F. Ho, C. W. Ng, and N. H. Cheung: Appl. Spectrosc. 51 (1997) 87.

51. N.H. Cheung and E.S. Yeung : Appl. Spectrosc. 47 (1993) 882.

52. N.H. Cheung, E.S. Yeung : Anal. Chem. 66 (1994) 929.

53. D.Alamelu, A.Sarkar and S.K.Aggarwal : Talanta (in press).

54. A.Sarkar, D.Alamelu and S.K.Aggarwal : Applied Optics (in press).

55. A.Sarkar, D.Alamelu and S.K.Aggarwal : J. Nucl. Mater. (communicated).

56. N.K.Rai and A.K.Rai : J. Hazardous Materials, 150 (2008) 835.

57. P.K.Rai, N.K.Rai, A.K.Rai and Geeta Watal : Instrumentation Science and Technology, 35 (2007) 507.

Roundup

Facility Utilization and Development as a follow up of BRNS-IANCAS and BITS-Pilani, Goa Campus Collaborative National Workshop 2007

Prof. S.K. Ray

The Board of Research in Nuclear Science (BRNS), Bhabha Atomic Research Centre (BARC), Mumbai, in collaboration with Biological Sciences group, Birla Institute of Technology and Science-Pilani, Goa Campus organized The BRNS-IANCAS National Workshop on Radiochemistry and Application of Radio-isotopes in science, from 20th to 28th January ,2007, at BITS–Pilani, Goa Campus. It was a hands-on training programme that was inaugurated by Prof L K Maheshwari Vice- Chancellor, BITS-Pilani and the welcome address was delivered by Prof T C Goel , Director, BITS-Pilani, Goa Campus. In order to sustain the knowledge, propagate the acquired training to the regular students & researchers and to facilitate research activity, IANCAS donated all the source materials, kits and instruments to the host Institute, BITS-Pilani, Goa Campus.

The instruments donated by IANCAS such as Gamma Ray Spectrophotometer and GM Counter along with sources Co^{60} , Cs^{137} ,Ng^{22} ,Tl^{204} are at present placed in the Measurement Technique Laboratory (MT-1) of the Biological Sciences department and is kept open to the interested researchers and faculty members across the Institute. They have been extensively utilized by the Biology and Physics Groups after the workshop. The instruments and the experiments were included in 'Instrumental Methods of Analysis (IMA)-Lab, BIO-GC391 and PHY-GC391- four unit compulsory formal Lab courses in BITS. The IMA-Lab is guided and run by experienced faculty members in the Institute who are licensed to supervise and work in the radioactive laboratory. From Biology group, the IMA Lab is run by Dr.Judith Braganc'a, Dr.M.Srikanth and Prof S K RAY (Instructor–in- charge). Workshop experiments on Radioimmunoassay, GM characteristics, Gamma Spectrophotometry were incorporated in the Bio- IMA lab.

Every week, students participate in one hour theory class, where the theory part of the experiments was taught and six hours practical. For this compulsory IMA- lab course, 25 students registered in Biology and 28 students registered in Physics, making it a total of 53 students who were benefited from these instruments. The students are subdivided into multiple groups to provide maximum facility to the students to do the experiments using GM-Counter and Gamma Ray Spectrophotometer. The Instructors conducting the laboratory work in Physics are Prof Suresh Ramaswamy (Instructor-in-charge), Dr. Sutapa Ramanan and Dr. P N Deepak. The Physics students were trained in the areas of GM- Characteristics and Gamma Spectrometry.

The extent of learning of the new facility by the students was formally evaluated by Mid-Semester-Viva, comprehensive exam lab practicals and comprehensive closed book examination. The most valuable contribution by IANCAS to BITS-Goa is that all apprehensions of working in Radioactive Laboratory and using radioisotopes were completely alleviated from the minds of students and faculty members of other disciplines. Rather, the resource scientists from BARC, very successfully communicated to the participants the usefulness of this very important

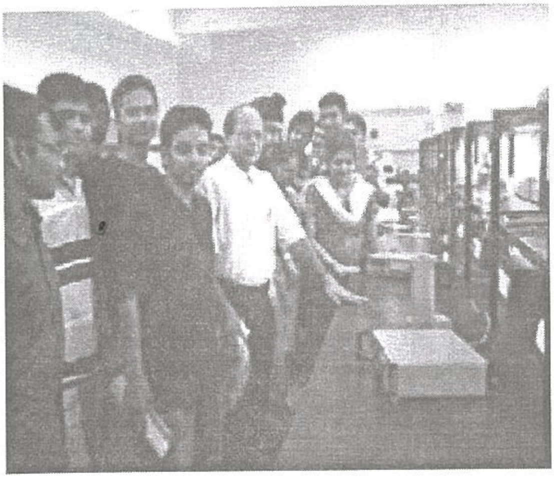

Prof.S.K.Ray and Dr.Judith Braganc'a along with the students in front of the GM Counter and Gamma Spectrophotometer instruments in the MT1 laboratory .

Prof.L.K.Maheshwari, Vice-Chancellor,BITS, is discussing the utilization of facility provided by IANCAS with Prof.S.K.Ray and Dr.Judith Braganca in the MT-1 lab at BITS-Pilani Goa Campus .

branch of nuclear science in research and its application in medical, biomedical and other fields.

Setting up of the Radioactive Laboratory in this campus is gaining ground. We are planning to add a few more instruments depending on our design of experiments for the students, research potentials and programme. New facility is stationed in the MT-1 lab. In this lab, more than three hundred students divided into 13 sections do the measurement techniques experiments in the first semester. The MT-1 lab being very busy, there is need to structure a devoted separate laboratory to work on radioisotope and carry on special projects in the allied fields. . Bio-Group is writing a project for the same. This will strengthen the existing course like Nuclear Physics PHY GC341 which is a compulsory disciplinary course (CDC) in our course curriculum. We want to further extend the existing facility initiated by IANCAS. Faculty members from any institute in Goa can take advantage of such facility available at BITS- Pilani, Goa campus after fulfilling the Institute's requirements.

RNI MAHENG / 2002 / 7152

For Limited Circulation Only

Printed & Published by :
Dr. G.A. Rama Rao, Secretary, Indian Association of Nuclear Chemists and Allied Scientists (IANCAS)
(Registration No. MAH / 232/1984 GBBSD) on the behalf of IANCAS, C/o. Radiochemistry Division ,
Bhabha Atomic Research Centre, Mumbai 400 085

Printed at
Perfect Prints, 22/23, Jyoti Industrial Estate, Nooribaba Dargah Road, Thane 400 601.
Tel. (022) 2534 1291 Telefax : (022) 2541 3546, E-mail : perfectprints@gmail.com

Edited by
Dr. B.S. Tomar, Radiochemistry Division, Bhabha Atomic Research Centre, Mumbai 400 085.
Price Rs. 20.